Turbulence interaction noise

Piccolo, A.

DOI
10.4233/uuid:576a5104-5504-4c7b-b981-228e1d5d2528

Publication date
2026

Document Version
Final published version

Citation (APA)
Piccolo, A. (2026). *Turbulence interaction noise*. [Dissertation (TU Delft), Delft University of Technology]. https://doi.org/10.4233/uuid:576a5104-5504-4c7b-b981-228e1d5d2528

Turbulence Interaction Noise

Andrea Piccolo

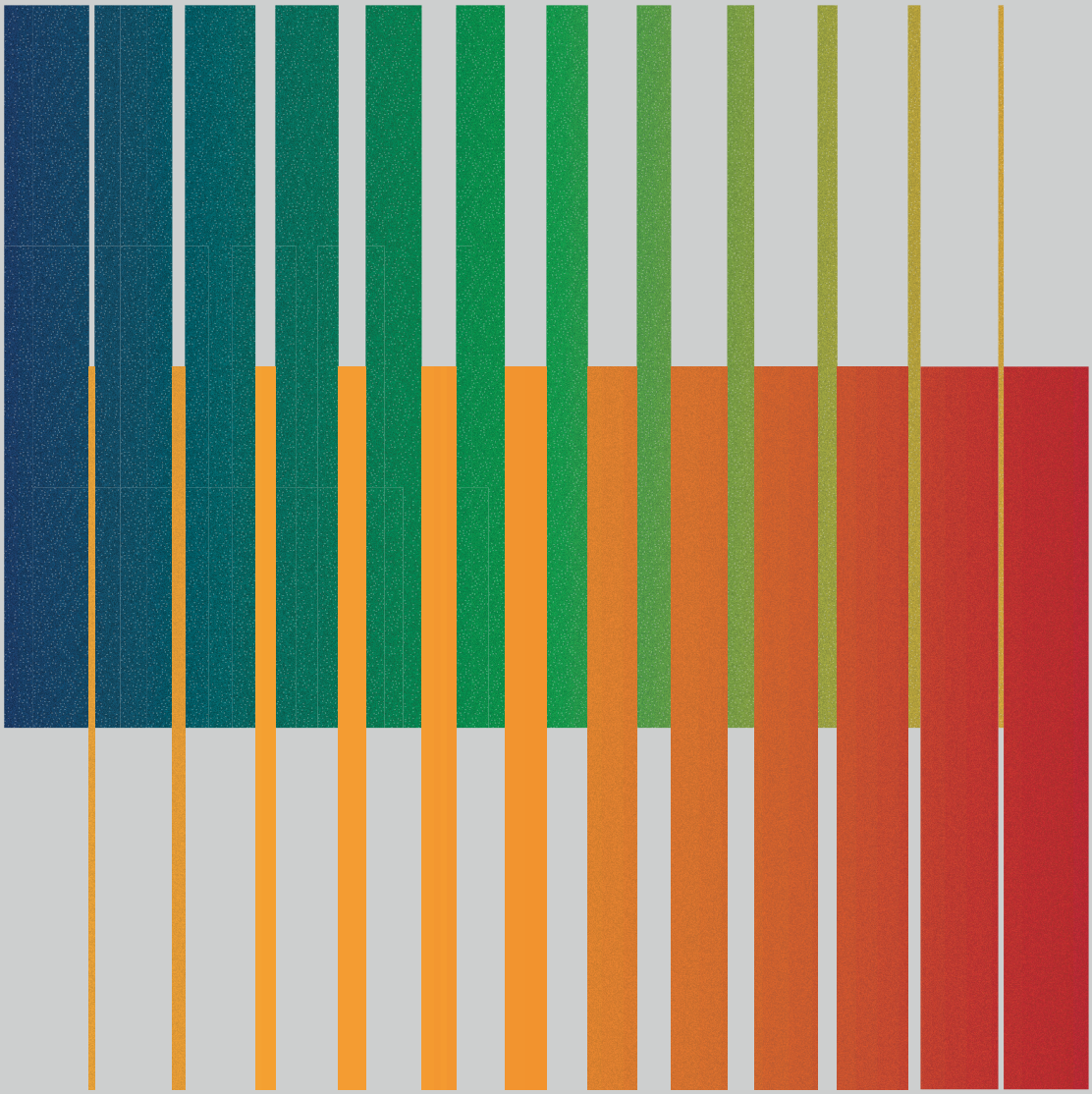

TURBULENCE INTERACTION NOISE

TURBULENCE INTERACTION NOISE

Proefschrift

ter verkrijging van de graad van doctor
aan de Technische Universiteit Delft,
op gezag van de Rector Magnificus prof. dr. ir. H. Bijl,
voorzitter van het College voor Promoties,
in het openbaar te verdedigen
op donderdag 29 januari 2026 om 15:00 uur

door

Andrea PICCOLO

Master of Science in Aerospace and Astronautics Engineering,
Università degli Studi di Napoli “Federico II",
geboren te Napels, Italië.

Dit proefschrift is goedgekeurd door de promotoren.

Samenstelling promotiecommissie:

Rector Magnificus,	voorzitter
Dr. D. Ragni,	Technische Universiteit Delft, promotor
Prof.dr. F. Avallone,	Politecnico di Torino, IT, promotor
Dr. R. Zamponi,	Technische Universiteit Delft, copromotor

Onafhankelijke leden:

Prof. dr. W. Devenport	Virginia Polytechnic Institute and State University, US
Prof. dr. M. Kotsonis,	Technische Universiteit Delft, NL
Prof. dr. S. Moreau,	Université de Sherbrooke, CA
Dr. S. Buck,	Siemens Gamesa Renewable Energy, US
Prof. dr. D. A. von Terzi	Technische Universiteit Delft, NL, reservelid

Keywords: Aeroacoustics, Turbulence Interaction Noise, Turbulence Distortion, Analytical Models

Printed by: Ridderprint

Front & Back: Beautiful cover art that captures the entire content of this thesis in a single illustration.

ISBN 000-00-0000-000-0

An electronic version of this dissertation is available at
http://repository.tudelft.nl/.

Le doute
doit suivre la conviction
comme son ombre.

Albert Camus,
philosopher

Whoever knows only football
doesn't even know anything
about football.

Juan Manuel Lillo,
football coach

CONTENTS

SUMMARY

Turbulence-interaction noise arises from unsteady surface pressure fluctuations caused by the interaction of incoming turbulence with an aerofoil or rotor. This type of flow-induced noise is relevant across a range of diverse applications. Consequently, multiple physical mechanisms must be examined and analytically modelled for use in low-fidelity prediction methods. Such models are particularly valuable during the design and optimisation phases due to their low computational cost. However, their accuracy is critically dependent on the fidelity of the underlying physical assumptions. One of the most widely used and robust approaches, Amiet's model, has been shown to produce inaccurate results for thick blades, as it was originally developed for flat plates. This limitation is likely due to the distortion of the incoming turbulent structures and the alteration of the noise radiation caused by aerodynamic surfaces of non-negligible thickness. Comparable limitations affect its application to rotors, where an accurate representation of the inflow conditions is essential to ensure the reliability of the prediction. The present study seeks to address the following three research questions:

1. How does turbulence distortion affect noise generation and prediction?
2. How can turbulence-distortion effects be included in Amiet's model?
3. How does this apply to rotors?

The first research question is explored through the analysis of an aerofoil in rectilinear motion. The distortion of turbulence interacting with thick aerofoils is analysed with scale-resolved numerical simulations to elucidate its impact on turbulence-interaction-noise generation and prediction. The effect of the leading-edge geometry is investigated by considering two aerofoils with different leading-edge radii subjected to grid-generated turbulence. The velocity field is shown to be altered near the stagnation point, in a region whose extent does not depend on the leading-edge radius. Here, the deformation of the large-scale turbulence causes the amplitude of the upwash velocity fluctuations to increase in the low-frequency range of the spectrum because of the blockage exerted by the surface. Conversely, the distortion of small-scale structures leads to an exponential decay of the spectrum at high frequencies due to the alteration of the vorticity field. The prevalence of a distortion mechanism over the other is found to depend on the size of the turbulent structures with respect to the curvilinear length from the stagnation point to the location where surface-pressure fluctuations and pressure gradient peak. This occurs at the curvilinear abscissa where the curvature changes the most. The same high-frequency exponential-decay slope observed for the upwash velocity is retrieved for surface-pressure spectra in the leading-edge region, suggesting that the aerofoil unsteady response is induced by the distorted velocity field. This physical mechanism can be taken into account in the Amiet model by using a distorted turbulence spectrum as input and accounting for the increased amplitude of the distorted

gust in the aeroacoustic transfer function, obtaining an accurate noise prediction for both aerofoils.

The findings of the initial physical investigation are then applied to address the second research question. When applied to aerofoils with non-negligible thickness, Amiet's theory for turbulence-interaction noise prediction does not account for alterations in the velocity field and acoustic response induced by the surface, resulting in an overestimation of the radiated noise. This work proposes a semi-analytical method that models turbulence distortion in the immediate vicinity of the surface starting from upstream flow conditions and considers the resulting effects on the acoustic response of the aerofoil. The distorted spectrum of the upwash velocity component is calculated using the asymptotic results of the rapid distortion theory (RDT) for very large- and small-scale turbulence, overcoming the need to define a representative location where the turbulence characteristics are sampled. This distorted spectrum is characterised by an increased energy content that is encompassed in the model by scaling the analytical flat-plate formulation of the aeroacoustic transfer function. The proposed approach relies on defining the aerofoil geometrical feature that affects distortion mechanisms, required to extend the RDT results to such geometries. As mentioned above, this parameter is identified as the path travelled by the turbulent eddies from the stagnation point to the position of maximum surface-pressure fluctuations, which is, in turn, related to flow acceleration and leading-edge sharpness. The accuracy of this methodology in enhancing noise prediction is demonstrated using numerical and experimental data of grid-generated turbulence interacting with different aerofoils.

Finally, the focus is put on the full-scale application of rotors. Amiet's model for turbulence-interaction noise prediction for rotors is adapted to incorporate pointwise velocity measurements as input. This is accomplished by using an inverse strip theory approach and transforming the three-dimensional turbulence spectrum, which models inflow conditions, into a one-dimensional term. This latter modification enhances the low-fidelity prediction tool in two key ways. First, it enables its application in cases where turbulence modelling is unavailable or detailed inflow characterisation is impractical. In this way, for example, hot-wire anemometry measurements of the incoming turbulence can be used to compute the acoustic prediction. Second, since the conversion of the turbulence term entails introducing two new functions describing spanwise and axial turbulence correlations, this approach establishes a framework for Amiet's theory in which contributions to turbulence alteration and noise scattering are separated and represented individually. This "modular" structure enables independent analysis and modelling of these contributions, facilitating the application of Amiet's model to complex flow configurations and rotor geometries. The proposed methodology is successfully validated through experimental measurements of a simplified turbulence-interaction setup, where a two-bladed propeller interacts with grid-generated turbulence at three different advance ratios.

The findings of this investigation can be summarised in the following conclusions, each of which directly addresses the initial research questions.

1. Turbulence distortion, related to aerofoil bluntness, causes an alteration of the velocity field in the stagnation region, which affects unsteady surface pressure and hence noise generation.

2. Turbulence-distortion effects should be considered at the stagnation point to enhance low-fidelity prediction. This could be done by using RDT asymptotic results starting from upstream undistorted flow conditions.

3. Amiet's model modification enables the evaluation of the impact of inflow conditions on noise generation and prediction and leads to the application of turbulence-distortion models developed for rectilinear motion.

SAMENVATTING

Turbulentie-interactiegeluid ontstaat door drukfluctuaties op een oppervlak, veroorzaakt door de interactie van inkomende turbulentie met een vleugelprofiel of rotor. Dit type stromingsgeïnduceerd geluid is relevant in een breed scala aan uiteenlopende toepassingen. Daarom moeten meerdere fysieke mechanismen worden onderzocht en analytisch worden gemodelleerd om deze in low-fidelity modellen te kunnen gebruiken. Dergelijke modellen zijn met name waardevol tijdens de ontwerp- en optimalisatiefase vanwege hun lage rekentijd. De nauwkeurigheid ervan is echter sterk afhankelijk van de onderliggende fysieke aannames. Een van de meest gebruikte en robuuste benaderingen, het model van Amiet, blijkt onnauwkeurig te zijn voor dikke bladen, aangezien het oorspronkelijk is ontwikkeld voor vlakke platen. Deze beperking is waarschijnlijk te wijten aan de vervorming van de binnenkomende turbulente structuren en de verandering van de geluidsstraling veroorzaakt door aerodynamische oppervlakken met een niet verwaarloosbare dikte. Vergelijkbare beperkingen gelden voor de toepassing op rotoren, waarbij een nauwkeurige beschrijving van de instromingscondities essentieel is voor de betrouwbaarheid van de voorspelling.

In deze studie worden de volgende drie onderzoeksvragen onderzocht:

1. Hoe beïnvloedt turbulentie-vervorming de geluidsproductie en -voorspelling?
2. Hoe kunnen effecten van turbulentie-vervorming worden opgenomen in het model van Amiet?
3. Hoe is dit toepasbaar op rotoren?

De eerste onderzoeksvraag onderzocht aan de hand van de analyse van een vleugelprofiel in rechtlijnige beweging. De vervorming van turbulentie bij dikke vleugelprofielen is geanalyseerd met scale-resolving numerieke simulaties, om de impact ervan op het ontstaan en de voorspelling van turbulentie-interactiegeluid te verduidelijken. Het effect van de leading-edge geometrie wordt onderzocht door twee vleugelprofielen met verschillende leading-edge radii bloot te stellen aan turbulentie gegenereerd door een turbulentierooster. Het snelheidsveld blijkt nabij het stagnatiepunt te veranderen, in een gebied waarvan de omvang niet afhankelijk is van de leading-edge radius. Hier zorgt de vervorming van grote turbulente structuren voor een toename van de amplitude van upwash snelheidsfluctuaties in het laagfrequente regime van het spectrum, als gevolg van het blokkeringseffect van het oppervlak. Daarentegen leidt de vervorming van kleine structuren tot een exponentiële afname van het spectrum bij hoge frequenties, vanwege de verandering van het vorticiteitveld. De overheersing van het ene vervormingsmechanisme boven het andere blijkt af te hangen van de grootte van de turbulente structuren ten opzichte van de curvilineaire afstand van het stagnatiepunt tot de locatie waar de oppervlakte-drukfluctuaties en de drukgradiënt een piek bereiken. Dit vindt plaats op de

curvilineaire abscis waar de kromming het meest verandert. Dezelfde hoge-frequentie exponentiële afnamesnelheid die wordt waargenomen voor de upwash snelheid, wordt ook teruggevonden in de oppervlakte-drukspectra in het leading-edge gebied, wat suggereert dat de niet-stationaire respons van het vleugelprofiel wordt veroorzaakt door het veranderde snelheidsveld. Dit fysieke mechanisme kan worden opgenomen in het model van Amiet door een vervormd turbulentiespectrum als invoer te gebruiken en rekening te houden met de verhoogde amplitude van de vervormde stromingsfluctuaties in de aero-akoestische overdrachtsfunctie, wat leidt tot een nauwkeurige geluidsvoorspelling voor beide vleugelprofielen.

De bevindingen uit het eerste onderzoek worden daarna toegepast om de tweede onderzoeksvraag te behandelen. Wanneer het model van Amiet wordt toegepast op vleugelprofielen met een niet-verwaarloosbare dikte, neemt de theorie de veranderingen in het snelheidsveld en de akoestische respons die door het oppervlak worden veroorzaakt niet mee, wat resulteert in een overschatting van het geproduceerde geluid. Deze studie stelt een semi-analytische methode voor die de turbulentie-vervorming in de onmiddellijke nabijheid van het oppervlak modelleert, uitgaande van de stroomopwaartse stromingscondities, en rekening houdt met de resulterende effecten op de akoestische respons van het vleugelprofiel. Het vervormde spectrum van de upwash snelheidscomponent wordt berekend met behulp van asymptotische resultaten van de rapid distortion theory (RDT) voor zeer grote en kleine turbulentieschalen, waardoor het niet nodig is om een representatieve locatie te definiëren waar de turbulentie-eigenschappen worden uitgelezen. Dit vervormde spectrum wordt gekenmerkt door een verhoogde energie-inhoud, die in het model wordt opgenomen door de analytische formulering van de aero-akoestische overdrachtsfunctie voor een vlakke plaat te schalen. De voorgestelde aanpak is gebaseerd op het definiëren van het geometrische kenmerk van het vleugelprofiel dat de vervormingsmechanismen beïnvloedt, wat nodig is om de RDT-resultaten naar dergelijke geometrieën uit te breiden. Zoals eerder vermeld, wordt deze parameter geïdentificeerd als het pad dat de turbulente wervelingen afleggen van het stagnatiepunt tot de positie van maximale oppervlakte-drukfluctuaties, hetgeen op zijn beurt verband houdt met de stromingsacceleratie en de radius van de leading-edge. De nauwkeurigheid van deze methode voor het verbeteren van geluidsvoorspellingen wordt aangetoond met numerieke en experimentele resultaten van verschillende vleugelprofielen met turbulentie gegenereerd door een turbulentierooster.

Tenslotte, wordt er aandacht besteed op de toepassing op rotoren. Het model van Amiet voor het voorspellen van turbulentie-interactiegeluid bij rotoren wordt aangepast om puntsgewijze snelheidsmetingen als invoer te gebruiken. Dit wordt bereikt door gebruik te maken van een inverse striptheoriebenadering en het driedimensionale turbulentiespectrum, dat de instromingscondities modelleert, om te zetten in een eendimensionale term. Deze aanpassing verbetert het low-fidelity model op twee belangrijke manieren. Ten eerste maakt het de toepassing mogelijk in gevallen waarin turbulentiemodellering niet beschikbaar is of een gedetailleerde karakterisering van de instroom onpraktisch is. Zo kunnen bijvoorbeeld hot-wire anemometrie van de binnenkomende turbulentie worden gebruikt voor de akoestische voorspelling. Ten tweede, doordat de conversie van de turbulentiecomponent de introductie bevat van twee nieuwe functies die de spanwise en axiale correlaties van de turbulentie beschrijven, creëert deze aanpak een

raamwerk voor de theorie van Amiet waarin de bijdragen aan turbulentie-vervorming en geluidsverstrooiing afzonderlijk worden geanalyseerd en gemodelleerd. Deze “modulaire” structuur maakt een onafhankelijke analyse van deze bijdragen mogelijk, wat de toepassing van het model van Amiet op complexe stromingsconfiguraties en rotorgeometrieën mogelijk maakt. De voorgestelde methode is succesvol gevalideerd aan de hand van experimentele resultaten uit een vereenvoudigde opstelling voor turbulentie-interactie, waarbij een propeller met twee bladen een wisselwerking aangaat met een turbulentierooster bij drie verschillende advance-ratio's.

De bevindingen van dit onderzoek kunnen worden samengevat in de volgende conclusies, die elk direct betrekking hebben op de oorspronkelijke onderzoeksvragen:

1. Turbulentie-vervorming, gerelateerd aan de stompheid van het vleugelprofiel, veroorzaakt een verandering in het snelheidsveld in de stagnatieregio, wat de tijdsafhankelijke oppervlaktedruk en dus de geluidsproductie beïnvloedt.

2. Effecten van turbulentie-vervorming moeten in overweging worden genomen bij het stagnatiepunt om de low-fidelity voorspelling te verbeteren. Dit kan worden gedaan met behulp van asymptotische resultaten van RDT, uitgaande van onvervormde stroomopwaartse stromingscondities.

3. De aanpassing van het model van Amiet maakt het mogelijk om de invloed van instromingscondities op geluidsproductie en -voorspelling te analyseren en maakt de toepassing mogelijk van modellen voor turbulentie-vervorming die zijn ontwikkeld voor rechtlijnige beweging.

1

INTRODUCTION

1.1. ENVIRONMENTAL NOISE

A wide range of human activities and infrastructure generates environmental noise, defined as “unwanted or harmful outdoor anthropogenic sound, including noise emitted by means of transport, road traffic, rail traffic, air traffic and from sites of industrial activity" [1] (Fig. 1.1). The consequences of prolonged and elevated exposure to such noise sources can be detrimental at multiple levels. According to the World Health Organization (WHO), high noise levels can indeed adversely affect human health. This makes noise pollution a serious concern and the second leading environmental cause of ill health in Western Europe, surpassed only by air pollution from fine particulate matter [1, 2]. In addition, environmental noise pollution can exacerbate social inequalities. Generally, lower-income individuals, who often cannot afford to live in quiet neighbourhoods or well-insulated homes, are disproportionately affected. Poor environmental quality, particularly due to aircraft noise, can indeed depress local housing prices, making properties more affordable and thereby attracting lower-income residents, reinforcing a vicious cycle [3]. Anthropogenic noise also poses a significant threat to wildlife, disrupting critical behaviours and thereby impacting the distribution and population size of several animal species [1]. All these factors make environmental noise pollution a significant health, social, and environmental problem, underscoring the need to address its reduction through both normative frameworks and technological solutions.

1.1.1. REGULATORY FRAMEWORK

The main legislative instrument of the European Union for the assessment and management of environmental noise is the Environmental Noise Directive (END) [4]. Its primary goal is not to impose binding noise limits or specific mitigation measures, but is indeed to encourage coordinated action among EU institutions, national governments, and local authorities by establishing a consistent methodology and shared knowledge base for setting noise limits and shaping policy. To support consistent noise pollution assessment, mapping and planning [5], the Directive defines key noise indicators: L_{den}

1

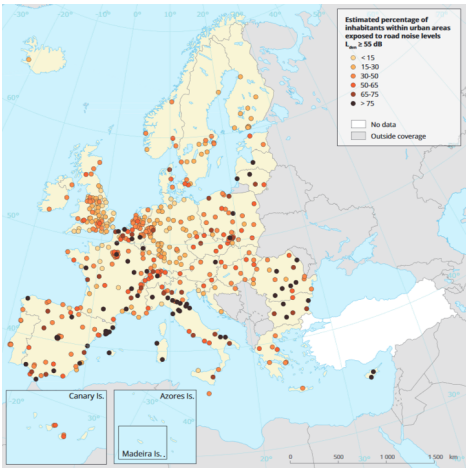

(a) Road noise

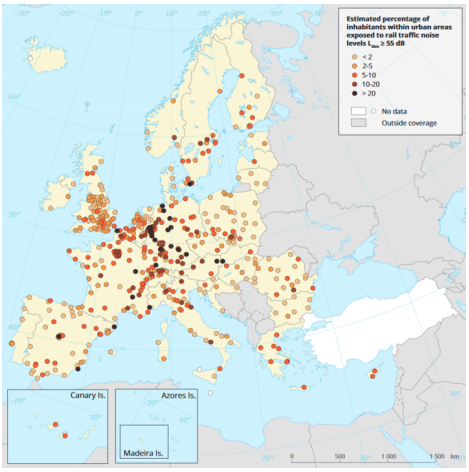

(b) Rail noise

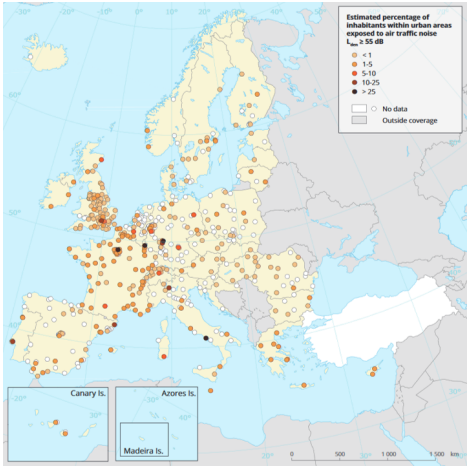

(c) Air traffic noise

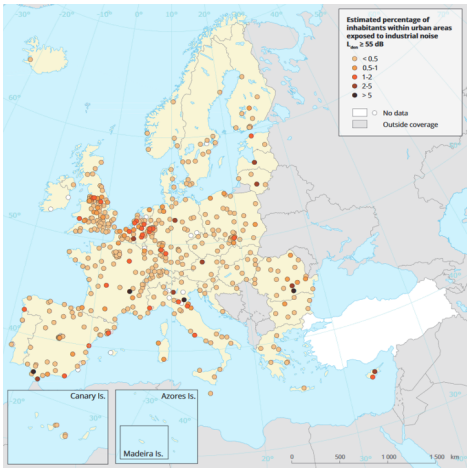

(d) Industrial noise

Figure 1.1: Percentage of inhabitants in urban environments in the European Union exposed to four different sources of environmental noise. Pictures from EEA [3].

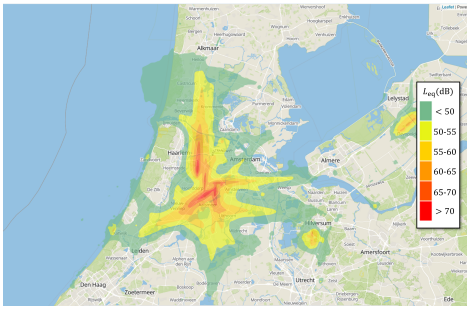

(a) Schiphol, Amsterdam, The Netherlands

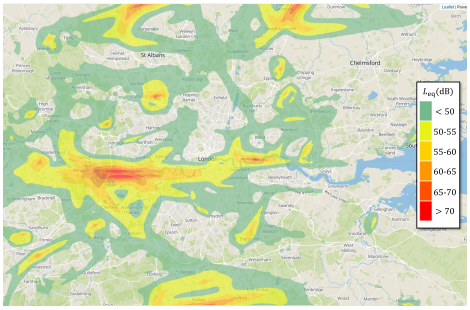

(b) Heathrow, London, United Kingdom

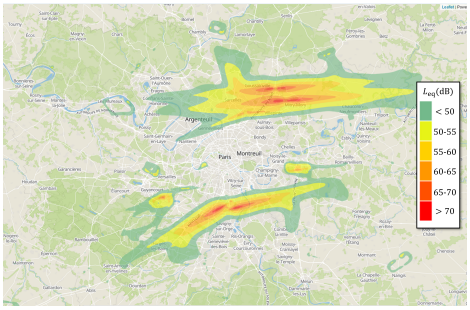

(c) Charles De Gaulle, Paris, France

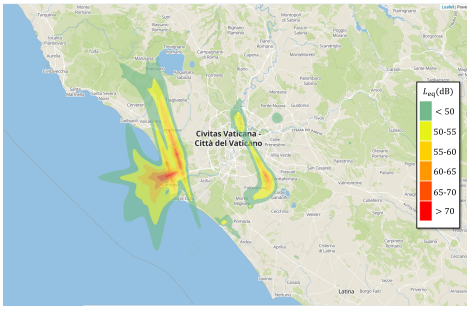

(d) Fiumicino, Rome, Italy

Figure 1.2: Flight noise maps from four of the largest airports in the European Union for passenger traffic. Images `https://noise-map.com/` and data from Lukas Martinelli `https://github.com/lukasmartinelli/osm-noise-pollution`.

(day-evening-night level) and L_{night} (night-time level). These are defined as the A-weighted long-term average sound level as defined in ISO1996-2:1987 [6], determined, respectively, over all the day, evening and night periods and over all the night periods of a year. The prescribed maximum values are set at 55 dBA for the day-evening-night period and 50 dBA for the night period, respectively. The latest implementation report highlights the urgent need to intensify existing regulatory and technological efforts [7]. Many national noise limits remain well above the prescribed thresholds [8], and without stronger and more widespread measures, the EU is unlikely to achieve its target of reducing the number of people affected by environmental noise by 30 % by 2030, as defined in the Zero Pollution Action Plan [9].

1.1.2. WIND TURBINE NOISE IN THE INDUSTRIAL AND ENERGY SECTOR

For industrial noise, research remains limited, and potential health impacts are not yet well understood [2]. This also applies to wind turbine noise, for which only limited and uncertain evidence exists regarding its associated health effects. The END does not consider this noise source [3], but the WHO [2] recommend maintaining average noise exposure below 45 dBA L_{den}. However, most national limits remain considerably higher

than these recommendations, and exceedances for industrial and wind turbine sources often lead to operational restrictions or prohibitions, creating significant obstacles for wind energy deployment. Many turbines must operate at reduced power during the night, and in some cases, plans for entire wind farms are cancelled. For new installations, blade length and maximum rotational speed, and therefore energy output, are often limited by noise constraints. As a result, increases in rated power output must rely on higher torque, which in turn entails a significant increase in the cost of drivetrain components. Research on the health impacts of acoustic emissions in this sector remains limited and of low or very low quality, with systematic reviews yielding inconsistent conclusions [2]. What emerges clearly, however, is that beyond measurable sound levels, perception and social factors play a key role: surveys indicate that the characteristic "swishing" sound of turbines is particularly annoying compared with other noise sources, while annoyance is reduced when residents perceive fair procedures or share in economic benefits [10]. These findings underscore the urgent need to improve both the understanding and mitigation of wind turbine noise, supporting the development of renewable energy in a manner consistent with public health protection.

1.1.3. AVIATION NOISE IN THE TRANSPORT SECTOR

The Zero Pollution Action Plan places its primary focus on reducing transport noise [9]. This is dominated by road traffic, but targeted efforts are also required for the railways and aviation sectors to reduce noise emissions. Aviation noise, for example, is characterised by a lower overall exposure in Europe compared to road or rail transport, but people affected by aircraft noise tend to report higher levels of annoyance [11]. Figure 1.2 illustrates the considerable impact of aviation noise on urban communities, showing flight noise maps from four of the largest airports in the European Union. For this sector, mitigation involves a combination of quieter operational procedures, modernising aircraft fleets, and limiting night-time traffic. These measures are guided by Regulation (EU) No 598/2014, which sets out the rules and procedures for noise-related actions at airports [7]. Notably, aviation is the sector where the largest reduction in noise exposure is projected by 2030 [7]. At present, the WHO recommends aircraft noise levels below 45 dB L_{den} and 40 dB L_{night}, yet millions in Europe are exposed to levels roughly 10 dB higher than these limits [2, 5]. Reducing and stabilising aviation noise by 2030 depends on successfully implementing all the planned technological improvements described in the European Aviation Environmental Report [12]. At the same time, if flight volumes increase significantly, even better aircraft designs might only keep noise at current levels rather than lowering it. This context helps to explain the significant efforts directed toward investigating and reducing noise in the field of air transport.

1.1.4. AERODYNAMIC NOISE

In the aviation sector, the most significant sources of noise emissions are the aeroacoustic ones, i.e. those generated aerodynamically. The same holds true for the rapidly evolving Urban Air Mobility (UAM) sector and the wind energy industry, where aeroacoustic noise remains a major obstacle to the integration and acceptance of these technologies in or near urban environments [10]. The ongoing challenge of investigating and reducing noise has driven long-term research and interest in the field of aeroacoustics, originally

sparked by the need to reduce jet noise from early aeroengines, as the widespread diffusion of jet aviation in the 1960s and 1970s made aircraft noise a major concern for communities near airports. Since then, numerous other flow-induced noise sources have been identified, studied, and, in some cases, mitigated. In fixed-wing aircraft, the reduction of jet noise and the rise of turbofan engines highlighted additional contributors to overall emissions, notably noise from landing gear and high-lift devices. Thereafter, the development of helicopter technology spurred extensive research into flow-induced sources related to rotational motion, including trailing-edge noise (classified among “self-noise" sources), blade–vortex interaction noise, and turbulence–interaction noise, which result from the interaction with the incoming airflow. More recently, significant attention has been given to the expanding wind energy sector and urban air mobility (UAM), both affected by many of the same mechanisms observed in aviation.

Among the different flow-induced noise sources discussed above, turbulence-interaction noise remains a particularly challenging and critical issue due to the diversity and heterogeneity of the affected applications, which makes its investigation and control especially difficult. Indeed, the interaction mechanisms differ substantially across the various configurations previously mentioned: an aeroengine, the rotor of a UAM vehicle, a wind turbine, a ventilation fan, or a helicopter. These applications differ in several fundamental aspects. For instance, the flow regime varies significantly when considering the wide range of Reynolds numbers and rotational speeds involved. Similarly, the inflow conditions, such as turbulence characteristics, scales, and intensity, can differ dramatically. The large-scale atmospheric turbulence encountered by a wind turbine or helicopter is entirely unlike the small-scale, nearly homogeneous turbulence generated by a heat exchanger interacting with a ventilation fan. Likewise, the inflow of a UAM vehicle is influenced by the complex, unsteady wake structures characteristic of urban environments, while in an aeroengine, the inflow is shaped by the stator wake impinging upon the downstream rotor. Additionally, the significant variations in rotor and blade geometries among these applications further influence the nature of the flow interactions and the resulting noise generation. This phenomenon is especially evident in wind turbines, where the continuous increase in blade size to maximize energy capture has resulted in thicker blades that appear to influence acoustic emissions, although the precise effects are not yet fully understood [13, 14]. The ongoing challenge to physically characterise and model all these different configurations explains why turbulence-interaction noise remains a central topic in aeroacoustic research. The next section provides an overview of the state of the art in terms of physical characterisation and low-fidelity prediction, focusing respectively on turbulence–interaction noise in rectilinear and rotational motion.

1.2. TURBULENCE-INTERACTION NOISE: GENERATION AND PREDICTION

Turbulence-interaction noise is a flow-induced sound source produced by the interaction of incoming turbulence with an aerodynamic surface. Such a sound-generation mechanism may arise for a wing in rectilinear motion or a blade in rotational motion, with only the turbulence-interaction physics differing between the two flow configura-

tions.

The earliest identification and analytical modelling of this noise source dates back to the seventies [15–19], but several factors justify the long-standing academic and industrial interest in its analysis, as noted earlier: the successful results achieved in the reduction of other prevailing noise sources [20, 21], its relevance in high-speed applications, e.g. propellers and rotors in propulsive systems [19, 22, 23], as well as low-speed ones, e.g. fans in cooling systems or wind turbines [10, 13, 24], and the complexity of the physics involved in the sound production in such diverse applications. These physical mechanisms deserve particular attention, as the accuracy of their description and modelling affects the reliability of low-fidelity noise-prediction models. Such models play a crucial role in the design and optimisation of wings and blades due to their lower computational cost compared to numerical simulations. In this case, far-field acoustic pressure is derived from a statistical characterisation of the flow field using analytical or semi-empirical relations to model sound-production mechanisms.

As the physical mechanisms involved in the turbulence interaction and low-fidelity modelling through semi-empirical or analytical formulations differ significantly between rectilinear and rotational motion, these will be introduced separately hereafter. To avoid confusion between the two configurations, two alternative terms, drawn from the range of definitions found in the literature, will be adopted in place of turbulence-interaction noise throughout this work, depending on the context. The term *leading-edge noise* will refer to cases involving rectilinear motion, while *turbulence-ingestion noise* will be used for rotational motion.

1.2.1. RECTILINEAR-MOTION CONFIGURATION

The generation of turbulence-interaction noise in rectilinear motion represents the simplest configuration for this flow-induced sound source and most closely approximates an idealised model setup. The interaction that occurs in rotational motion is essentially the same, but it involves additional dynamics associated with more complex turbulence interactions. Consequently, although turbulence-interaction noise in rectilinear motion is relevant to only a few practical applications, this configuration has nevertheless become the focus of a substantial body of dedicated literature, as it has long served as a simplified reference case for analysing and modelling the same mechanism in rotational motion.

The most common low-fidelity model for predicting turbulence-ingestion noise, as will be discussed later on, is based indeed on the leading-edge model proposed by Amiet [16] for a fixed-wing configuration. In this semi-analytical method, the power spectral density (PSD) of the far-field noise produced by a flat plate in a subsonic turbulent flow is related to the characteristics of the upstream turbulence by means of a transfer function that models the surface response to a sinusoidal gust. The agreement with the experimental data was shown to be satisfactory for flat plates and thin aerofoils, in particular for high-speed flow [17, 25]. Nevertheless, the accuracy of the method decreases in the case of thicker aerodynamic surfaces, in particular in the high-frequency range, as pointed out by Paterson and Amiet [17]. Such a discrepancy was attributed to the fact that the model does not take into account effects due to the real geometry of the blade. The breakdown of the theory was observed to occur for Strouhal numbers $f\,t/U_\infty \geq 1$, with f being the sound frequency, t the thickness of the body, and U_∞ the free-stream velocity,

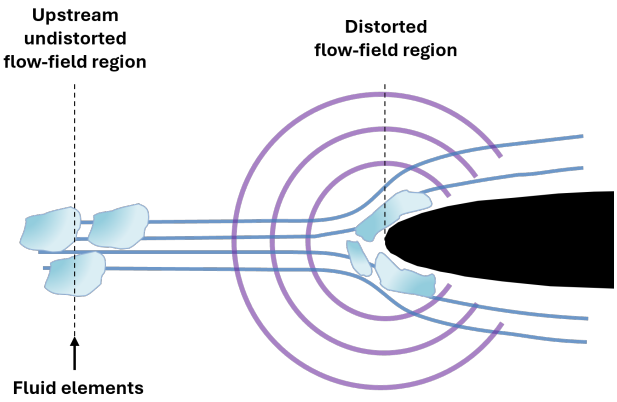

Figure 1.3: Noise produced in rectilinear motion by the interaction of incoming turbulence with an aerofoil leading-edge.

i.e. for wavelengths of the incoming turbulent structures smaller than the thickness of the aerofoil. Indeed, the deformation undergone by these structures during the interaction with a thick leading edge is not taken into account in the model, which adopts as input a canonical turbulence spectrum, such as the von Kármán or the Liepmann ones.

The effects of the aerofoil geometry on its aerodynamic and acoustic response were confirmed by the analytical study of Goldstein and Atassi [26], which was based on the distortion of a gust described as a small vortical disturbance convected by the mean flow. The model showed that the influence of the thickness on the streamlines could lead to an additional deformation of the incoming gusts, causing a variation of the unsteady lift in the high-frequency range. A following experimental investigation by Olsen and Wagner [27] corroborated this result from an acoustic point of view by reporting a far-field noise attenuation in the high-frequency range as the thickness increases. Atassi et al. [28] and Lockard and Morris [29] extended these findings by noticing that the effects of thickness occurred for gust wavelengths shorter than the aerofoil chord and mostly for downstream observer locations. Glegg and Devenport [30] showed that, for blade-vortex interaction, the peak of unsteady lift on the leading edge due to the passing of a vortex is reduced when the vortical element is closer to the surface and moves downstream when the thickness of the aerofoil increases, also experiencing a further decrease. In subsequent work, Glegg and Devenport [31] employed a panel method to develop a noise-prediction model able to capture this high-frequency attenuation due to the thickness, improving the prediction of Amiet's model.

Further investigations have been conducted to determine how the geometrical characteristics of the aerofoil impact the distortion of incoming turbulent eddies and affect far-field noise. In a series of wind tunnel tests, Oerlemans [32] found that the shape of the leading edge, more precisely its *sharpness*, could affect noise-generation efficiency, with more rounded aerofoils producing less noise. The same direction was taken in the experimental investigation of Hall et al. [33], who modified the leading-edge shape by altering the first 10% of an *ad-hoc* designed aerofoil. The maximum noise reduction

was obtained at reduced frequencies, computed with respect to the leading-edge thickness, of the order of 1. It was hypothesised that the changes in the flow incidence affected the noise generation, thus highlighting the relevance of the pressure distribution over the aerofoil on far-field noise and excluding a unique dependence on the relation between the incoming turbulence scale and the leading-edge thickness. The effects of turbulence distortion on noise generation and the role of aerofoil geometry were investigated through an extensive experimental campaign by Chaitanya et al. [34], who concluded that the aerofoil thickness and leading-edge shape are the main geometrical characteristics affecting the noise-generation efficiency, with the latter being particularly relevant in the high-frequency range. No significant effect of camber and angle of attack was found, as also confirmed experimentally by Devenport et al. [35], in the case of isotropic turbulence interacting with the aerofoil. Gill et al. [36] conducted a systematic study using a code solving the linearised Euler equations to investigate the role of aerofoil thickness and leading-edge radius in high-frequency noise attenuation. The analysis was carried out using single-frequency harmonic gusts interacting with several NACA 4-digit aerofoils. Interestingly, the noise mitigation obtained by increasing the leading-edge radius was shown to be smaller and occurred at higher frequencies than that obtained for larger thicknesses. In particular, an overprediction of Amiet's model was observed for ratios of $c/\lambda > 4$, c being the chord of the aerofoil and λ the wavelength of the perturbating gust, for increasing leading-edge radii, and for ratios of $c/\lambda > 1$ for increasing aerofoil thicknesses. In both cases, the noise reduction associated with thicker aerofoils was more evident for downstream observer positions, while an increase was observed in upstream positions in the case of larger leading-edge radii. The authors attributed these effects to the distortion of the vortical gusts due to the velocity gradients present in the stagnation region, which caused the gust wavefront to be smoothed and its amplitude to decrease. Bowen et al. [37] assessed the influence of turbulence characteristics on leading-edge noise by experimentally investigating alterations to the velocity field and surface-pressure distribution in the stagnation region of an aerofoil. The sound-production efficiency was shown to be directly related to the intensity and the integral length scale of the incoming turbulence, which also affects the energy levels of the surface-pressure spectra on the leading edge. At the same time, it was concluded that the noise generation at the leading edge was mainly induced by the flow field in the vicinity of the stagnation point.

Several approaches have been developed to enhance the accuracy of leading-edge noise prediction by taking into account aerofoil thickness effects. An analytical procedure was followed by Guidati et al. [38], who employed a boundary-element method to model the sound generated by point vortices convected along the mean-flow streamlines to formulate a correction to Amiet's model. Subsequently, Moriarty et al. [25] showed that such a combination was able to provide a satisfactory agreement with the experimental data in terms of the spectrum decay slope at different angles of attack and Mach numbers, but a tuning constant of 10 dB had to be added to the prediction. Moreover, a significant underestimation was still observed in the high-frequency range in comparison to the measurements for thicker aerofoils. Gershfeld [39] obtained good agreement with the experimental measurements of Paterson and Amiet [17] by implementing an exponential function to model the effects of aerofoil thickness on noise radiation. The cor-

rection was based on a rigid surface Green's function taking into account aerofoil thickness and back-scattering due to the aerofoil non-compactness [40]. In addition, Lysak et al. [41] and Kim et al. [42] observed that the aerofoil thickness causes an exponential decay in the high-frequency range for the unsteady response of the blade and the far-field noise, respectively. In both of their works, a correction factor for flat-plate-based noise-prediction models was developed in the form of an exponential function of the Mach number, aerofoil thickness, and leading-edge thickness by fitting the respective reference data, with which a good agreement was shown.

Recent efforts have focused on describing the alteration of the turbulent flow field in the interaction with the aerofoil to account for turbulence-distortion effects in existing low-fidelity noise-prediction methods. The problem of the deformation of turbulent structures was first investigated by Prandtl [43] and Taylor [44], who studied the distortion of the vorticity field in the contraction section of a wind tunnel. The rapid distortion theory (RDT) was then formulated by Hunt [45], starting from the works of Ribner and Tucker [46] and Batchelor and Proudman [47], to model the changes that the velocity field experiences in the interaction with a bluff body. The RDT assumes the distortion of the turbulent structures to occur rapidly enough to yield a negligible contribution from the turbulence to the relative motion of the fluid particles when these are convected through the non-uniform mean flow region. Moreover, the velocity fluctuations of the incoming flow are supposed to be small compared with the free-stream velocity. In his work, Hunt carried out a wavenumber analysis to compute the homogeneous turbulent flow past a circular cylinder. Velocity spectra and variances were derived in the asymptotic cases where the turbulence integral length scale L_1 can be considered much smaller or larger than the characteristic dimension of the bluff body a, e.g. the radius in the case of the cylinder. The results of this investigation identified different mechanisms by which turbulent structures are deformed according to the ratio L_1/a. In particular, for $L_1/a \gg 1$, the prevailing distortion mechanism is due to the blockage imposed by the presence of the body, which causes a momentum transfer between the streamwise and the upwash velocity components of a fluid element approaching the cylinder along the stagnation streamline. As a result, the streamwise velocity fluctuations decrease near the surface while the upwash ones increase. For small-scale structures ($L_1/a \ll 1$) or high wavenumbers of the incident turbulence, the dominant distortion mechanism is determined by the deformation of the vorticity field due to the deflection of the streamlines upstream and around the body. The altered vorticity field, in turn, induces changes in the velocity fluctuations depending on the stretching or shortening of the vortex lines as they are convected towards the surface. In particular, the streamwise and spanwise velocity fluctuations increase while the upwash ones decrease, leading to a steeper decay slope of the spectrum of the latter at high wavenumbers.

The variation of the high-frequency decay of the upwash velocity component spectrum was used by Moreau and Roger [48] to modify the von Kármán spectrum, which serves as an input in Amiet's model to describe the incoming turbulence. This approach, even though limited to the investigated case and relying on two case-specific constants, made it possible to improve the agreement with the experimental data obtained for a NACA 0012 and confirmed the potential benefit in terms of noise-prediction accuracy achievable by accounting for turbulence distortion. Similar approaches were proposed

by Christophe [49], De Santana et al. [50], and dos Santos et al. [51, 52]. They attempted to generalise the methodology of Moreau and Roger [48] imposing the conservation of variance with respect to the upstream undistorted flow conditions. However, this approach neglects the alteration of the spectrum in the low-wavenumber range and the increase of the root-mean-square of the velocity fluctuations, which indicates a variation of the gust energy as it approaches the leading edge. This limitation, together with the reliance on the identification of a position in the stagnation region where the turbulence characteristics should be sampled to scale the turbulence spectrum, limits the generality of the correction, as pointed out by the same authors. The application of the RDT to aerofoils relies on the identification of an equivalent characteristic dimension a, which has yet to be conclusively identified. Mish and Devenport [53, 54] proposed the leading-edge radius, while dos Santos et al. [55] argued that the average aerofoil thickness before the position of maximum thickness is the appropriate dimension to consider.

The effect of realistic geometrical parameters on the accuracy of the noise prediction was also investigated by assessing the role of the aeroacoustic transfer function in Amiet's model. This function, related to the pressure jump across the body due to the interaction with an incoming perturbation, can be expressed analytically in the case of a flat plate, whereas more cumbersome numerical and analytical procedures are required for real geometries. De Santana [56] carried out an extensive analysis taking separately into account the compact and non-compact frequency regimes. In the former case, adding two iterations of the Schwarzschild theorem to the two performed in the original formulation of Amiet proved to reduce the overprediction of noise levels in the low-frequency range. In the non-compact frequency regime, the Helmholtz equation prescribed by the linearised aerofoil theory was solved numerically with the purpose of improving the modelling of realistic aerofoil geometries. The procedure yielded acceptable results and, most interestingly, highlighted the crucial role played by the aerofoil thickness on the acoustic radiation of the body, whose main effect is a reduction of the noise prediction at higher frequencies. The methodology proposed for the compact regime followed the work of Christophe [49], who extended to the case of inflow-turbulence noise the approach carried out by Roger and Moreau [57] and Moreau and Roger [58] to include back-scattering effects in Amiet's theory for trailing-edge noise. A further advancement in this direction was proposed by Bresciani et al. [59] to improve the accuracy of low-frequency noise prediction. Their contribution introduced a novel approach aimed at generalising the calculation of the second iteration of the Schwarzschild theorem within Amiet's theory, which is required to predict back-scattering effects. This formulation eliminates the need for the regularisation and corrective procedures commonly employed in the literature and has proven particularly effective for acoustically compact aerofoils. A numerical approach to model the effects of aerofoil realistic geometries was proposed by Miotto et al. [60], who applied a boundary-element method to calculate the compressible aeroacoustic transfer function of an aerofoil of non-negligible thickness but still described by linearised theory. They demonstrated that, when compressibility effects are small, the aerofoil thickness causes the loading distribution to decrease, reducing, in turn, the noise generation. On the contrary, the surface loading and, hence, the noise scattering were observed to increase when compressibility effects become significant.

All the body of work mentioned above has shown that the distortion of turbulent structures in the interaction with a solid body can significantly affect leading-edge noise generation, and that low-fidelity methods can benefit from the modelling of these effects. However, a scattered framework emerges for the enhancement of leading-edge noise predictions in the case of realistic aerofoil geometries. Regarding the description of the altered turbulent field interacting with the aerofoil, the RDT has played a seminal role, although several shortcomings limit the general validity of currently implemented methodologies. As they lack support from a thorough physical investigation, these methods are hardly generalisable and rely on empirically tuned input parameters and the choice of a sampling location to evaluate turbulence characteristics. Conversely, procedures developed to improve the modelling of the acoustic response via the aeroacoustic transfer function still depend on cumbersome numerical methods. What emerges is a clear gap in the literature that must be addressed. First, an accurate physical investigation is required to analyse noise-generation mechanisms induced by turbulence interaction with aerofoil geometries. Second, there is the need for a systematic and general corrective approach to account for the aerofoil-geometry effects in leading-edge noise prediction, which has yet to be defined.

1.2.2. ROTATIONAL-MOTION CONFIGURATION

As previously noted, interest in turbulence-interaction noise was driven by applications involving rotational motion, particularly in helicopters and aeroengines. Since the late 2010s, however, research on this flow-induced noise has progressively increased and extended into additional sectors. This trend was initially driven by the widespread development of onshore wind farms, which require substantial noise mitigation efforts. More recently, the growing interest in UAM has renewed attention to this type of noise source [61]. Indeed, this field has experienced rapid expansion in recent years, with a diverse range of potential applications envisioned for this technology. This has driven considerable growth in research efforts. In particular, significant focus is being directed toward the optimisation of the acoustic performance of rotors, dominated by aerodynamic noise, as it represents one of the main obstacles to the diffusion of UAM [62, 63]. The investigation of turbulence-ingestion noise is especially important due to the highly turbulent flows characterising urban environments, where UAM vehicles are planned to operate and where minimisation of acoustic emissions is crucial. In addition, for UAM vehicles, the broadband noise component may not only be comparable to the tonal one, a key difference from previously studied rotorcraft applications, but also practically overlaps with the human hearing range [61, 64, 65].

The noise generated by the unsteady surface pressure induced by turbulence being ingested on the blades was investigated and modelled for the first time by Sharland [66] for the case of a fan. Sound is generated by a wide range of turbulence scales, ranging from the diameter of the rotor to the thickness of the blade [67]. These turbulent structures are deformed by the rotor-induced streamtube, as first shown by Hanson [68]. This implies that, even assuming a state of homogeneity and isotropy for the turbulence far away from the rotor, noise is actually generated by the interaction of anisotropic turbulence with the blades. In particular, Hanson [68] showed that the contracting streamtube induces a stretching of the turbulent structures into elongated eddies, which

are hence prone to be cut multiple times by the passage of different blades. This mechanism, defined as blade-to-blade correlation, causes partially coherent unsteady surface pressure on different blades, adding quasi-tonal peaks at the blade-passage frequency (BPF) harmonics to the mainly broadband characteristics of the turbulence-ingestion noise spectra. This narrow-band noise feature is also referred to as haystacking [69]. Hanson [68] also developed a model for sound prediction, using flow-field measurements and surface pressure as input to characterise the statistical distribution of eddies. These were incorporated into random pulse-modulation theory to calculate the unsteady blade forces and the resulting noise.

Hanson's work laid the foundation for the study of Majumdar and Peake [70], who employed RDT, following Goldstein's formulation [71], to account for turbulence distortion in the streamtube in the case of an aero engine. The same approach was also used by Simonich et al. [67, 72] and Amiet et al. [22] to investigate turbulence-ingestion noise in helicopters. Their findings demonstrated that turbulence distortion is influenced by the operating conditions of the rotor, since the contraction of the streamtube varies with the operating regime. Specifically, they observed significant turbulence alteration at low free-stream velocities, such as in hover and low-speed ascent, where the streamtube contraction is most pronounced. In contrast, in forward flight and high-speed ascent, the deformation of turbulent structures is less pronounced. The model was also capable of accounting for the effects of blade-to-blade correlation (referred to as "B2B" from now on).

The theory of Amiet [73] was based on the formulation developed for a wing in rectilinear motion, for which radiated sound was related to the inflow-turbulence spectrum through the aerodynamic and acoustic response of a linearised aerofoil, i.e., a flat plate [16]. This framework was extended to the rotational motion by assuming that it could be approximated to a rectilinear one. This assumption holds for acoustic frequencies significantly larger than the rotor rotational speed. Amiet's approach overcame the low-frequency limitations of the earlier model by Homicz and George [74], which treated the blade as a moving dipole source by relying on a low-frequency response function and a blade-compactness assumption to compute unsteady loading and the resulting acoustic pressure field. Amiet's model has thus emerged as the most robust and feasible theory for low-fidelity turbulence-ingestion noise prediction. This has recently been confirmed by Raposo and Azarpeyvand [69], which proved that the model can effectively capture both broadband characteristics and narrow-band haystacking features despite all assumptions regarding blade geometry and inflow conditions.

Therefore, in a simple turbulence-rotor interaction configuration, two intrinsically related and consecutive physical mechanisms characterise the interaction: the elongation of turbulent structures due to streamtube contraction and their subsequent repeated chopping by multiple blades. In theory, another physical mechanism is expected to influence turbulence alteration during its interaction with the blades, thereby affecting noise generation and prediction. This is the deformation induced by the flow that accelerates along the leading edge itself, investigated and modelled by several studies [50, 51], which proved its relevance in high-frequency noise in the two-dimensional regime in the case of blunt aerofoils. No studies currently investigate or model this effect for rotating blades, but this is expected to play a significant role in the case of small-scale

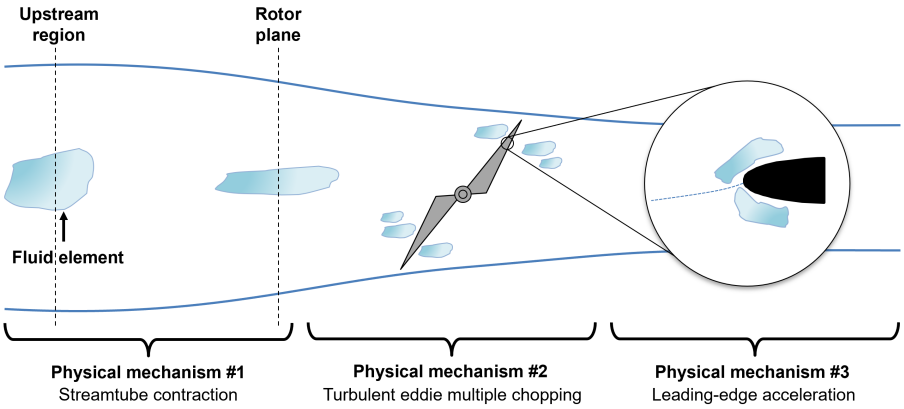

Figure 1.4: Physical mechanisms undergone by turbulence approaching a rotor.

turbulence relative to the leading-edge radius, e.g. for thick blades, and at significant pitch angles [75]. A conceptual representation of turbulence alteration in the interaction with a rotor is reported in Fig. 1.4.

Different yet equally complex phenomena govern the interaction between incoming turbulence and a wind turbine (or, more generally, any rotor performing negative work on the fluid), for which the streamtube is actually diverging. In such cases, the stronger variation in cross-sectional area, resulting from the higher aerodynamic loading of turbines compared with propellers, leads to a more pronounced alteration of the turbulence structures. Furthermore, the ongoing trend toward increasing blade lengths to enhance rated power output is accompanied by a progressive thickening of the blade sections, meaning that distortion mechanisms occurring at the leading-edge because of aerofoil thickness are expected to become increasingly significant.

The studies mentioned above clearly demonstrate the complexity of the physical mechanisms underlying turbulence-interaction noise generation and modelling. Moreover, in the case of rotors, the growing variety of configurations and operating conditions envisioned for UAM vehicles has led to increasingly heterogeneous and complex geometries and inflow conditions. In addition to the previously discussed distortion mechanisms, these factors introduce new and unexplored interactions that can influence noise generation. This highlights the need for further research on low-fidelity noise prediction, emphasising the importance of direct physical investigations before engaging in any modelling efforts [76].

1.3. THESIS OBJECTIVES AND STRUCTURE

This work presents an enhanced methodology for describing and modelling turbulence-distortion effects to improve the accuracy of a low-fidelity prediction of turbulence-interaction noise. The approach begins by analysing rectilinear motion and is then extended to more realistic full-scale applications, which predominantly involve configur-

ations operating in rotational regimes. The investigation has thus been structured into conceptually consecutive phases, each with a clearly defined objective, as outlined below:

1. **PHYSICAL ANALYSIS**: description of turbulence distortion mechanism in the case of an aerofoil of non-negligible thickness and assessment of the impact on noise generation and prediction;

2. **ANALYTICAL MODELLING**: development of an analytical framework to incorporate turbulence-distortion effects into low-fidelity noise prediction tools;

3. **FULL-SCALE APPLICATION**: establishment of the physical and analytical framework needed to evaluate the impact of these advancements in the context of rotational motion.

This structure mirrors the layout of the manuscript. Following an overview of the relevant theoretical background in Chapter 2 and a description of the experimental and numerical setups in Chapter 3, the physical analysis of turbulence-interaction noise is presented in Chapter 4. The effects of turbulence distortion on noise generation are examined for grid-aerofoil configuration, and a potential approach is proposed to enhance the accuracy of low-fidelity prediction methods by accounting for these effects. This first conceptual phase aims to lay the physical foundation for the subsequent stages of the work and to address the previously identified gap in the literature concerning the incorporation of turbulence-distortion effects into low-fidelity models of turbulence-interaction noise. At present, the way in which this mechanism should be represented remains unclear, and existing models lack a comprehensive physical justification. The physical framework developed in this phase is therefore essential to support the analytical modelling of this mechanism, presented in Chapter 5. This chapter details the analytical methodology developed to model turbulence-distortion effects using a limited set of commonly available turbulence characteristics and to include these effects in Amiet's model. This methodology is validated through numerical simulations of symmetrical and cambered aerofoils with varying geometries and loading conditions, as well as experimental data involving aerofoils of increasing thickness. The intent is to address the previously mentioned need for a general corrective approach to account for turbulence-distortion effects influencing noise-generation mechanisms in thick aerofoil geometries. This advancement is achieved through a formulation based on simple closed-form RDT expressions in their original form, without relying on any empirical tuning, and whose application is, most importantly, supported and validated by the results from the physical investigation conducted in the first conceptual phase. Chapter 6 extends the analysis to rotational motion, detailing the modifications necessary to adapt Amiet's original low-fidelity model to implement the enhanced framework developed to describe and model turbulence alteration. From a broader perspective, these modifications extend Amiet's model and establish it as a robust and versatile low-fidelity prediction tool to estimate turbulence-interaction noise in complex flow and geometric configurations. Finally, Chapter 7 summarises the key findings of this work and outlines directions for future research.

2

THEORETICAL BACKGROUND

This chapter provides a concise yet comprehensive overview of the key analytical formulations employed in the present investigation. The first part introduces Amiet's theory in both its original formulation for rectilinear motion [16] and its subsequent extension to rotational motion [73]. Owing to its robustness and widespread adoption, this model serves as the foundational framework for the current analysis. Its relatively simple structure offers an ideal low-fidelity representation of turbulence-interaction noise, enabling effective evaluation of turbulence-distortion effects on noise generation and prediction.

The second part briefly outlines rapid distortion theory as developed by Hunt [45]. The primary assumptions and initial formulation of the problem are presented, with particular emphasis on the asymptotic results and their derivation. These results form the theoretical basis for the analytical corrections to Amiet's model discussed in Chapter 5 for aerofoils with non-negligible thickness.

For clarity, the notation for spatial coordinates and velocity used throughout this work is specified here. Coordinate systems are expressed by the vector

$$\boldsymbol{x} = \begin{pmatrix} x_1 \\ x_2 \\ x_3 \end{pmatrix}.$$

For velocities, mean and fluctuation are denoted as follows:

$$\boldsymbol{u} = \overline{\boldsymbol{u}} + \boldsymbol{u}' = \begin{pmatrix} \overline{u}_1 \\ \overline{u}_2 \\ \overline{u}_3 \end{pmatrix} + \begin{pmatrix} u_1' \\ u_2' \\ u_3' \end{pmatrix}.$$

The free-stream velocity is denoted by the subscript $_\infty$. Alternatively, in Chapter 4 and Chapter 5, $_{\text{ups}}$ is used for "upstream," in contrast to $_{\text{dis}}$, which denotes "distorted" flow conditions. The adopted notation is defined as follows

$$\overline{\boldsymbol{u}}_\infty = \begin{pmatrix} \overline{u}_{1,\infty} \\ \overline{u}_{2,\infty} \\ \overline{u}_{3,\infty} \end{pmatrix}, \quad \text{with} \quad \left|\overline{\boldsymbol{u}}_\infty\right| = U_\infty. \tag{2.1}$$

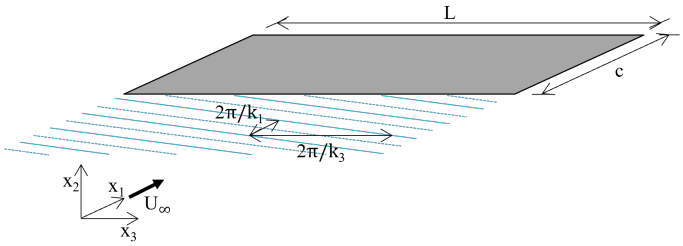

Figure 2.1: Sketch of the flat plate interacting with a turbulent gust considered in Amiet's theory.

2.1. AMIET'S MODEL

2.1.1. LOW-FIDELITY PREDICTION FOR RECTILINEAR MOTION

A brief summary of Amiet's theory is provided hereafter. The notation used is consistent with that employed by Amiet [16], but the axes (and consequently the notation for the velocity components) have been changed to be consistent with the reference system of the investigation carried out in this work (introduced in Chapter 3). The reference system is centred at the leading edge, x_1 is the streamwise direction, x_2 is the upwash direction, and x_3 is the spanwise direction. The spatial wavenumbers along the three directions are k_1, k_2, and k_3, respectively. A conceptual sketch is shown in Fig. 2.1.

Amiet's model relies upon two simplifying hypotheses: the turbulence is assumed to be *frozen* while convecting and impinging on the leading edge, and the aerofoil is considered to be an infinitely-thin flat plate of chord c and with large span L, thus neglecting the effects of thickness, camber, and angle of attack. These hypotheses allow the incident gust, with which the flat plate is interacting, to be modelled as a two-dimensional upwash velocity gust with amplitude $u_{2,0}$ and wavenumbers k_1 and k_3:

$$u_2(x_1, x_3) = u_{2,0} \mathrm{e}^{\mathrm{i}[k_1(U_\infty t - x_1) - k_3 x_3]}. \tag{2.2}$$

The pressure jump across the flat plate will be, hence, expressed as

$$\Delta p(x_1, x_3, t) = \pi \rho_\infty U_\infty \mathrm{c} u_{2,0} g(x_1, k_1, k_3) \mathrm{e}^{\mathrm{i}(k_3 x_1 - k_1 U_\infty t)}, \tag{2.3}$$

where $g(x_1, k_1, k_3)$ is the transfer function between the turbulent velocity and pressure jump, and ρ_∞ is the density. The pressure jump due to all the wavenumber components will hence be indicated by

$$\Delta p(x_1, x_3, t) = 2\pi \rho_\infty U_\infty \iint_\infty^\infty \hat{u}_{2,R}(k_1, k_3)\, g(x_1, k_1, k_3)\, \mathrm{e}^{i(k_3 x_3 - k_1 U t)} \mathrm{d}k_1 \mathrm{d}k_3, \tag{2.4}$$

with

$$\hat{u}_{2,R}(k_1, k_3) = \frac{1}{(2\pi)^2} \iint_{-R}^{R} u_2(x_1, x_3)\, \mathrm{e}^{-\mathrm{i}(k_1 x_1 + k_3 x_3)} \mathrm{d}x_1 \mathrm{d}x_3. \tag{2.5}$$

The variable R, large but finite, was employed in the original formulation to prevent convergence difficulties in the integration. By calculating the integration time as $T = R/U$, the Fourier transform with respect to time between $\pm T$ can be calculated, leading to

$$\Delta \hat{p}(x_1, x_3, \omega) = 2\pi \rho_\infty \int_\infty^\infty \hat{u}_{2,R}(K_1, k_3)\, g(x_1, K_1, k_3)\, \mathrm{e}^{i(k_3 x_3)} \mathrm{d}k_3. \tag{2.6}$$

The assumption of frozen turbulence has been used by considering $K_1 = -\omega/U_\infty$, which shows that a given frequency of the pressure jump is induced by the value $-\omega/U_\infty$ of the streamwise turbulent wavenumber. Equation (2.6) is obtained by taking into account that

$$\lim_{T\to\infty}\int_{-T}^{T} \mathrm{e}^{\mathrm{i}\xi t}\,\mathrm{d}t = 2\pi\delta(\xi).$$

Amiet showed that the cross-spectral density S_{QQ} of the pressure jump between two points on the surface with coordinates (x_1, x_3) and (x_1', x_3') can be expressed as a function of the two-dimensional wavenumber component $\Psi_{22}(k_1, k_3)$ via the transfer function $g(x_1, k_1, k_2)$

$$S_{QQ}(x_1, x_1', \eta, \omega) = (\pi\rho_\infty \mathrm{c})^2 \int_{-\infty}^{+\infty} g^\dagger(x_1, K_1, k_3)\, g(x_1', K_1, k_3) \times \Psi_{22}(K_1, k_3)\, \mathrm{e}^{\mathrm{i}k_3\eta}\,\mathrm{d}k_3. \quad (2.7)$$

$g^\dagger(x_1, k_1, k_3)$ is the complex conjugate of the transfer function $g(x_1, k_1, k_3)$, whereas $\eta = x_3' - x_3$ is the non-dimensionalised spanwise separation of the two points on the surface.

The cross-spectral density of the surface pressure can then be related to the far-field sound using the theory of Curle [77], according to which the acoustic response of an aerofoil can be obtained by considering a distribution of dipoles on the surface with the same strength of the force acting on the surface itself. If the far-field pressure produced by an elementary force $F(x_{1,0}, x_{3,0}, \omega)\,\mathrm{e}^{i\omega t}\boldsymbol{k}$ acting on the point $\boldsymbol{x}_0 = (x_{1,0}, 0, x_{3,0})$ is indicated with $p_1(x_1, x_2, x_3, \omega, x_{1,0}, x_{3,0})$, this can be expressed as

$$p_1(x_1, x_2, x_3, \omega, x_{1,0}, x_{3,0}) = \frac{\mathrm{i}\omega x_3 F(x_{1,0}, x_{3,0}, \omega)}{4\pi \mathrm{c}_\infty \sigma_\infty^2} \mathrm{e}^{i\omega\left[t + \frac{M_\infty(x_1 - x_{1,0}) - \sigma_\infty}{\mathrm{c}_\infty\beta^2} + \frac{x_1 x_{1,0} + x_3 x_{3,0}\beta^2}{\mathrm{c}_\infty\beta^2\sigma_\infty}\right]}, \quad (2.8)$$

where M_∞ is the free-stream Mach number, and c_∞ is the speed of sound. The effects of convection are accounted for in the variable σ_∞, whose expression is

$$\sigma_\infty = \sqrt{(x_1 - x_{1,0})^2 + \beta^2\left[(x_2 - x_{2,0})^2 + (x_3 - x_{3,0})^2\right]}, \quad (2.9)$$

with $\beta = \sqrt{1 - M_\infty^2}$ being the compressibility factor.

By integrating the cross-spectral density of the pressure jump on the whole surface, the loading acting on the aerofoil can be related to the far-field acoustic pressure S_{pp} in $\boldsymbol{x}$ through

$$S_{pp}(\boldsymbol{x}, \omega) = \left(\frac{\omega x_3}{4\pi c_\infty \sigma_\infty^2}\right)^2 \iiiint S_{QQ}(x_1, x_1', \eta, \omega) \times \mathrm{e}^{\frac{\mathrm{i}\omega}{c_\infty}\left[\beta^{-2}(x_1 - x_1')\left(M_\infty - \frac{x_1}{\sigma_\infty}\right) + \frac{x_2\eta}{\sigma_\infty}\right]} \mathrm{d}x_1\,\mathrm{d}x_1'\,\mathrm{d}x_2\,\mathrm{d}x_2'. \quad (2.10)$$

By substituting Eq. (2.7) in Eq. (2.10), the far-field acoustic pressure as a function of in-

coming turbulence spectrum can be expressed as

$$S_{pp}(\boldsymbol{x},\omega) = \left(\frac{\omega x_2 \rho_\infty \mathrm{c}}{2\mathrm{c}_\infty \sigma_\infty^2}\right)^2 \pi U_\infty \frac{\mathrm{L}}{2} \times \int_{-\infty}^{+\infty} \frac{\sin^2\left[\frac{\mathrm{L}}{2}\left(k_3 + \frac{\omega x_3}{\mathrm{c}_\infty \sigma_\infty}\right)\right]}{\left(k_3 + \frac{\omega x_3}{\mathrm{c}_\infty \sigma_\infty}\right)^2 \pi \frac{\mathrm{L}}{2}} |\mathscr{L}(\boldsymbol{x}, K_1, k_3)|^2 \Psi_{22}(K_1, k_3)\, \mathrm{d}k_3. \quad (2.11)$$

$\mathscr{L}$ is the total aeroacoustic transfer function, retrieved from the transfer function $g(x_1, K_1, k_3)$ through

$$\mathscr{L}(x_1, K_1, k_3) = \int_{-L/2}^{L/2} g\left(x_{1,0}, K_1, k_3\right) \mathrm{e}^{-\mathrm{i}\omega x_{1,0}(M_\infty - x_1/\sigma_\infty)/c_\infty \beta^2} \mathrm{d}x_{1,0}. \quad (2.12)$$

In the case of a flat plate, this function can be calculated analytically, while, for thicker aerofoils, numerical methodologies must be carried out [60]. The formulation employed in this thesis implements the derivation of Christophe [49], Rozenberg [78] and De Santana et al. [79], which derives the aeroacoustic transfer function as the sum of the leading-edge term $\mathscr{L}_1$ and trailing-edge term $\mathscr{L}_2$. These two contributions express the noise emitted by the scattering of the incoming turbulence at the leading edge and the back-scattering correction [57] of that incident field at the trailing edge, respectively. The expressions for $\mathscr{L}_1$ and $\mathscr{L}_2$ are reported in Eq. (2.45) and Eq. (2.46) in the dedicated Subsection 2.1.3.

A simplified formulation of Amiet's model has been implemented in the analyses carried out in Chapter 4 and Chapter 5. Indeed, Eq. (2.11) can be simplified by assuming a large span and considering a listener at the midspan plane of the aerofoil ($x_3 = 0$), where only gusts with $k_3 = 0$ contribute to the sound:

$$S_{pp}(x_1, x_2, 0, \omega) = \left(\frac{\omega x_2 \rho_\infty \mathrm{c} M_\infty}{2\sigma_\infty^2}\right)^2 \frac{\mathrm{L}}{2} |\mathscr{L}(\boldsymbol{x}, K_1, 0)|^2 \Theta_{22}(\omega)\, l_3(\omega). \quad (2.13)$$

This can be obtained as Amiet proves that, under these assumptions, $\Psi_{22}(K_1, 0)$ in Eq. (2.11) can be expressed as

$$\Psi_{22}(K_1, 0) = \frac{U_\infty}{\pi} \Theta_{22}(\omega)\, l_3(\omega), \quad (2.14)$$

where Θ_{22} is the PSD of the upwash velocity fluctuations, and l_3 is the spanwise coherence length of the velocity fluctuations impinging on the aerofoil. This is calculated considering the spanwise distribution of the upwash velocity component at the same positions where the frequency spectrum has been sampled using the following expression:

$$l_3(\omega) = \int_0^\infty \sqrt{\gamma^2_{u_2' u_2'}(\omega, x_3)}\, \mathrm{d}x_3. \quad (2.15)$$

Here, γ^2 is the magnitude square coherence defined as

$$\gamma^2_{s_1 s_2}(\omega) = \frac{|\Theta_{s_1 s_2}(\omega)|^2}{\Theta_{s_1 s_1}(\omega)\, \Theta_{s_2 s_2}(\omega)}, \quad (2.16)$$

s_1 being a reference time signal and s_2 a generic one, $\Theta_{s_1 s_1}$ and $\Theta_{s_2 s_2}$ the respective power spectral densities and $\Theta_{s_1 s_2}$ the cross-spectral density of the two variables.

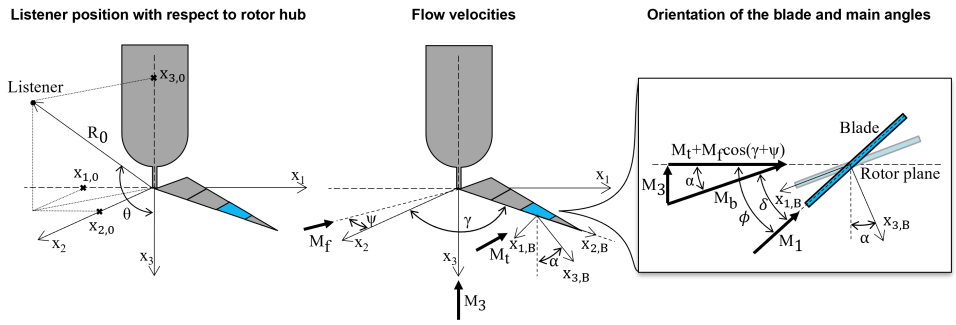

Figure 2.2: Rotor problem with key parameters and quantities.

2.1.2. LOW-FIDELITY PREDICTION FOR ROTATIONAL MOTION

A quick overview of Amiet's model for the low-fidelity prediction of turbulence-ingestion noise in the formulation accounting for B2B correlation is presented here. The reader is referred to Amiet [73, 80] for a more detailed formulation.

Figure 2.2 reports a sketch of the rotor problem, together with the most important quantities and parameters. The fixed reference frame $\mathbf{x}_0$ is centred on the rotor hub. The $x_1 - x_2$ plane lies in the rotor plane, while x_3 corresponds to the axial direction, along which the free-stream velocity $U_{3,\infty}$ is directed. The listener position is identified with the distance R_0 from the rotor hub and the elevation angle θ, taken with respect to the upstream direction of the x_3 axis. The azimuthal angle $\gamma = \Omega t$ measures the instantaneous angular distance of the blade from the x_1 axis.

For consistency with Amiet's notation, velocities are expressed in terms of Mach numbers. The axial Mach number is indicated with M_3, while, considering a blade element at a distance r from the rotor hub, the tangential (or azimuthal) Mach number $M_\mathrm{t} = \Omega r / c_\infty$ is obtained. With respect to the fixed reference frame, this is indicated in vectorial form as

$$\mathbf{M}_\mathrm{t} = \left(-M_\mathrm{t} \sin\gamma, M_\mathrm{t} \cos\gamma, 0\right). \tag{2.17}$$

In the most general configuration, the rotor is assumed to interact with a transverse velocity in its plane, characterised by a Mach number M_f. The angle between this velocity and the x_2-axis, fixed relative to the rotor, is denoted as ψ. Both M_f and ψ are equal to zero in the present investigation, but are kept in the formulation to preserve the generality of the discussion. Taking into account these velocities, the blade element at a distance r, simplified in Amiet's theory into a flat plate with no radial pitch distribution, interacts with a velocity u_b directed along the chord direction, with a Mach number indicated as M_b (see details of Fig. 1.4), which is calculated as

$$M_\mathrm{b} = \sqrt{M_3^2 + \left(M_\mathrm{t} + M_\mathrm{f} \cos\left(\gamma + \psi\right)\right)^2}. \tag{2.18}$$

This velocity forms an angle α with the rotor plane, obtained as

$$\alpha = \arctan\left(\frac{M_3}{M_\mathrm{t} + M_\mathrm{f} \cos\left(\gamma + \psi\right)}\right). \tag{2.19}$$

Following the approach of Sinayoko et al. [81], the present implementation of the model accounts for the radial pitch distribution $\phi(r)$. The velocity along the blade direction is thus given by $u_1 = u_b \cos\delta$ and the corresponding Mach number is denoted as M_1. Here, $\delta = \alpha - \phi$ represents the angle between u_b and the chord direction, as shown in the detail of Fig. 2.2.

The motion of the blade, and hence the relative position of the sound source with respect to the listener, must be accounted for to retrieve the noise prediction correctly. In the fixed reference frame, the listener position is identified by

$$\begin{cases} x_{1,0} = R_0 \sin\theta, \\ x_{2,0} = 0, \\ x_{3,0} = R_0 \cos\theta. \end{cases} \tag{2.20}$$

This position must be expressed in terms of the moving reference frame associated with the blade rotation, taking into account also the retarded source position of the aerofoil segment, i.e. the position where the source is when the acoustic wave reaches the listener. This is indicated with $\mathbf{x}_s$ and is expressed by

$$\begin{cases} x_{1,s} = -M_f r_e \sin\psi, \\ x_{2,s} = -M_f r_e \cos\psi, \\ x_{3,s} = -M_3 r_e, \end{cases} \tag{2.21}$$

with r_e being the distance of the listener from the retarded source derived as

$$r_e = R_0 \frac{M_s \cos\Lambda + \sqrt{1 - M_s^2 \sin^2\Lambda}}{1 - M_s^2}. \tag{2.22}$$

$M_s = \sqrt{M_f^2 + M_3^2}$ is the convection Mach number and Λ is the angle between $\mathbf{M}_s$ and $\mathbf{x}_0$, according to

$$\Lambda = \arccos\left(\frac{M_f \sin\psi \sin\theta + M_3 \cos\theta}{M_s}\right). \tag{2.23}$$

The "present" source position $\mathbf{x}_p$ must then be determined. This corresponds to the position of the source as if it had moved in the chordwise direction during the time taken by the acoustic wave to travel from its emission point identified by $\mathbf{x}_s$ to the listener. Amiet [80] shows that $\mathbf{x}_p$ reads

$$\begin{cases} x_{1,p} = r_e \left[-\left(M_t \sin\gamma + M_f \cos\gamma \sin\left(\gamma + \psi\right)\right)\right], \\ x_{2,p} = r_e \left[M_t \cos\gamma - M_f \sin\gamma \sin\left(\gamma + \psi\right)\right], \\ x_{3,p} = 0. \end{cases} \tag{2.24}$$

With respect to $\mathbf{x}_p$, the listener will be identified by $\mathbf{x}_0 - \mathbf{x}_p$. Accounting for the rotation around the x_3 axis to consider the azimuthal rotation $(\pi/2 - \gamma)$ with a rotation matrix R_3

$$\mathsf{R}_3 = \begin{bmatrix} \cos\left(\frac{\pi}{2} - \gamma\right) & -\sin\left(\frac{\pi}{2} - \gamma\right) & 0 \\ \sin\left(\frac{\pi}{2} - \gamma\right) & \cos\left(\frac{\pi}{2} - \gamma\right) & 0 \\ 0 & 0 & 1 \end{bmatrix}, \tag{2.25}$$

and for the angle α formed by the blade with respect to the rotor plane with a rotation matrix R_2

$$\mathsf{R}_2 = \begin{bmatrix} \cos\alpha & 0 & -\sin\alpha \\ 0 & 1 & 0 \\ \sin\alpha & 0 & \cos\alpha \end{bmatrix} \tag{2.26}$$

(as in the formulation of Sinayoko et al. [81]), the position of the listener $\mathbf{x}_\mathrm{B}$ in the blade reference frame (from which the subscript $_\mathrm{B}$) is finally obtained as

$$\mathbf{x}_\mathrm{B} = \mathsf{R}_2\mathsf{R}_3\left(\mathbf{x}_0 - \mathbf{x}_\mathrm{p}\right), \tag{2.27}$$

resulting in

$$\begin{cases} x_{1,\mathrm{B}} = \left[\left(x_{1,0} - x_{1,\mathrm{p}}\right)\sin\gamma - \left(x_{2,0} - x_{2,\mathrm{p}}\right)\cos\gamma\right]\cos\alpha - \left(x_{3,0} - x_{3,\mathrm{p}}\right)\sin\alpha; \\ x_{2,\mathrm{B}} = \left(x_{1,0} - x_{1,\mathrm{p}}\right)\cos\gamma + \left(x_{2,0} - x_{2,\mathrm{p}}\right)\sin\gamma; \\ x_{3,\mathrm{B}} = \left[\left(x_{1,0} - x_{1,\mathrm{p}}\right)\sin\gamma - \left(x_{2,0} - x_{2,\mathrm{p}}\right)\cos\gamma\right]\sin\alpha + \left(x_{3,0} - x_{3,\mathrm{p}}\right)\cos\alpha. \end{cases} \tag{2.28}$$

Once the motion of the sound source is taken into account, Amiet [73] treats the sound produced by each rotating blade at a certain azimuthal position as if it was generated in rectilinear motion, enabling the application of the analytical model [16] to the rotating regime. This procedure relies on a fundamental assumption: the frequency range of the noise is much higher than the rotational speed of the rotor.

The far-field acoustic pressure $S_{pp}\left(\mathbf{x}_\mathrm{B}, \omega_0\right)$ at the listener position $\mathbf{x}_\mathrm{B} = \left(x_{1,\mathrm{B}}, x_{2,\mathrm{B}}, x_{3,\mathrm{B}}\right)$, with $\omega_0 = 2\pi f$ being the sound frequency as heard by the observer in the fixed reference frame, is hence retrieved through the azimuthal average of the instantaneous noise emission $S'_{pp}\left(\mathbf{x}_\mathrm{B}, \omega_0, \gamma\right)$ through

$$S_{pp}\left(\mathbf{x}_\mathrm{B}, \omega_0\right) = \frac{1}{2\pi}\int_0^{2\pi}\left(\frac{\omega_\mathrm{B}}{\omega_0}\right)S'_{pp}\left(\mathbf{x}_\mathrm{B}, \omega_0, \gamma\right)\mathrm{d}\gamma. \tag{2.29}$$

$\omega_\mathrm{B}/\omega_0$ describes the Doppler's effect due to the sound source motion with respect to the listener position. This is calculated as

$$\frac{\omega_0}{\omega_\mathrm{B}} = 1 + \frac{\mathbf{M}_t \cdot \hat{\mathbf{s}}}{1 - \mathbf{M}_r \cdot \hat{\mathbf{s}}},$$

with $\mathbf{M}_\mathrm{r}$ representing the Mach number of the source with respect to the fluid, expressed in vectorial form as

$$\mathbf{M}_\mathrm{r} = \left(M_\mathrm{f}\sin\psi - M_\mathrm{t}\sin\gamma, M_\mathrm{f}\cos\psi + M_\mathrm{t}\cos\gamma, M_3\right), \tag{2.30}$$

$\hat{\mathbf{s}}$ being the unit vector from the retarded source position to the listener according to

$$\hat{\mathbf{s}} = \left(\frac{x_{1,s} - x_{1,0}}{r_e}, \frac{x_{2,s} - x_{2,0}}{r_e}, \frac{x_{3,s} - x_{3,0}}{r_e}\right). \tag{2.31}$$

$S'_{pp}\left(\mathbf{x}_\mathrm{B}, \omega_0, \gamma\right)$, expressed in terms of the Doppler shifted frequency as heard by the listener ω_0, is related to $S_{pp}\left(\mathbf{x}_\mathrm{B}, \omega_\mathrm{B}, \gamma\right)$, depending on the angular frequency of the blade forces ω_B through

$$S'_{pp}\left(\mathbf{x}_\mathrm{B}, \omega_0, \gamma\right) = \frac{\omega_\mathrm{B}}{\omega_0}S_{pp}\left(\mathbf{x}_\mathrm{B}, \omega_\mathrm{B}, \gamma\right), \tag{2.32}$$

meaning that a factor $(\omega_B/\omega_0)^2$ will appear in Eq. (2.29).

In the formulation accounting for the correlation of the unsteady surface pressure induced by the chopping of an eddie by more than one blade, $S_{pp}\left(\mathbf{x}_B,\omega_B,\gamma\right)$ takes the form

$$S_{pp}\left(\mathbf{x}_B,\omega_B,\gamma\right) = G\left|\mathscr{L}\left(K_1,K_2,M_1\right)\right|^2 \sum_{n=-\infty}^{\infty} \Phi_{33}\left(K_1,K_2,K_3^{(n)}\right) \frac{2\pi}{\left(\frac{c}{2}\right)^2 \overline{u_3'^2} X_3}, \tag{2.33}$$

with

$$G = \left(\frac{\omega_B x_{3,B} \rho_\infty c}{2 c_\infty \sigma_\infty^2}\right)^2 \pi U_1 \left(\frac{L}{2}\right) \overline{u_3'^2} \left(\frac{c}{2}\right)^2. \tag{2.34}$$

The blade geometry is represented by the chord c and the span L, while the convection factor σ_∞ is calculated in this case as $\sigma_\infty = \sqrt{x_{1,B}^2 + \beta_1^2\left(x_{2,B}^2 + x_{3,B}^2\right)}$, with $\beta_1 = \sqrt{1-M_1^2}$. $\mathscr{L}\left(K_1,K_2,M_1\right)$ is the aeroacoustic transfer function, for which the original formulation of Amiet [80] has been used, while $\Phi_{33}\left(K_1,K_2,K_3^{(n)}\right)$ is the three-dimensional turbulence spectrum. The wavenumbers are calculated as

$$\begin{cases} K_1 = \dfrac{\omega_B}{u_1}, \\ K_2 = \dfrac{\omega_B x_{2,B}}{c_\infty \sigma_\infty}, \\ K_3^{(n)} = \dfrac{2\pi n + \omega_0 T_2}{X_3}. \end{cases} \tag{2.35}$$

K_1 takes this form under the hypothesis of frozen turbulence, while K_2 under the large-span wing assumption, i.e. $M_\infty K_1 L/2 \gg 0$, and $K_3^{(n)}$ is obtained in the framework of the B2B correlation. The latter term features the Doppler-shifted frequency ω_0, the time between consecutive chops of a certain eddy as heard by the listener T_2, and the distance X_3, which represents the distance between the path of two adjacent blades measured with respect to the fluid, nX_3 thus being the distance between the 0-th and the n-th blade paths. T_2 is calculated by adding a $\Delta\tau$ to the time between eddie chops T_1 through

$$T_2 = T_1 + \Delta\tau. \tag{2.36}$$

The expression for T_1 reads

$$T_1 = T_t \left(\frac{u_t}{u_3}\right) \sin\alpha \cos\alpha, \tag{2.37}$$

where $T_t = 2\pi/\Omega B$, while $\Delta\tau$ is calculated as

$$\Delta\tau = X_1 \left(\frac{M_1 - \frac{x_{1,B}}{\sigma_\infty}}{\beta_1^2 c_\infty}\right) + X_2 \frac{x_{2,B}}{c_\infty \sigma_\infty}, \tag{2.38}$$

with $X_1 = (T_t - T_1)$, u_t, $X_2 = T_1\, u_f \sin\left(\gamma+\psi\right)$, and $X_3 = T_t\, u_t \sin\alpha$. The reader is referred to Amiet [73, 80] for the physical meaning of these parameters and the derivation of the respective expressions, whose explanation is beyond the scope of this study.

2.1.3. AEROACOUSTIC TRANSFER FUNCTION

The aeroacoustic transfer function $\mathscr{L}$ is implemented following Christophe [49], Rozenberg [78] and De Santana et al. [79], where it is obtained as the sum of the two contributions $\mathscr{L}_1$ and $\mathscr{L}_2$. The two terms are retrieved by calculating the pressure distribution induced by the sinusoidal perturbation, whose expressions are

$$p_1(x_1,0,x_3,t) = \rho_\infty U_\infty u_{2,0} \frac{\mathrm{e}^{-\mathrm{i}\pi/4}\left(\frac{k_1 c}{2\beta^2}-\chi\right)}{\sqrt{\pi\left(\frac{k_1 c}{2\beta^2}-\chi\right)\left[\left(\frac{k_1 c}{2}\right)^2+\left(\frac{k_3 c}{2}\right)^2\right]\frac{2x_1}{c}}} \mathrm{e}^{\mathrm{i}\left(\omega t-\left[2\left(\frac{k_1 c}{2\beta^2}-\chi\right)/c-k_1\right]x_1-k_3 x_3\right)} \tag{2.39}$$

for the leading-edge term and

$$\begin{aligned} p_2(x_1,0,x_3,t) \simeq -\rho_\infty U_\infty u_{2,0} &\frac{1}{\sqrt{2\pi\left[\left(\frac{k_1 c}{2}\right)^2+\beta^2\chi\right]}} \\ &\times\left[1-(1+\mathrm{i})\,\mathrm{E}^*\left(2\chi\left(2-\frac{2x_1}{c}\right)\right)\right]\mathrm{e}^{\mathrm{i}\left[\left(\frac{k_1 c}{2\beta^2}M_\infty^2\right)\frac{2x_1}{c}-\pi/4+\omega t-k_3 x_3\right]} \end{aligned} \tag{2.40}$$

the trailing-edge one, with $\chi^2=\mu^2-k_3^2 c/\left(2\beta^2\right)$, and $\mu=k_1 c M_\infty/\left(2\beta^2\right)$, whereas the function $E^*(z)$ (with z indicating a generic variable) is expressed as

$$E^*(z) = \int_0^z \frac{\mathrm{e}^{-\mathrm{i}z'}}{\sqrt{2\pi z'}}\mathrm{d}z' = C_2(z)-\mathrm{i}S_2(z), \tag{2.41}$$

C_2 and S_2 being the two Fresnel's integrals:

$$C_2(z) = \frac{1}{\sqrt{2\pi}}\int_0^z \frac{\cos\left(z'\right)}{\sqrt{z'}}\mathrm{d}z' \tag{2.42}$$

and

$$S_2(z) = \frac{1}{\sqrt{2\pi}}\int_0^z \frac{\sin\left(z'\right)}{\sqrt{z'}}\mathrm{d}z'. \tag{2.43}$$

These expressions, valid in the case of supercritical gust ($\chi^2>0$), are then substituted into $g(x_1,k_1,k_3)$, which is retrieved by rearranging Eq. 2.3 as

$$g(x_1,k_1,k_3) = \frac{\Delta p(x_1,x_3,t)\,\mathrm{e}^{\mathrm{i}(k_1 U_\infty t-k_3 x_3)}}{\pi\rho_\infty U_\infty \mathrm{c} u_{2,0}}. \tag{2.44}$$

$\mathscr{L}_1$ and $\mathscr{L}_2$ are then obtained by substituting the resulting expressions into Eq. 2.12, yielding

$$\mathscr{L}_1(\boldsymbol{x},k_1,k_3) = \frac{1}{\pi}\sqrt{\frac{2}{\left(\frac{k_1 c}{2}+\beta^2\chi\right)\nu_1}}E^*(2\nu_1)\,\mathrm{e}^{\mathrm{i}\nu_2}; \tag{2.45}$$

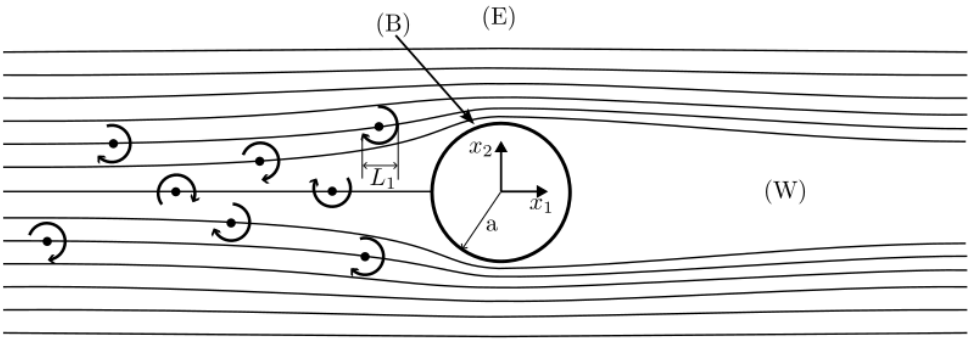

Figure 2.3: Scheme of a bluff body immersed in a turbulent flow with the characteristic length a and the scale of the incident turbulence L_1 highlighted. The different regions characterising the flow field that surround the bluff body are indicated together with the spatial reference systems considered in the present investigation.

$$\mathscr{L}_2(\boldsymbol{x}, k_1, k_3) \simeq \frac{\mathrm{e}^{\mathrm{i}\nu_2}}{\pi\nu_1\sqrt{2\pi\left(\frac{k_1 c}{2}+\beta^2\chi\right)}}\left\{\mathrm{i}\left(1-\mathrm{e}^{-2\mathrm{i}\nu_1}\right)\right.$$
$$\left.+(1-\mathrm{i})\left[E^*(4\chi)-\sqrt{\frac{2\chi}{\nu_3}}\mathrm{e}^{-2\mathrm{i}\nu_1}E^*(2\nu_3)\right]\right\}. \quad (2.46)$$

In this expression, $\nu_1 = \chi - \mu x_1/\sigma_\infty$, $\nu_2 = \mu(M_\infty - x_1/\sigma_\infty) - \pi/4$, and $\nu_3 = \chi + \mu x_1/\sigma_\infty$.

2.2. RAPID DISTORTION THEORY

The basic assumptions and governing equations of the RDT are briefly reported to provide the reader with the theoretical framework behind the results presented in this work. The mathematical formulation of the theory is based on the work of Hunt [45] in the implementation of Zamponi et al. [82]. In the discussion below, the reference system and relative velocity components are consistent with those presented in Subsection 2.1.1.

2.2.1. ASSUMPTIONS OF THE THEORY

The typical problem addressed by the RDT is depicted in Fig. 2.3. The flow field interacting with a bluff body is divided into different sub-regions: an outer region (E) where the normal and shear stresses are negligible with respect to the inertial forces, a thin region (B) coincident with the boundary layer on the surface $\mathbb{S}$, and a region of flow separation (W) in the wake of the body characterised by large velocity fluctuations.

The following assumptions are at the base of the theory:

- the intensity of the incoming turbulence is weak

$$\frac{u'_\infty}{U_\infty} \ll 1; \quad (2.47)$$

- the Reynolds number calculated with respect to the intensity and the integral length scale L_1 of the upstream turbulence is large

$$\frac{\rho u'_\infty L_1}{\mu} \gg 1, \tag{2.48}$$

with μ being the dynamic viscosity of the fluid;

- the time taken by the flow to be distorted is much smaller than the time scale of turbulence, expressed by Hunt [45] as

$$\frac{u'_\infty}{U_\infty} \ll \frac{L_1}{a}. \tag{2.49}$$

In this scenario, the flow in the region (E) is not significantly affected by the velocity fluctuations in regions (B) and (W) and can be modelled by the solution of a well-posed boundary value problem determining the changes in a given fluctuating-velocity field [45].

2.2.2. GOVERNING EQUATIONS AND FOURIER ANALYSIS

In the assumption of incompressible flow, the governing equations are

$$\frac{\partial u'_i}{\partial t} + \overline{u}_j \frac{\partial u'_i}{\partial x_j} + u'_j \frac{\partial \overline{u}_i}{\partial x_j} = -\frac{1}{\rho}\frac{\partial p}{\partial x_i}, \tag{2.50}$$

$$\frac{\partial \overline{u}_i}{\partial x_i} = 0 \quad \text{and} \quad \frac{\partial u'_i}{\partial x_i} = 0, \tag{2.51}$$

with p being the pressure and ν the kinematic viscosity. The dependence on the pressure can be removed by taking the curl of the linearised momentum equation 2.50, leading to the following dimensionless linearised vorticity equation

$$\frac{\partial \omega_i^*}{\partial t^*} + U_j^* \frac{\partial \omega_i^*}{\partial x_j^*} + u_j'^* \frac{\partial \Omega_i^*}{\partial x_j^*} = \omega_j^* \frac{\partial U_i^*}{\partial x_j^*} + \Omega_j^* \frac{\partial u_i'^*}{\partial x_j^*}, \tag{2.52}$$

where $\boldsymbol{U}^* = \overline{\boldsymbol{u}}/U_\infty$, $\boldsymbol{u}'^* = \boldsymbol{u}'/u'_\infty$, and the non-dimensional coordinates obtained as

$$\left(x_1^*, x_2^*, x_3^*, t^*\right) = (x_1, x_2, x_3, tU_\infty)/a. \tag{2.53}$$

The corresponding vorticity terms $\boldsymbol{\Omega}^*$ and $\boldsymbol{\omega}^*$ are expressed as $\boldsymbol{\Omega}^* = \nabla \times \boldsymbol{U}^*$ and $\boldsymbol{\omega}^* = \nabla \times \boldsymbol{u}'^*$.

In the case of bluff-body flows, such as that around a circular cylinder, the most relevant effect on turbulence is due to the irrotational component of $\boldsymbol{U}^*$, meaning that it is possible to assume that

$$\boldsymbol{\Omega}^* = 0 \tag{2.54}$$

in Eq. (2.52), as demonstrated by Hunt [45] in his original work through an order-of-magnitude analysis. Consequently, the mean-velocity field can be obtained as the solution to a potential flow problem satisfying appropriate boundary conditions. Considering that the upstream velocity U_∞ is set, only one condition needs to be imposed. Taking

into account that the normal component of the incident velocity must be zero at the wall in the case of a solid body, it is possible to write

$$\boldsymbol{u}'^{*} \cdot \boldsymbol{n} = 0 \qquad \text{on} \quad \mathbb{S}, \tag{2.55}$$

where $\boldsymbol{n}$ is the outward-pointing normal to the body surface $\mathbb{S}$.

At this point, Cauchy's equation allows $\boldsymbol{\omega}^*$ to be expressed as a function of its upstream value $\boldsymbol{\omega}^*_\infty$ [47] and the vorticity distortion tensor $\boldsymbol{\gamma}$, hence obtaining

$$\omega_i^*\left(x_1^*, x_2^*, x_3^*, t^*\right) = \gamma_{ij}\left(x_1^*, x_2^*\right) \omega^*_{\infty,j}\left(x_1^*, x_2^* - \Delta_2, x_3^*, t^* - \Delta_T\right). \tag{2.56}$$

Δ_2 expresses the deviation of a fluid particle in the x_2^*-direction as it is convected around the body. It is defined as $\Delta_2 = x_2^* + \Psi$, with Ψ being the streamfunction of the irrotational mean flow. Δ_T is instead the drift function [83], whose expression is

$$\Delta_T = \int_{-\infty}^{x_1^*} \left(\frac{1}{U_1^*(x_1^{*\prime}, x_2^{*\prime})} - 1 \right) dx_1^{*\prime} \quad \text{where} \quad \Psi(x_1^{*\prime}, x_2^{*\prime}) = \Psi(x_1^*, x_2^*). \tag{2.57}$$

In this case, $\boldsymbol{\gamma}$ can be expressed as a function of $\boldsymbol{U}^*$ and the derivatives of Δ_T along x_1^* and x_2^* [45], i.e.

$$\gamma_{ij} = \begin{bmatrix} U_1^* & -\partial\Delta_T/\partial x_2^* & 0 \\ U_2^* & 1 + \partial\Delta_T/\partial x_1^* & 0 \\ 0 & 0 & 1 \end{bmatrix}. \tag{2.58}$$

The knowledge of $\boldsymbol{U}^*$ and $\boldsymbol{\omega}^*$ allows $\boldsymbol{u}'^*$ to be calculated as its deviation from the upstream value, as a function of a scalar velocity potential ϕ and a vortical streamfunction $\boldsymbol{\psi}$, characterised by the gauge condition $\nabla \cdot \boldsymbol{\psi} = 0$ [84]. The following expression is thus obtained:

$$\Delta\boldsymbol{u}'^* = \boldsymbol{u}'^* - \boldsymbol{u}'^*_\infty = -\nabla\phi + \nabla \times \boldsymbol{\psi}. \tag{2.59}$$

This can be, in turn, substituted into the continuity equation and the vorticity one Eq. (2.52) to retrieve a new set of governing equations:

$$\nabla^2\phi = 0 \tag{2.60}$$

$$\nabla^2\boldsymbol{\psi} = -\Delta\boldsymbol{\omega}^* = -(\boldsymbol{\omega}^* - \boldsymbol{\omega}^*_\infty). \tag{2.61}$$

As regards to the boundary conditions, Eq. (2.55) implies for Eq. (2.60) that

$$\nabla\phi \cdot \boldsymbol{n} = \boldsymbol{u}'^*_\infty \cdot \boldsymbol{n} \qquad \text{on} \quad \mathbb{S}, \tag{2.62}$$

whereas the imposition of the upstream velocity results in

$$|\nabla\phi| \to 0 \qquad \text{as} \quad x_1^{*2} + x_2^{*2} \to \infty. \tag{2.63}$$

For Eq. (2.61), the same conditions lead to

$$(\nabla \times \boldsymbol{\psi}) \cdot \boldsymbol{n} = 0 \qquad \text{on} \quad \mathbb{S} \tag{2.64}$$

and

$$|\nabla \times \boldsymbol{\psi}| \to 0 \qquad \text{as} \quad x_1^{*2} + x_2^{*2} \to \infty, \tag{2.65}$$

respectively. Moreover, in order to satisfy the gauge condition at every point of the flow field, it is necessary to impose an additional boundary condition on $\boldsymbol{\psi}$:

$$\nabla \cdot \boldsymbol{\psi} = 0 \qquad \text{on} \quad \mathbb{S} \qquad \text{and} \quad \text{as} \quad x_1^{*2} + x_2^{*2} \to \infty. \tag{2.66}$$

The new set of governing equations, i.e. the Laplace equation for ϕ in Eq. (2.60) and the three Poisson equations for $\boldsymbol{\psi}$ in Eq. (2.61), entails four partial differential equations, which must be solved simultaneously. It should be noted that Goldstein [71] formulated an alternative and less cumbersome approach to solving the RDT equations compared with the method presented in this section.

Hunt's formulation proceeds by assuming the upstream turbulence to be homogeneous and stationary in time. Under these conditions, it is possible to describe the velocity field by means of spatial Fourier analysis in terms of the velocity distortion tensor $\mathbf{M}$:

$$\hat{u}_i'^* = \int_{-\infty}^{\infty} \mathsf{M}_{ij}(x_1^*, x_2^*; \boldsymbol{\kappa})\, \hat{u}_{\infty,j}'^*(\boldsymbol{\kappa})\, d\kappa_2, \tag{2.67}$$

with $\boldsymbol{\kappa}$ being the non-dimensional wavenumber calculated as

$$\boldsymbol{\kappa} = \begin{pmatrix} \kappa_1 \\ \kappa_2 \\ \kappa_3 \end{pmatrix} = a \begin{pmatrix} k_1 \\ k_2 \\ k_3 \end{pmatrix}.$$

$\hat{\hat{\boldsymbol{u}}}_\infty'^*$ is the spatial Fourier transform of the upstream velocity obtained from

$$\begin{pmatrix} u_{\infty,i}'^* \\ \omega_{\infty,i}^* \end{pmatrix}(x_1^*, x_2^*, x_3^*, t^*) = \iiint_{-\infty}^{\infty} \mathrm{e}^{i(\kappa_1 x_1^* + \kappa_2 x_2^* + \kappa_3 x_3^* + \sigma t'^*)} \times \begin{pmatrix} \hat{u}_{\infty,i}^* \\ \hat{\omega}_{\infty,i}^* \end{pmatrix}(\boldsymbol{\kappa})\, d\kappa_1\, d\kappa_2\, d\kappa_3, \tag{2.68}$$

where $\sigma = -\kappa_1$ for Taylor's hypothesis. As turbulent structures approach the body, the flow becomes inhomogeneous in the x_1^* and x_2^* directions, while remaining homogeneous along x_3^*, as the mean velocity does not vary in that direction. Consequently, the Fourier analysis of ϕ and $\boldsymbol{\psi}$ leads to

$$\begin{pmatrix} \phi \\ \psi_i \end{pmatrix}(x_1^*, x_2^*, x_3^*, t^*) = \iint_{-\infty}^{\infty} \mathrm{e}^{i(\kappa_3 x_3^* - \kappa_1 t^*)} \begin{pmatrix} \hat{\hat{\phi}} \\ \hat{\hat{\psi}}_i \end{pmatrix}(x_1^*, x_2^*; \kappa_1, \kappa_3)\, d\kappa_1\, d\kappa_3, \tag{2.69}$$

obtained using the decomposition of the velocity field in Eq. (2.59). Equation (2.60) can hence be rewritten as

$$\left\{ \frac{\partial^2}{\mathrm{d}x_1^{*2}} + \frac{\partial^2}{\mathrm{d}x_2^{*2}} - \kappa_3^2 \right\} \hat{\hat{\phi}} = 0, \tag{2.70}$$

while Eq. (2.61)) becomes

$$\left\{ \frac{\partial^2}{\mathrm{d}x_1^{*2}} + \frac{\partial^2}{\mathrm{d}x_2^{*2}} - \kappa_3^2 \right\} \hat{\hat{\psi}}_i = -\left[\hat{\hat{\omega}}_i - \int_{-\infty}^{\infty} \mathrm{e}^{i(\kappa_1 x_1^* + \kappa_2 x_2^*)}\, \hat{\omega}_{\infty,i}^*\, d\kappa_2 \right]. \tag{2.71}$$

It must be noted that $\partial/\partial x_3^* = i\kappa_3$ due to the homogeneity in the x_3^* direction. From Eq. (2.56), it follows that

$$\hat{\omega}_i^* = \gamma_{ij}(x_1^*, x_2^*)\, \mathrm{e}^{i\kappa_1(\Delta_T + x_1^*)} \int_{-\infty}^{\infty} \mathrm{e}^{i\kappa_2(x_2^* - \Delta_2)}\, \hat{\omega}_{\infty,j}^*\, d\kappa_2. \tag{2.72}$$

The governing equations can be simplified by introducing the following two variables

$$\hat{\tilde{\phi}}(x_1^*, x_2^*; \kappa_1, \kappa_3) = \int_{-\infty}^{\infty} \beta_j(x_1^*, x_2^*; \boldsymbol{\kappa})\, \hat{u}'^*_{\infty,j}(\boldsymbol{\kappa})\, d\kappa_2; \tag{2.73}$$

$$\hat{\tilde{\psi}}_i(x_1^*, x_2^*; \kappa_1, \kappa_3) = \int_{-\infty}^{\infty} \alpha_{ij}(x_1, x_2; \boldsymbol{\kappa})\, \hat{\omega}_{\infty,j}^*(\boldsymbol{\kappa})\, d\kappa_2. \tag{2.74}$$

$\boldsymbol{\alpha}$ is a tensor and represents the turbulent streamfunction, while $\boldsymbol{\beta}$ is a vector and indicates the turbulent-velocity potential. The substitution of Eq. (2.73) into Eq. (2.70) leads to

$$\left\{ \frac{\partial^2}{\mathrm{d}x_1^{*2}} + \frac{\partial^2}{\mathrm{d}x_2^{*2}} - \kappa_3^2 \right\} \beta_j = 0, \tag{2.75}$$

while substituting Eq. (2.74) and Eq. (2.72) into Eq. (2.71) retrieves

$$\left\{ \frac{\partial^2}{\mathrm{d}x_1^{*2}} + \frac{\partial^2}{\mathrm{d}x_2^{*2}} - \kappa_3^2 \right\} \alpha_{ij} = -\Omega_{ij}^\star \qquad \text{with} \qquad \Omega_{ij}^\star = \left[\gamma_{ij}\, \mathrm{e}^{i(\kappa_1 \Delta_T - \kappa_2 \Delta_2)} - \delta_{ij} \right] \mathrm{e}^{i(\kappa_1 x_1^* + \kappa_2 x_2^*)}, \tag{2.76}$$

with $\boldsymbol{\delta}$ indicating the Kronecker delta. The function $\boldsymbol{\Omega}^\star$ is known. It tends to zero as $x_1^* \to -\infty$ or $x_2^* \to \pm\infty$ as a consequence of $\Delta_T, \Delta_2 \to 0$ and $\boldsymbol{\gamma} \to \boldsymbol{\delta}$. The boundary conditions must then be expressed in terms of $\boldsymbol{\alpha}$ and $\boldsymbol{\beta}$ to pose the problem in a formal manner.

Using Eq. (2.73) and Eq. (2.74), and keeping into account that

$$\hat{\boldsymbol{u}}'^* = -\nabla \hat{\tilde{\phi}} + \nabla \times \hat{\tilde{\boldsymbol{\psi}}} + \hat{\boldsymbol{u}}'^*_{\infty},$$

it is possible to write

$$\hat{u}_i'^* = \int_{-\infty}^{\infty} \left\{ \left(\mathsf{M}_{ij}^{(\mathrm{s})} + \mathsf{M}_{ij}^{(\infty)} \right) \hat{u}'^*_{\infty,j} + \mathsf{a}_{ij}\, \hat{\omega}^*_{\infty,j} \right\} d\kappa_2, \tag{2.77}$$

with

$$\begin{aligned} \mathsf{M}_{ij}^{(\mathrm{s})} &= -\left(\frac{\partial \beta_j}{\partial x_1^*}, \frac{\partial \beta_j}{\partial x_2^*}, i\kappa_3 \beta_j \right); \quad \mathsf{M}_{ij}^{(\infty)} = \delta_{ij} \mathrm{e}^{i(\kappa_1 x_1^* + \kappa_2 x_2^*)}; \\ \mathsf{a}_{ij} &= \left(\frac{\partial \alpha_{3j}}{\partial x_2^*} - i\kappa_3 \alpha_{2j}, i\kappa_3 \alpha_{1j} - \frac{\partial \alpha_{3j}}{\partial x_1^*}, \frac{\partial \alpha_{2j}}{\partial x_1^*} - \frac{\partial \alpha_{1j}}{\partial x_2^*} \right). \end{aligned} \tag{2.78}$$

Keeping into account that, from the definition of vorticity,

$$\hat{\omega}^*_{\infty,i} = \varepsilon_{ijk} \left(\partial \hat{u}^*_{\infty,k} / \partial x_j^* \right) = \varepsilon_{ijk} \left(i\kappa_j \hat{u}^*_{\infty,k} \right),$$

with ε_{ijk} being the Levi-Civita symbol, it is possible to write

$$\mathsf{M}_{il}^{(\mathrm{d})} = i\mathsf{a}_{ij} \varepsilon_{kjl} \kappa_k, \tag{2.79}$$

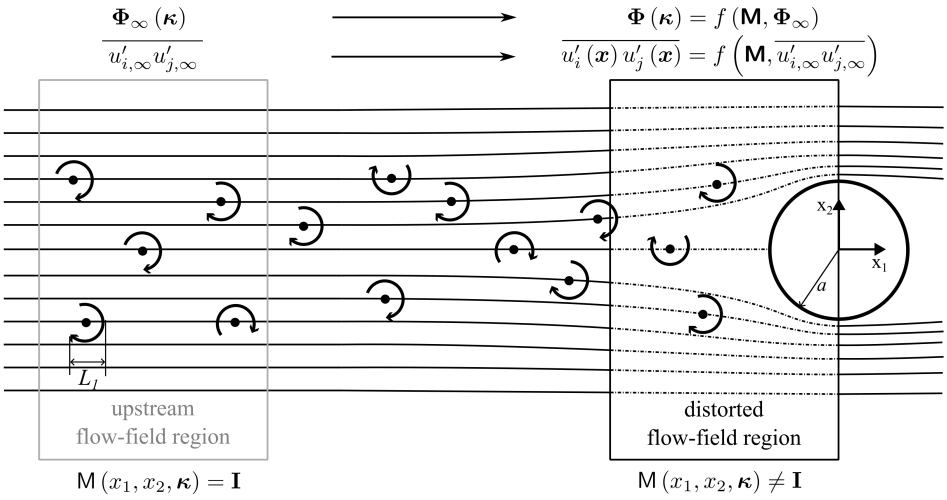

Figure 2.4: Conceptual sketch of the RDT framework. Velocity spectra and variances are expressed as a function of the velocity tensor $\mathbf{M}(x_1, x_2, \boldsymbol{\kappa})$, related to the alteration of the flow field caused by the presence of the bluff body, and the upstream values. This holds both in the distorted and the upstream regions of the flow field, where the velocity field is not altered and the velocity tensor thus tends to the identity matrix.

finally leading to an expression for the velocity tensor M in Eq. (2.67) as the sum of three different terms

$$\mathbf{M} = \mathbf{M}^{(\mathrm{s})} + \mathbf{M}^{(\mathrm{d})} + \mathbf{M}^{(\infty)}. \tag{2.80}$$

These terms account for the various contributions to the distortion of the turbulent structures. $\mathbf{M}^{(\mathrm{s})}$ is related to the distortion caused by the blockage due to the presence of the body, $\mathbf{M}^{(\mathrm{d})}$ describes the distortion induced by the distortion of the vorticity field, and $\mathbf{M}^{(\infty)}$ represents the alteration undergone by turbulence because of the upstream conditions.

2.2.3. SPECTRA AND VARIANCES UNDER ASYMPTOTIC ANALYSES

The RDT calculates the alteration of the velocity cross-spectra, auto-spectra, and coherence from the upstream undistorted flow conditions using the velocity tensor $\mathbf{M}$ to model the distortion of the flow field. A conceptual sketch is reported in Fig. 2.4. In the case of the distorted one-dimensional spectra of the velocity components u_i and u_j $\Theta^*_{ij,\mathrm{dis}}$, generically calculated between the non-dimensional positions $\left(x_1^*, x_2^*\right) = (x_1, x_2)/a$ and $\left(x_1'^*, x_2'^*\right) = \left(x_1', x_2'\right)/a$ separated by a lateral distance $r_3^* = r_3/a$, the following expression can be obtained as a function of the three-dimensional spectrum $\boldsymbol{\Phi}^*_{\mathrm{ups}}$ of the up-

stream turbulence:

$$\Theta^*_{ij}\left(x^*_1, x^*_2; x'^*_1, x'^*_2; r^*_3; \kappa_1\right) = \iint_{-\infty}^{\infty} \mathsf{M}_{il}\left(x^*_1, x^*_2, \boldsymbol{\kappa}\right)^{\dagger} \mathsf{M}_{jm}\left(x'^*_1, x'^*_2, \boldsymbol{\kappa}\right) \Phi^*_{lm,\infty}(\boldsymbol{\kappa})\, \mathrm{e}^{\mathrm{i}\kappa_3 r^*_3}\, \mathrm{d}\kappa_2 \mathrm{d}\kappa_3, \quad (2.81)$$

with the superscript † indicating the complex conjugate. The non-dimensional spectrum $\Theta^*_{ij}(\kappa_i)$ is related to the dimensional one through

$$\Theta^*_{ij}(\kappa_i) = \frac{L_1}{a} \frac{\Theta_{ij}(k_i)}{u'^2_i L_1}. \quad (2.82)$$

The upstream undistorted turbulence spectrum $\boldsymbol{\Phi}^*_{\infty}$ can be modelled using the von Kármán turbulence spectrum [47]

$$\Phi^*_{ij,\infty}(\boldsymbol{\kappa}) = \frac{55 g_1 (a/L_1)^{2/3} k^2}{36\pi \left[g_2 (a/L_1)^2 + k^2\right]^{\frac{17}{6}}} \left[\delta_{ij} - \frac{\kappa_i \kappa_j}{k^2}\right], \quad (2.83)$$

where $k^2 = \kappa_1^2 + \kappa_2^2 + \kappa_3^2 = |\boldsymbol{\kappa}|^2$, $g_2 = \pi \Gamma^2(5/6)/\Gamma^2(1/3) = 0.5578$, and $g_1 = g_2^{5/6}/\pi = 0.1957$, with $\Gamma(\cdot)$ being the Gamma function.

The alteration of the velocity field can then be estimated using the canonical turbulence spectrum modelling undistorted turbulence conditions once the velocity tensor has been calculated in the vicinity of the body for each wavenumber component solving four partial differential equations (see Hunt [45] and Zamponi et al. [82]). However, in the asymptotic cases of very large-scale and small-scale turbulence structures interacting with the body, Hunt [45] showed that Eq. (2.81) can be simplified into closed-form expressions. A summarised version of the discussion carried out for these limit scenarios is reported hereafter, as these form the foundation of the methodology developed in Chapter 5. The reader may refer to Sections 5 and 6 in Hunt [45] for the complete analytical formulation.

LARGE-SCALE TURBULENCE

One-dimensional spectra For large-scale turbulence ($L_1/a \gg 1$), Hunt [45] proved that the spectra can be calculated using the asymptotic expansion of M_{il} valid for $k \to 0$:

$$\mathsf{M}_{il} = \mathsf{M}^{(0)}_{il} + \mathsf{M}^{(1)}_{il} + \mathsf{M}^{(L)}_{il} + \mathsf{M}^{(2)}_{il} + \ldots, \quad (2.84)$$

with the different terms being of the order $\mathscr{O}(1)$, $\mathscr{O}(k)$, $\mathscr{O}\left(k^2 \ln|\kappa_3|\right)$, and $\mathscr{O}\left(k^2\right)$, respectively. This simplification of the velocity tensor indicates that, in the case of a large integral length scale, only the distortion of large turbulent structures can be taken into account to model the alteration of the velocity spectra.

It must be noted that the expansion of M_{il} for $k \to 0$ is valid to $\mathscr{O}\left(k^2 \ln k\right)$, meaning that $\mathsf{M}^{\dagger}_{il}\mathsf{M}_{jm}$ in Eq. (2.81) can be calculated up to this order and that the integral converges only for $r_3 \neq 0$. However, Hunt [45] showed that by introducing the normalised one-dimensional spectrum

$$\hat{\Theta}_{ij}(\hat{\kappa}_1) = (a/L_1)\Theta^*_{ij}(\kappa_1), \quad (2.85)$$

with $\hat{\boldsymbol{\kappa}} = (a/L_1)\boldsymbol{\kappa}$, it is possible to express the distorted spectrum using the following expansion as a series in terms of a/L_1:

$$\hat{\Theta}_{ij}\left(x_1^*, x_2^*, x_1'^*, x_2'^*, r_3^*, \hat{\kappa}_1\right) = \hat{\Theta}_{ij}^{(0)}(\hat{\kappa}_1) + (a/L_1)\,\hat{\Theta}_{ij}^{(1)}(\hat{\kappa}_1) + \\ + (a/L_1)^2 \ln(a/L_1)\hat{\Theta}_{ij}^{(L)}(\hat{\kappa}_1) + \ldots. \quad (2.86)$$

In this way, the first term of the expansion $\hat{\Theta}^{(0)}$ can be calculated using $\mathsf{M}_{il}^{(0)}$, the second term $\hat{\Theta}^{(1)}$ using $\mathsf{M}_{il}^{(0)}$ and $\mathsf{M}_{il}^{(1)}$, and the third term with $\mathsf{M}_{il}^{(0)}$ and $\mathsf{M}_{il}^{(L)}$. These terms can be expressed through explicit analytical relations, but a closed-form solution can be identified only for $\hat{\Theta}_{ij}^{(0)}(\hat{\kappa}_1)$ and $\hat{\Theta}_{ij}^{(1)}(\hat{\kappa}_1)$.

In the case of the auto spectrum, for which $\boldsymbol{x}^* = \boldsymbol{x}'^*$, $i = j$, and $r_3^* = 0$, a further simplification can be applied: $\hat{\Theta}_{ij}^{(1)}$ can be proven indeed to be equal to zero, leading to the following expression for $\hat{\Theta}_{ij}$ as a function of the upstream undistorted spectrum $\hat{\Theta}_{kl,\infty}$:

$$\hat{\Theta}_{ij}(\hat{\kappa}_1) = F_{ijkl}^{(0)}\delta_{kl}\hat{\Theta}_{kl,\infty}(\hat{\kappa}_1) + \mathcal{O}(1), \quad (2.87)$$

with δ_{kl} being the Kronecker delta and

$$F_{ij11}^{(0)} = \mathsf{M}_{i1}^{(0)}\left(\boldsymbol{x}^*\right)\mathsf{M}_{i1}^{(0)}\left(\boldsymbol{x}'^*\right), \quad (2.88a)$$

$$F_{ij22}^{(0)} = \mathsf{M}_{i2}^{(0)}\left(\boldsymbol{x}^*\right)\mathsf{M}_{i2}^{(0)}\left(\boldsymbol{x}'^*\right), \quad (2.88b)$$

$$F_{ij33}^{(0)} = \mathsf{M}_{i3}^{(0)}\left(\boldsymbol{x}^*\right)\mathsf{M}_{i3}^{(0)}\left(\boldsymbol{x}'^*\right). \quad (2.88c)$$

The important result is that the PSD of the one-dimensional spectra can be calculated to $\mathcal{O}(1)$, implying that the variation with a/L_1 can not be obtained [45].

In the case of a circular cylinder, $\mathsf{M}_{il}^{(0)}$ can be expressed by

$$\mathsf{M}_{il}^{(0)} = \begin{bmatrix} 1 - \frac{\left(1-\frac{x_1}{a}\right)^2 - \left(\frac{x_2}{a}\right)^2}{\left[\left(1-\frac{x_1}{a}\right)^2 + \left(\frac{x_2}{a}\right)^2\right]^2} & \frac{2\left(1-\frac{x_1}{a}\right)\frac{x_2}{a}}{\left[\left(1-\frac{x_1}{a}\right)^2 + \left(\frac{x_2}{a}\right)^2\right]^2} & 0 \\ -\frac{2\left(1-\frac{x_1}{a}\right)\frac{x_2}{a}}{\left[\left(1-\frac{x_1}{a}\right)^2 + \left(\frac{x_2}{a}\right)^2\right]^2} & 1 + \frac{\left(1-\frac{x_1}{a}\right)^2 - \left(\frac{x_2}{a}\right)^2}{\left[\left(1-\frac{x_1}{a}\right)^2 + \left(\frac{x_2}{a}\right)^2\right]^2} & 0 \\ 0 & 0 & 1 \end{bmatrix}, \quad (2.89)$$

which, substituted in Eq. (2.87) through Eq. (2.88), finally leads to

$$\Theta_{22}^*(\kappa_1) = \left[1 + \frac{1}{\left(1-\frac{x_1}{a}\right)^2}\right]^2 \Theta_{22,\infty}^*(\kappa_1), \quad (2.90)$$

which is valid on the stagnation streamline ($x_2/a = 0$).

Variance The cross-variance of the velocity components for lateral separation $r_3^* = 0$ can be calculated to zero order in the asymptotic case $L_1/a \gg 1$ through

$$\overline{u_i'^*\left(\boldsymbol{x}^*\right)u_j'^*\left(\boldsymbol{x}'^*\right)} = F_{ijll}^{(0)}\left(\boldsymbol{x}^*, \boldsymbol{x}'^*\right)\delta_{kl}\overline{u_{k,\infty}'^* u_{l,\infty}'^*}. \quad (2.91)$$

This leads to the following expression for the variances:

$$\overline{u_1'^{*2}\left(\boldsymbol{x}^*\right)} = \left(\mathsf{M}_{11}^{(0)}\right)^2 \overline{u_{1,\infty}'^{*2}} + \left(\mathsf{M}_{12}^{(0)}\right)^2 \overline{u_{2,\infty}'^{*2}}, \tag{2.92}$$

$$\overline{u_2'^{*2}\left(\boldsymbol{x}^*\right)} = \left(\mathsf{M}_{21}^{(0)}\right)^2 \overline{u_{1,\infty}'^{*2}} + \left(\mathsf{M}_{22}^{(0)}\right)^2 \overline{u_{2,\infty}'^{*2}}, \tag{2.93}$$

$$\overline{u_3'^{*2}\left(\boldsymbol{x}^*\right)} = \overline{u_{3,\infty}'^{*2}}. \tag{2.94}$$

SMALL-SCALE TURBULENCE

One-dimensional spectra In the high-wavenumber range, Hunt [45] showed that the spectrum of the upwash velocity component in the immediate vicinity of the stagnation point decays with an exponential slope according to

$$\Theta_{22,\mathrm{dis}}^*\left(\kappa_1\right) \simeq G_1 \left(a/L_1\right)^{-\frac{2}{3}} \kappa_1^{-\frac{7}{3}} \mathrm{e}^{-\frac{1}{2}\pi\kappa_1}, \tag{2.95}$$

where

$$G_1 = \frac{55 \times 0.1955 \times \pi^{\frac{1}{2}} \Gamma\left(\frac{1}{3}\right) \Gamma\left(\frac{5}{3}\right)}{36\pi \times 4\pi \times \left(\frac{3}{4}\right)^{\frac{5}{3}} \Gamma\left(\frac{11}{6}\right)} = 0.0566.$$

Variance The calculation of the variance in the case of small-scale turbulence conducted by Hunt [45] is quite complex and not directly necessary for supporting the results presented in this dissertation. However, for completeness, it is useful to report the asymptotic results obtained for a single point along the stagnation streamline at small distances from the stagnation point. These results have also been employed in the literature for direct comparison with experimental measurements [85]. Under these assumptions, the following expressions are found by Hunt [45]:

$$\overline{u_1'^2\left(\boldsymbol{x}^*\right)} = \frac{3}{4}\left[\frac{1}{U_1^*} + \frac{1}{2}U_1^* \ln\left(\frac{4}{U_1^*}\right) + \ldots\right] \overline{u_{1,\infty}'^2}, \tag{2.96}$$

$$\overline{u_2'^2\left(\boldsymbol{x}^*\right)} \simeq \frac{3}{4}U_1^*\left[\ln\left(\frac{4}{U_1^*}\right) - 1\right] \overline{u_{1,\infty}'^2}, \tag{2.97}$$

$$\overline{u_3'^2\left(\boldsymbol{x}^*\right)} \simeq \frac{3}{4}\left[\frac{1}{U_1^*} - \frac{1}{2}U_1^* \ln\left(\frac{4}{U_1^*}\right) \ldots\right] \overline{u_{3,\infty}'^2}. \tag{2.98}$$

The reader may refer to Section 6 of Hunt [45] for the complete analytical calculation.

3

METHODOLOGY

This chapter presents the numerical and experimental set-ups employed to investigate turbulence–interaction noise under both rectilinear and rotational motion.

Lattice–Boltzmann Method (LBM) simulations have been conducted to assess the interaction of grid-generated turbulence with an aerofoil. The numerical set-up replicates the experimental one at the Institute of Sound and Vibration Research (ISVR) at the University of Southampton and was used by Chaitanya et al. [34] for a comprehensive study of turbulence–interaction noise.

The first part of the investigation on turbulence distortion and leading-edge noise generation has been carried out for a NACA 0012 and the NACA 0012-103, which share the same thickness distribution but differ in leading-edge radius. The analysis has then been extended in a second part to the cambered NACA 4412 at two angles of attack, $\alpha = \alpha_{ZL}$ and $\alpha = 1°$.

Although NACA 0012 and NACA 0012-103 were included in the ISVR experimental database used by Chaitanya et al. [34], the NACA 4412 does not feature among the investigated aerofoils. It was introduced in this study to establish continuity between the rectilinear and rotational motion analyses, as it represents the blade section of the propeller investigated in the latter. This analysis, carried out experimentally in the open-jet anechoic wind tunnel of TU Delft (A-Tunnel), reproduces the one carried out by Grande et al. [86]. The description of the experimental set-up includes details of the aerodynamic and acoustic measurements conducted in the campaign.

A description of the commercial LBM solver PowerFLOW, employed for the simulations, is provided at the beginning of the chapter.

3.1. FLOW SOLVER

The commercial software Simulia PowerFLOW 6-2021 is used to compute the flow field. The software is based on the LBM, which models the motion and the collisions of fluid particles at mesoscopic scales through particle-distribution functions. Local integration of these functions, aligned with a finite number of predefined directions, allows the

calculation of flow density, momentum, and internal energy [87]. The Boltzmann equation is solved on a Cartesian mesh (lattice), with the discretisation performed through 19 discrete velocity vectors in three dimensions, i.e. D3Q19, using a third-order truncation of the Chapman-Enskog expansion. This scheme has been shown to be accurate for approximating the Navier-Stokes equation in the case of a perfect gas at low Mach numbers and isothermal conditions [88]. The discretised form of the equation reads

$$F_i\left(\boldsymbol{x}+\boldsymbol{V}_n\Delta t, t+\Delta t\right)-F_i\left(\boldsymbol{x}, t\right)=C_i\left(\boldsymbol{x}, t\right), \tag{3.1}$$

where F_i and $\boldsymbol{V}_i$ are the particle distribution function and the discrete particle velocity along the ith lattice direction at position x and time instant t, respectively.

The collision term C_i is based on the Bhatnagar-Gross-Krook (BGK) model [89]. Despite its limitations [90, 91] and the development of various improvements[92, 93], this model remains widely used for its simplicity and computational efficiency [94, 95]. The BGK model indeed simplifies the discrete LB equation by replacing the collision operator with a single relaxation time τ. The model considers that, within this time scale, the local distribution function approaches the equilibrium one F_i^{eq}, which is approximated with a second-order expansion [88]. This means that the same rate is assumed for all the scales of the relaxation processes, rather than being a function of F_i.

The numerical solver uses a very-large-eddy simulation (VLES) model to account for unresolved scales of turbulence. A modified two-equation $k-\epsilon$ renormalisation group (RNG) turbulence model is used to calculate the turbulent relaxation time, which is added to the viscous relaxation time [96]

$$\tau_{\text{eff}}=\tau+\mathrm{C}_\mu\frac{k^2/\epsilon}{(1+\eta^2)^{1/2}}, \tag{3.2}$$

where $\mathrm{C}_\mu = 0.09$, and η combines local strain, vorticity, and helicity parameters [97]. This mitigates subgrid-scale viscosity so that the resolved large-scale structures are not numerically damped. This relaxation time then calibrates the Boltzmann model to the characteristic time scales of a turbulent flow motion. Reynolds stresses are, hence, an inherent consequence of the chaotic exchange of momentum driven by the turbulent flow. The non-linearity of the stresses is correctly captured by the Chapman-Enskog expansion, making the model suited to represent turbulence in a state far from equilibrium [98].

The LB scheme is solved on a three-dimensional lattice whose basic element is the voxel, i.e. volumetric pixel, whose size varies by a factor 2 in adjacent resolution regions. Surface elements discretise solid surfaces where they intersect voxels. Fluid-particle interaction with the solid surface is governed by wall-boundary conditions, such as a particle bounce-back process for no-slip walls and a specular reflection for slip walls [99]. The wall-shear stress is approximated by means of a wall function applied on the first wall-adjacent voxel. This function is based on the generalised law-of-the-wall model [100], extended to consider the effects of pressure gradient and surface roughness.

The FWH analogy, in formulation 1A of Farassat and Succi [101] extended to a convective wave equation [102], is used in the present work to calculate far-field noise. The formulation is implemented in the time domain using a source-time-dominant algorithm [103]. The analogy has been applied by sampling pressure fluctuations on the aerofoil

surface, making it possible to consider a distribution of acoustic dipoles and monopoles on the surface [77] and to neglect other non-linear contributions, i.e. quadrupole sources.

3.2. LBM SIMULATION SET-UP FOR GRID-AEROFOIL CONFIGURATION

The numerical set-up, shown in Fig. 3.1, reproduces the open-jet wind-tunnel facility at the Institute of Sound and Vibration Research (ISVR) at the University of Southampton, where the experimental campaign of Chaitanya et al. [34] has been carried out. The simulation domain, whose size does not correspond to the actual dimensions of the anechoic chamber for computational requirements, consists of a cube of 5 m side centred at the aerofoil leading edge (in the cases where the angle of attack is equal to zero). This coincides with the origin of the reference frame, whose axes are denoted as x_1, x_2, and x_3, representing the streamwise, upwash, and spanwise directions, respectively. The corresponding velocity components are u_1, u_2, and u_3, while the spatial wavenumbers are indicated with k_1, k_2, and k_3. The chord of the aerofoil is $c = 0.15\,\text{m}$, while its span is $L = 0.45\,\text{m}$. It is placed 1 chord downstream of a convergent nozzle having a rectangular exit section 0.45 m wide and 0.15 m high and a square inlet section of side 1.3 m. The converging part of the ISVR nozzle is 1.35 m long, but in the numerical set-up the tunnel has been extended upstream with a constant square-section duct to allow the inlet boundary conditions to be applied directly at the boundary of the simulation domain. At the exit section of the nozzle, on the sides of the aerofoil, two rectangular plates 0.225 m high and 0.375 m long have been placed to eliminate tip effects. In both the experimental and numerical set-ups, turbulence is generated by a rectangular grid measuring 0.46 m × 0.61 m and positioned 0.63 m upstream of the nozzle exit. The square rods of the turbulence-generating grid, separated by a distance equal to 0.034 m, have a thickness of 0.012 m, resulting in a solidity of 55 %.

The total pressure at the nozzle inlet has been imposed to achieve a free-stream velocity of $U_\infty = 60\,\text{m}\,\text{s}^{-1}$ at $x_1/c = -0.033$ without the aerofoil in the open jet. This free-stream velocity corresponds to a Reynolds number, with respect to the aerofoil chord, of $Re = 6.2 \times 10^5$. The head loss caused by the presence of the turbulence-generating grid has been taken into account using the empirical results of Roach [104], while the friction loss along the nozzle walls has been neglected in the numerical simulation. On all the other boundaries of the cubic domain, a static pressure of 101 325 Pa has been imposed.

10 voxel-refinement regions have been used to discretise the numerical domain at the finest grid resolution. The turbulence-generating grid and the aerofoil are placed into the same refinement region to avoid any variation of the voxel size, which here is $7.19 \times 10^{-4}\,\text{m}$, and affect turbulence convection. The voxel size is further reduced along the aerofoil surface by means of two refinement regions obtained as offsets of the aerofoil geometry, reaching a value of $1.79 \times 10^{-4}\,\text{m}$ along the aerofoil surface. This leads to an average value of y^+ along the surface of the body of 19. The finest resolution configuration hence requires a discretisation of the numerical domain into a total of 660×10^6 voxels.

The simulation time is 0.2295 s, corresponding to 92 flow-through times. After a tran-

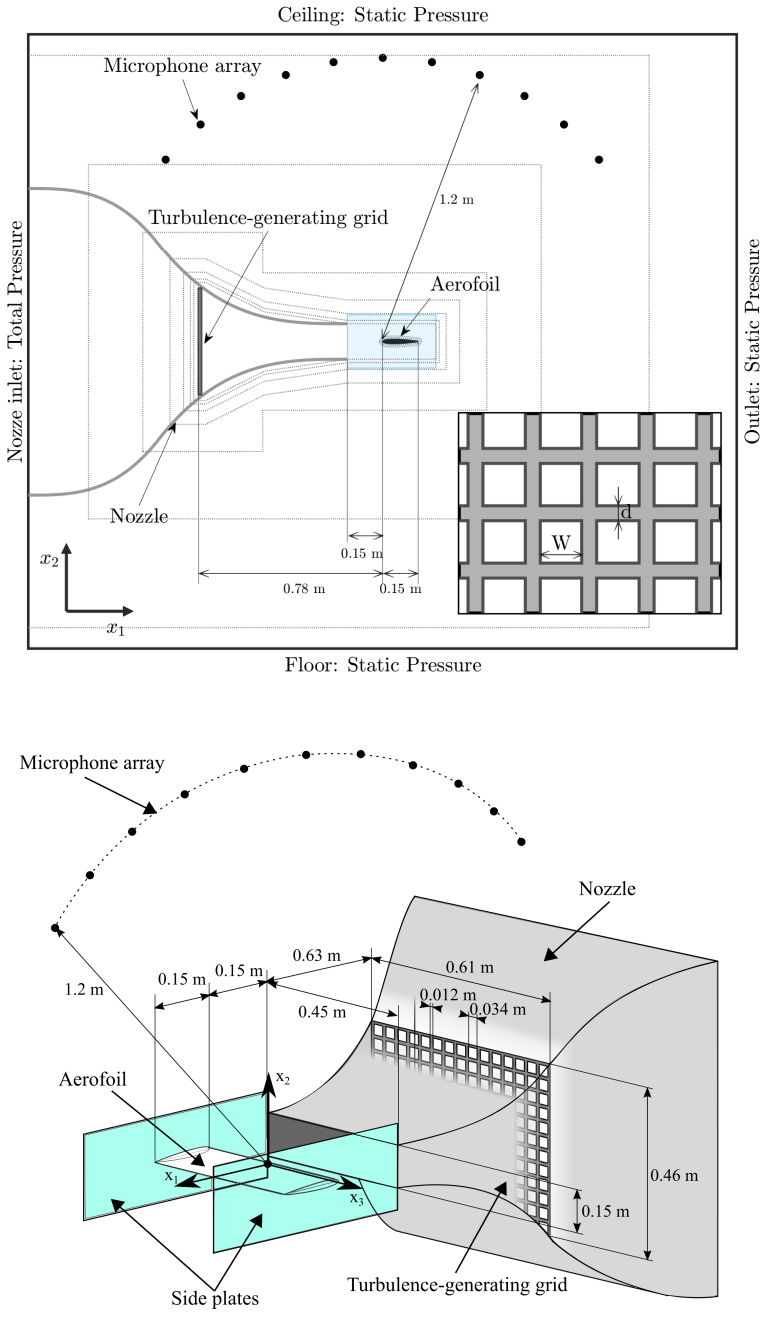

Figure 3.1: Sketch of the simulation domain. The size of the volume is not drawn to scale. The resolution regions are qualitatively represented using dotted lines. The detail in the bottom right corner depicts a sketch of the turbulence-generating grid placed inside the nozzle. The thickness of the square bars d is equal to 0.012 m and the width W of the gap is 0.034 m

.

Table 3.1: Geometrical information about the rectangular grid.

Width [m]	Height [m]	Gap, W [m]	Rod thickness, d [m]	Pattern period, W + d [m]	Solidity, σ_{grid} [%]
0.46	0.61	0.034	0.012	0.046	55

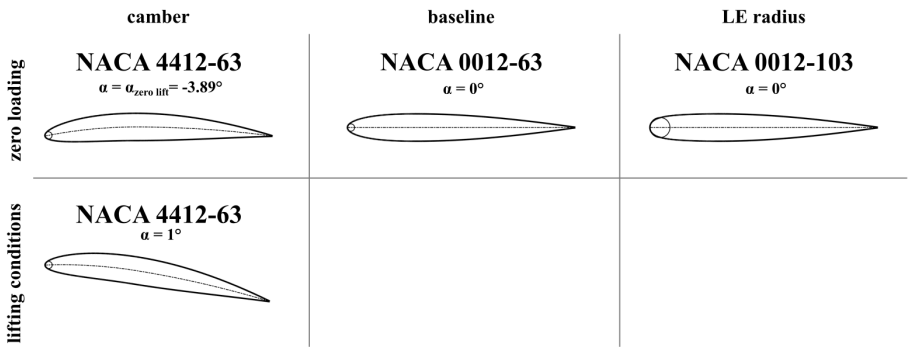

Figure 3.2: Aerofoil configurations analysed in the numerical simulations. The baseline NACA 0012 has been compared to a NACA 0012-103, which is part of the modified 4-digit series and differs only for the radius of the leading edge, and the cambered NACA 4412 investigated at two different loading conditions.

sient of 25 flow-through times, i.e. 0.0625 s, flow quantities have been saved for 0.1670 s, equivalent to 10 repetitions of the cycle at the lowest frequency of interest (60 Hz) and to 67 flow-through times. The physical time step, depending on the grid resolution, is equal to 3.046×10^{-7} s for the finest configuration. The grid-independence study is reported in Subsection 3.2.1, while the aerodynamic and acoustic validations of the numerical simulations are presented in Subsection 3.2.2.

The solid formulation of the FWH analogy, using the pressure sampled on the aerofoil surface, was used to calculate the far-field acoustic radiation. A 30 kHz acquisition frequency has been imposed to obtain flow quantities on the aerofoil surface and in the flow field. The power spectral densities have been computed by means of Welch's method, using a Hanning window with 50 % overlap resulting in a frequency resolution of 100 Hz. The direct far-field noise has also been computed using probes placed along a circle arc in the midspan plane of the aerofoil (Fig. 3.1). This arc, centred at the origin of the numerical domain, features a radius $R = 1.2$ m and ranges from $\theta = 2\pi/9$ and $\theta = 7\pi/9$, with the angle measured with respect to the downstream direction. The angular separation between the 11 probes is $\Delta\theta = \pi/18$.

The physical analysis presented in Chapter 4 is carried out on two symmetrical aerofoil geometries. The first is the standard NACA 0012, used as baseline case, while the second is the NACA 0012-103, which belongs to the NACA-modified four-digit series [34, 36, 105]. Following the notation used for this series, a standard NACA 0012 would be indicated as NACA 0012-63, where 6 is the value of a parameter r_{idx} related to the length of

the leading-edge radius through the relation

$$r_{LE} = 1.1019\left(\frac{t r_{idx}}{6}\right)^2 c,$$

with t being the thickness of the aerofoil. The second digit of the numerical appendix indicates the position of maximum thickness. As a consequence, the NACA 0012-103 will have an increased radius of the leading edge, being $r_{idx} = 10$, but the same thickness and same position of maximum thickness of the other aerofoil investigated. The radius of the leading edge for the standard NACA 0012 is $r_{LE,\,0012} = 2.4 \times 10^{-3}$ m, while for the NACA 0012-103 is $r_{LE,\,0012\text{-}103} = 6.6 \times 10^{-3}$ m. The geometrical data are reported in Table 3.2. These two aerofoils have been selected to analyse the contribution of a different curvature distribution on the leading-edge noise generation and turbulence distortion, keeping the same aerofoil thickness.

To develop the analytical methodology presented in Chapter 5, the investigation was extended to additional configurations. A NACA 4412 has been added to the NACA 0012 and NACA 0012-103 previously analysed to evaluate the impact of aerofoil camber (the NACA 4412 features indeed the same leading-edge radius as the NACA 0012). All three aerofoils share the same thickness distribution. While the NACA 0012 and NACA 0012-103 are included in the experimental study by Chaitanya et al. [34], the NACA 4412 is not. All the aerofoils have been tested at zero loading conditions, which correspond to an angle of attack of $\alpha = 0°$ for the symmetric NACA 0012 and NACA 0012-103 and an angle of attack of $\alpha = -3.89°$ for the cambered NACA 4412. The latter has also been analysed at lifting conditions, selecting an angle of attack α equal to 1°. In the cases of the cambered aerofoil, positioned at incidence different from zero, the angle of attack has been obtained by rotating the aerofoil around the position at $\frac{1}{4}$ of the chord. All the information regarding the geometry of the aerofoils is reported in Table 3.2, while the investigated configurations are illustrated in Fig. 3.2.

The curvature of the aerofoil is derived analytically from the formulation of NACA aerofoils and is expressed as

$$C_s = r_{LE}\frac{\ddot{x}_{2,NACA}}{\left(1+\dot{x}^2_{2,NACA}\right)^{3/2}},$$

where $x_{2,NACA}$ denotes the ordinate of the NACA aerofoil profile, and derivatives (indicated by dots) are taken with respect to the abscissa $x_{1,NACA}$. Since the curvature is defined as the inverse of the radius of curvature, the non-dimensional curvature C_s is obtained by scaling the expression with the leading-edge radius r_{LE}.

3.2.1. GRID-INDEPENDENCE STUDY

The grid-independence study was performed for the NACA-0012 baseline case. For this configuration, five simulations with different resolutions have been carried out. With respect to the coarsest simulation, identified as “resolution level 1", the following one, i.e. “resolution level 2", is obtained using a refinement factor of 2. The third and the fourth levels of refinement have been achieved by refining the second resolution level with factors of 1.5 and 2, respectively. The fifth and finest resolution level is obtained

NACA	chord, c (m)	span, L (m)	LE radius, r_{LE} (m)	angle of attack, α (deg)
0012	0.15	0.45	2.4×10^{-3}	0
0012-103	0.15	0.45	6.6×10^{-3}	0
4412	0.15	0.45	2.4×10^{-3}	−3.89 1

Table 3.2: Investigated configurations and geometrical information of the four analysed aerofoils.

Table 3.3: Comparison of the simulation characteristics for the NACA-0012 configuration.

Resolution level	Resolution [r_{LE}/finest voxel]	Total amount of voxel [−]	CPU time [hours]
1	3.31	14×10^6	0.80×10^3
2	6.62	91×10^6	7.48×10^3
3	9.93	287×10^6	24.99×10^3
4	13.25	660×10^6	44.75×10^3
5	26.50	900×10^6	96.58×10^3

by adding a further refinement region on the aerofoil surface. Convergence is assessed in terms of sound power level (PWL) and time-averaged lift and drag coefficients of the aerofoil, i.e. $\overline{C}_L$ and $\overline{C}_D$, respectively. Table 3.3 reports additional information about the different resolution levels.

The solid formulation of the FWH analogy is employed to calculate the far-field noise at the virtual microphones described in Sec. 3.2. The PWL is computed with the expression used in the reference experimental campaign:

$$\mathrm{PWL} = \left(\frac{\mathrm{LR}}{\rho_\infty c_\infty}\right)\left[\sum_{i=1}^{N-1}\frac{S_{pp}(f,\theta_i)+S_{pp}(f,\theta_{i+1})}{2}\Delta\theta\right], \tag{3.3}$$

with L being the span of the aerofoil, R the radius of the microphone array, c_∞ the speed of sound, and ρ_∞ the density of air. $S_{pp}(f,\theta_i)$ is the power spectral density of the far-field acoustic pressure at position θ_i, while $\Delta\theta$ is the angular separation between two adjacent microphones. The procedure is explained in further detail by Narayanan et al. [106].

The comparison of the PWLs for the different resolution levels is illustrated in Fig. 3.3 as a function of St_t, computed with respect to the aerofoil thickness. The Strouhal range from $St_t = 0.15$ to $St_t = 1.5$ is highlighted since leading-edge noise dominates in this range [34]. The transparent grey patches in the plots cover the frequency ranges where background noise ($St_t < 0.15$) and self-noise ($St_t > 1.5$) prevail in the experimental campaign. The trends obtained for the different grid resolutions almost overlap up to $St_t = 2.5$, demonstrating that the results are grid independent in the range of interest from resolution level 3. For $St_t > 2.5$, the effects related to the different resolutions are more evident, particularly for resolution levels 1 and 2. This is due to the coarser refinement

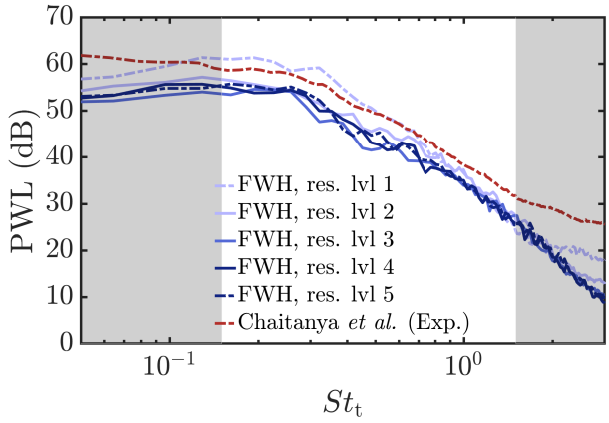

Figure 3.3: Grid-independence study in terms of PWL for the different grid resolutions for the NACA-0012 case.

around the aerofoil surface, where the unsteady pressure used to apply the FWH analogy is sampled.

The convergence trends of $\overline{C}_L$ and $\overline{C}_D$ are shown in Fig. 3.4 with respect to the total amount of voxels expressed in logarithmic scale. The trend of the drag coefficient indicates that convergence has also been reached in terms of aerodynamic forces at resolution level 4. Conversely, the lift coefficient tends to a constant value as the resolution increases but does not converge to zero, as it would be expected for a symmetric aerofoil placed at a 0° angle of attack. A small incidence is likely due to the highly turbulent flow in which the aerofoil is immersed and to the slight upward deflection of the flow at the exit of the open-jet wind tunnel. This hypothesis is corroborated by the results of the turbulence characterisation in Subsection 3.2.3, which shows that the time-averaged upwash velocity component is non-zero at the aerofoil position. However, this effect is deemed negligible, as it corresponds to a variation of the angle of attack estimated from the lift curve of a NACA 0012 aerofoil at the current Reynolds number of approximately 0.25° and does not affect the analysis presented herein.

In view of the above, it can be concluded that convergence has already been achieved at resolution level 4. Consequently, this resolution level has been selected to carry out the investigation for the NACA 0012 and for the simulation of the NACA 0012-103, considering the excessively high computational cost required to run a simulation at resolution level 5.

3.2.2. VALIDATION

The validation study is performed by comparing the aerodynamic and acoustic results obtained in the configurations at resolution level 4 of the two aerofoils with the data from the reference experimental campaign of Chaitanya et al. [34]. For the aerodynamic validation, the flow at the nozzle exit has been assessed in terms of streamwise integral length scale, turbulence intensity, and turbulence frequency spectrum of the streamwise velocity component at $x_1/c = -0.033$ upstream of the position of the leading edge. The

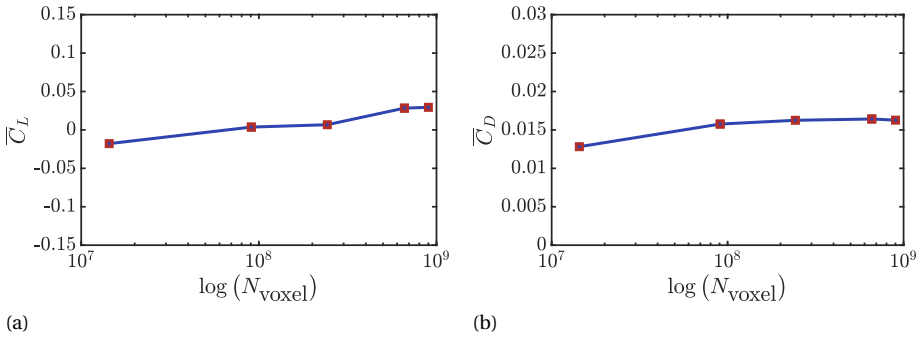

Figure 3.4: Grid-independence study in terms of time-averaged (a) lift coefficient $\overline{C}_L$ and (b) drag coefficient $\overline{C}_D$ for the different grid resolutions for the NACA-0012 case.

flow characterisation has been carried out by running a simulation in which the aerofoil is removed while keeping the resolution and the refinement regions unaltered. By sampling the velocity components at this position, a time-averaged free-stream velocity of $U_\infty = 59.5\,\mathrm{m\,s^{-1}}$ and a turbulence intensity $\mathrm{Tu}_1 = \sqrt{\overline{u_1'^2}}/U_\infty$ of 2.2 % are obtained. The streamwise integral length scale is equal to $\mathrm{L}_1 = 6.0 \times 10^{-3}\,\mathrm{m}$, and it has been estimated using the expression [107]

$$L_{ij}^m(\boldsymbol{x}, l) = \int_0^\infty R_{ij}^m(\boldsymbol{m})\,\mathrm{d}l = \int_0^\infty \frac{\overline{u_i(\boldsymbol{x} + l\boldsymbol{e}_m)\,u_j(\boldsymbol{x})}}{u_i(\boldsymbol{x})\,u_j(\boldsymbol{x})}\,\mathrm{d}l \quad . \tag{3.4}$$

It must be noted that, when $i = j = m$, the notation L_{ij}^m will be simplified into L_i. $R_{ij}^m(x)$ is the correlation coefficient calculated considering a reference location x, u_i and u_j are the turbulent velocity fluctuations components in the ith and jth directions, respectively, $\boldsymbol{e}_m$ is the unitary vector in the mth direction, and $l = \boldsymbol{l} \cdot \boldsymbol{e}_m$ is the separation length from the reference location. $\bar{\cdot}$ is the temporal-averaging operator with the assumption that the turbulent fluctuations in the open jet are ergodic. The expression has been applied using a discrete integration with respect to the streamwise velocity component, and the calculation is independent of the spatial separation between the sampling points. The values calculated for these quantities are compared with the results obtained in the reference experimental work of Chaitanya et al. [34]. The comparison is reported in Table 3.4, where a good agreement is shown between the turbulence characteristics of the reference experimental campaign and those obtained in the present numerical simulation.

The same values are subsequently used to scale the von Kármán wavenumber spectra for the streamwise and upwash velocity components, using the expressions

$$\Theta_{11}(k_1) = \frac{1}{\sqrt{\pi}} \frac{\Gamma(5/6)}{\Gamma(1/3)} \frac{\overline{u_1^2}}{k_\mathrm{e}} \frac{1}{\left[1 + (k_1/k_\mathrm{e})^2\right]^{5/6}}; \tag{3.5}$$

Table 3.4: Nozzle open-jet flow characterization. Data are sampled at $x/c = -0.033$ with respect to the origin of the reference system (coincident with the leading edge of the aerofoil) and compared with the measurements of the reference experimental campaign by Chaitanya et al. [34].

	U_∞ $[m\,s^{-1}]$	Tu_u [%]	L^x_{uu} [m]
Present (LBM-VLES)	59.5	2.2	6.0×10^{-3}
Chaitanya et al. [34] (Exp.)	60	2.5	7.5×10^{-3}

$$\Theta_{22}(k_1) = \frac{2}{27\sqrt{\pi}} \frac{\Gamma(5/6)}{\Gamma(7/3)} \frac{\overline{u_2^2}}{k_e} \frac{3 + 8(k_1/k_e)^2}{\left[1 + (k_1/k_e)^2\right]^{\frac{11}{6}}}, \tag{3.6}$$

where $\Gamma(\cdot)$ is the Gamma function, k_1 is the wavenumber in the streamwise direction, and k_e is defined as the wavenumber scale of the largest eddies according to the expression [108]

$$k_e = \frac{\sqrt{\pi}}{L_1} \frac{\Gamma(5/6)}{\Gamma(1/3)}. \tag{3.7}$$

The comparison of the von Kármán spectrum scaled with the quantities sampled at $x_1/c = -0.033$ and the turbulence frequency spectrum acquired at the same position is reported in Fig. 3.5. The turbulence spectra of the streamwise velocity component have also been compared with the results provided in the reference experimental work (Fig. 3.5a). The sampled spectrum and the analytical computation are indeed very similar, while the difference with the von Kármán spectrum obtained in the experimental campaign is most likely due to the slight discrepancy in the integral length scale and turbulence intensity.

The analysis of the upwash velocity component spectrum, reported in Fig. 3.5b, has been carried out considering just the turbulence frequency spectrum sampled at $x_1/c = -0.033$ and the von Kármán spectrum scaled with the quantities sampled at this location. This has been scaled using a value for the turbulence intensity of the upwash velocity component $Tu_2 = \sqrt{\overline{u_2'^2}}/U_\infty$ equal to 2.8%. No information regarding the upwash velocity component, either in terms of the frequency spectrum and turbulence intensity, is reported in the reference experimental work of Chaitanya et al. [34]. A good agreement is observed between the numerical turbulence spectrum and the analytical one, in particular for frequencies above 1 kHz. In the low-frequency range, the von Kármán spectrum clearly underestimates the trend of the numerical spectrum. This suggests that the turbulent flow features a slight anisotropy, which is most likely due to the strong section contraction in the final part of the nozzle and to the fluctuations induced in the flow by the two shear layers developing on the upper and lower sides of the exit section. As the homogeneity and the isotropy of the incoming turbulence are not necessary conditions for the present investigation, turbulence characteristics will be further detailed for the sake of completeness in Subsection 3.2.3.

The acoustic validation is performed in terms of PWL and overall sound pressure level (OASPL) directivity patterns. The noise prediction obtained using the FWH analogy along the arc where the direct microphones are placed has been compared with the

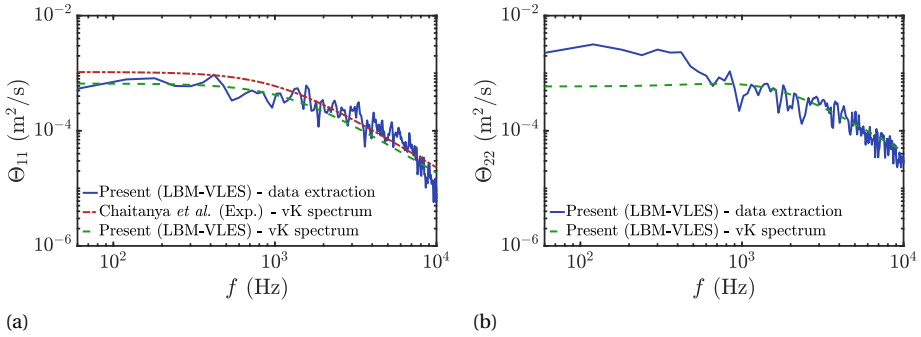

Figure 3.5: Power spectral density of the streamwise velocity component acquired at $x_1/c = -0.033$ with respect to the position of the leading-edge. The spectrum is compared with the von Kármán (vK) spectrum scaled using the integral length scale $L_1 = 6.0 \times 10^{-3}$ m and the turbulence intensity $Tu_1 = 2.2\%$ calculated at the same position. The streamwise component spectra are also compared with the von Kármán spectrum scaled with the results of the reference experimental campaign of Chaitanya et al. [34] ($L_1 = 7.5 \times 10^{-3}$ m; $Tu_1 = 2.5\%$).

experimental data, which deployed 18 microphones on an arc spanning from $\theta = \pi/4$ to $\theta = 3\pi/4$ with a radius R = 1.2 m. The comparison of the PWL is shown in Fig. 3.6 as a function of the Strouhal number calculated with respect to the aerofoil thickness St_t. Additionally, the computational aeroacoustics (CAA) results obtained in the work of Chaitanya et al. [34] are shown for the sake of completeness. For both aerofoils, a 3 dB underprediction is achieved in the frequency range going from $St_t \simeq 0.15$ to $St_t \simeq 1.5$, where leading-edge noise dominates. An error margin of ±2 dB has been considered for the measurements, as indicated by the authors of the experimental campaign. The difference between the numerical and the experimental acoustic data can be traced back to the discrepancy between the turbulence characteristics obtained in the simulation and those measured experimentally. This also concerns the blockage effects in the wind tunnel caused by the aerofoil, which may differ slightly between the simulation and the experiment. A similar satisfactory agreement between the numerical simulations and the measurements is observed in Fig. 3.7, where the OASPL directivity patterns are shown. The OASPL has been determined by integrating the frequency range going from $St_t = 0.15$ to $St_t = 1.5$.

3.2.3. TURBULENCE CHARACTERISATION

The characteristics of the grid-generated turbulence at the exit of the open-jet wind tunnel are further investigated by assessing the flow anisotropy and homogeneity. The analysis of the turbulence characteristics at the nozzle exit, carried out in terms of turbulence intensity of the velocity components and turbulence spectra, has highlighted a slight anisotropy of the flow. More specifically, the fluctuation of the upwash velocity component appears to be larger than that of the streamwise velocity component. This is consistent with the known behaviour of turbulent structures experiencing a distortion caused by a contraction, which leads indeed to an increase of vorticity along the axis of the contraction and a consequent decrease in the two normal directions. This

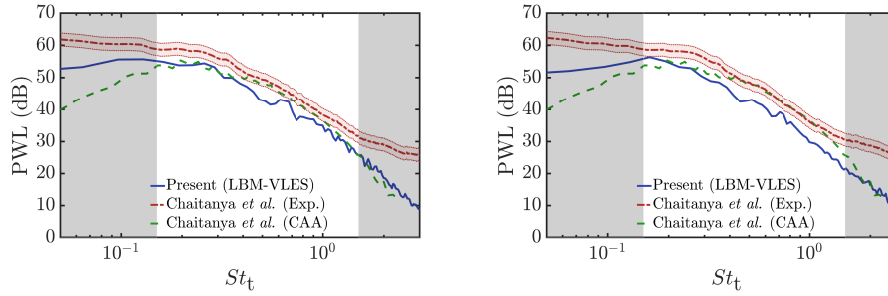

Figure 3.6: Acoustic validation for the (a) NACA 0012 and (b) NACA 0012-103 configurations in terms of sound power level.

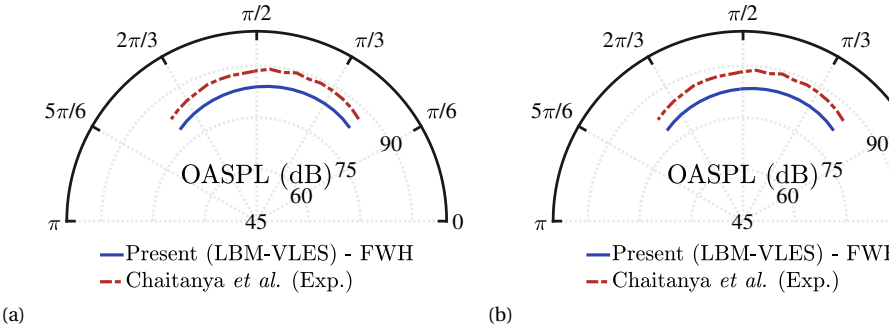

Figure 3.7: Acoustic validation for the (a) NACA 0012 and (b) NACA 0012-103 configurations in terms of noise-directivity pattern.

causes the energy to redistribute from the streamwise to the upwash and spanwise velocity fluctuations [22, 47, 109, 110]. As shown by Batchelor and Proudman [47], the energy redistribution is proportional to the contraction ratio, which is related to the section variation in the final part of the nozzle. Considering the dimensions of the grid-generating turbulence and the nozzle exit section, the contraction is equal to 4.16. This value is significantly larger than those commonly employed in the literature to adjust the flow anisotropy downstream of a grid, which are in the order of 1 [109–111], and explains the higher fluctuation observed for the upwash velocity component with respect to the isotropic state observed in Subsection 3.2.2.

The variations of the ratio between the root-mean-square of the velocity-components fluctuations in the streamwise direction, shown in Fig. 3.8, are a further confirmation of the hypothesis formed above. These trends, showing the evolution of the flow from $x_1/c = -1.5$ to $x_1/c = 0$, indicate that the upwash velocity component and the spanwise velocity one feature increasingly similar fluctuations, larger than those characterising the streamwise velocity component. An ancillary x-axis is reported to indicate the

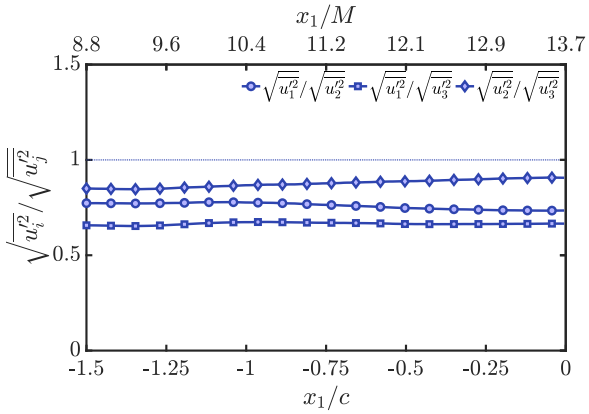

Figure 3.8: Ratios of the root-mean-square of the three velocity components along the stagnation streamline between $x_1/c = -1.5$ and $x_1/c = 0$.

variation of the ratios with respect to the distance from the turbulence-generating grid, expressed in terms of the mesh size W.

However, this analysis only provides information on the isotropy of the energy-containing scales. As emerged from the study of the turbulence frequency spectrum of the upwash velocity component (Fig. 3.5b), the anisotropy characterises mostly the large scales of turbulence. The following relations for the velocity derivatives are more representative of the behaviour and characteristics of small-scale structures [111]:

$$\overline{\left(\frac{\partial u_1'}{\partial x_3}\right)^2} = 2\overline{\left(\frac{\partial u_1'}{\partial x_1}\right)^2}, \tag{3.8a}$$

$$\overline{\left(\frac{\partial u_3'}{\partial x_1}\right)^2} = 2\overline{\left(\frac{\partial u_1'}{\partial x_1}\right)^2}, \tag{3.8b}$$

$$-\overline{\left(\frac{\partial u_1'}{\partial x_3}\right)\left(\frac{\partial u_3'}{\partial x_1}\right)} = \frac{1}{2}\overline{\left(\frac{\partial u_1'}{\partial x_1}\right)^2}. \tag{3.8c}$$

Fig. 3.9 reports these relations in the form of ratios with respect to $\overline{\left(\frac{\partial u_1'}{\partial x_1}\right)^2}$. Satisfactory isotropy levels are observed as the flow develops in the streamwise direction, with the curves of equations 3.8a and 3.8b overlapping with the asymptote at 2 and that of equation 3.8c very close to 1/2.

Skewness S_k and kurtosis K_r of the streamwise velocity component along the stagnation streamline have also been investigated to assess the similarity of the probability density function (PDF) of this fluctuating velocity component to a Gaussian distribution [112, 113]. The results are reported in Fig. 3.10. The skewness and kurtosis of the upwash and spanwise velocity components are omitted in this study since they show very similar behaviour to that of the streamwise velocity. Both S_k and K_r stay within the ranges specified in the literature to indicate the isotropy of the flow, equal to $[-1, 1]$ for the skewness and to $[2, 4]$ for the kurtosis.

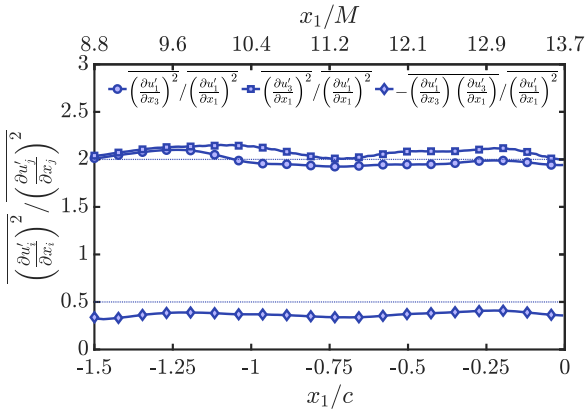

Figure 3.9: Ratios of the second-order velocity derivative moments of Eq. 3.8 along the stagnation streamline between $x_1/c = -1.5$ and $x_1/c = 0$.

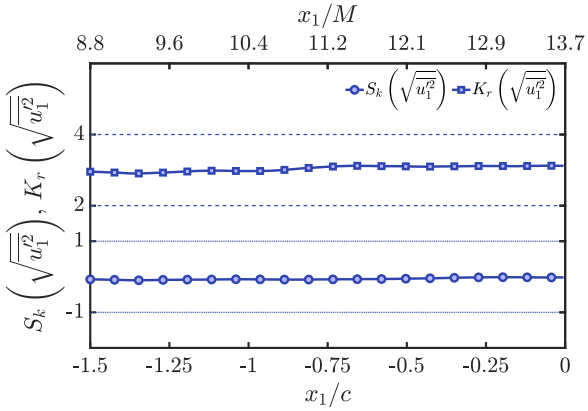

Figure 3.10: Skewness and kurtosis of the streamwise velocity component along the stagnation streamline between $x/c = -1.5$ and $x/c = 0$.

Further information on the turbulent flow after the distortion occurring in the final part of the nozzle is obtained by analysing the anisotropy invariant map, also known as Lumley triangle [114–116]. This technique provides insight into the return to isotropy of grid-generated turbulence by using the second and third invariants of the anisotropy tensor, whose non-dimensional form is

$$b_{ij} = \frac{\overline{u_i' u_j'}}{2k_t} - \frac{1}{3}\delta_{ij}, \tag{3.9}$$

with δ_{ij} being the Kronecker delta and $k_t = \overline{u_i' u_i'}/2$ the turbulent kinetic energy, related to the trace of the Reynolds stress tensor. For incompressible flows, the invariants I, II,

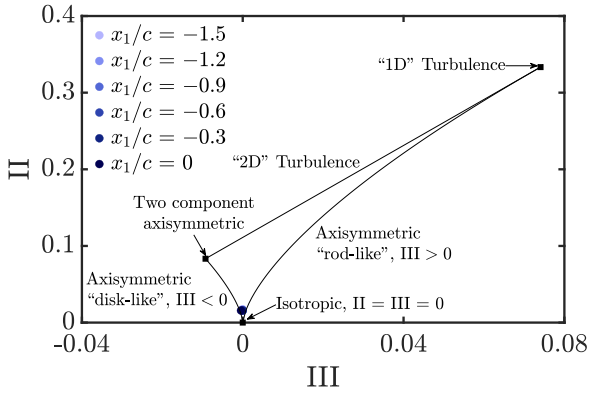

Figure 3.11: Anisotropy invariant map for 6 positions along the streamwise direction (indicated in the plot) at $x_2 = 0$ and $x_3 = 0$. The position where the aerofoil will be placed is reported as a reference in the plot below.

and III are retrieved by the anisotropy tensor terms through the expressions

$$\mathrm{I} = b_{kk} = 0, \tag{3.10}$$

$$\mathrm{II} = \frac{b_{ij}b_{ji}}{2}, \tag{3.11}$$

$$\mathrm{III} = \frac{b_{ij}b_{jn}b_{ni}}{3}, \tag{3.12}$$

which are used to create a coordinate system (III), (II) [117]. The range of invariants, and hence the possible states of turbulence, must fall within the boundaries shown in Fig. 3.11: one-dimensional turbulence (III = 2/27 and II = 1/3) in the right-hand corner, two-component axisymmetric turbulence (III = −1/108 and II = 1/12) in the left-hand corner, and isotropic turbulence (III = 0 and II = 0) at the origin of the plot. Turbulence in the left region has one component smaller than the other two, as in the case of an axisymmetric contraction [117], and is defined as "disk-like" or "pancake-shaped" turbulence. In the right region, turbulence has one component of the turbulent kinetic energy higher than the other two, as occurs for axisymmetric expansion, and is defined as "rod-like" or "cigar-shaped" [116]. The anisotropy tensor invariants are calculated at 6 positions equally spaced along the streamwise direction between $x_1/c = -1.5$ and $x_1/c = 0$ in the midspan plane ($x_2 = 0$, $x_3 = 0$), thus yielding 6 points in the invariant map. The results, reported in Fig. 3.11, indicate that turbulence slightly tends to the left-hand side of the triangle, consistent with the distortion mechanism occurring in a converging section, but is close to the isotropic condition.

Finally, flow homogeneity at the nozzle exit is assessed by analysing the spanwise distribution of the time average and the root-mean-square of the three velocity components. These distributions are shown from $x_3/c = -0.36$ to $x_3/c = 0.36$ in Fig. 3.12a, 3.12c, 3.12e, and Fig. 3.12b, 3.12d, 3.12f, respectively. The time-averaged values of the streamwise velocity component show a progressive acceleration at the exit of the nozzle, as expected. For the upwash velocity component, whose distribution can be considered

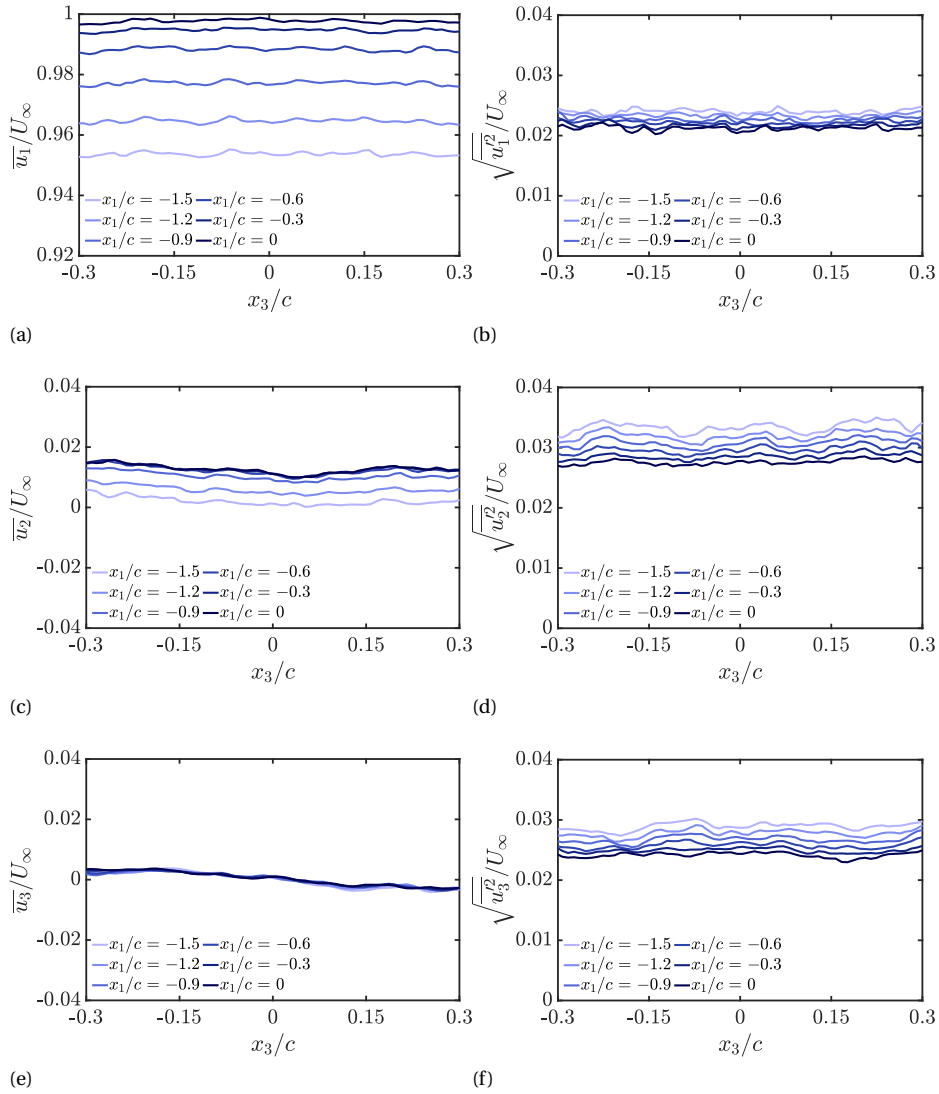

Figure 3.12: Spanwise distribution of the (a), (c), (e) time-average and (b), (d), (f) root-mean-square of the three velocity components at 6 different positions along the stagnation streamline between $x_1/c = -1.5$ and $x_1/c = 0$.

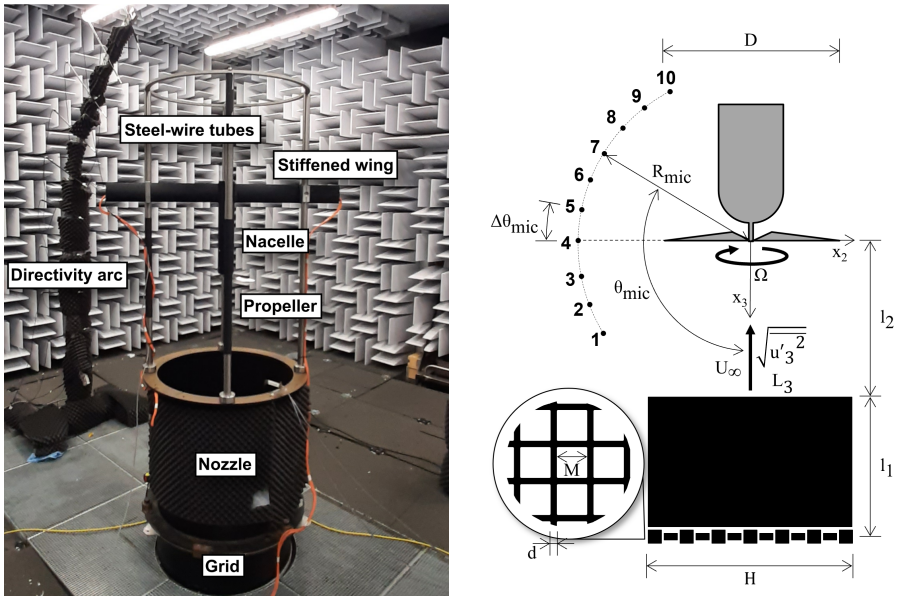

(a) (b)

Figure 3.13: (a) Picture of the experimental set-up mounted in the A-Tunnel at TU Delft and (b) descriptive sketch of the set-up with the main dimensions, distances, and operational parameters.

homogeneous in the spanwise direction, a small increase below 2 % of the free-stream streamwise velocity is found. The spanwise velocity component remains equal to zero.

As regards the spanwise distribution of the root-mean-square of the velocity fluctuations, all three components exhibit a progressive decrease in the streamwise direction. At the upstream locations inside the nozzle, a spanwise periodicity still characterises the distributions of the upwash velocity component and, mildly, the spanwise one. This indicates that the coalescence of the wakes generated by the rectangular grid, whose collection constitutes the turbulent flow field [118], is still ongoing in the last part of the nozzle. This periodic pattern reduces as the distance from the nozzle exit increases, and a homogeneous condition is reached at the most downstream position, where the aerofoil is placed.

3.3. EXPERIMENTAL SET-UP FOR GRID-ROTOR CONFIGURATION

The experimental campaign has been conducted in the anechoic wind tunnel (A-Tunnel) of the Flow Physics and Technology Department of TU Delft. This facility consists of a vertical open-jet wind tunnel, with the test section being an anechoic chamber lined with melamine wedges. To avoid potential acoustic reflections, the metal grids that typically cover the sound-absorbing foam on the floor were removed during the noise measurements. A detailed description and characterisation of this wind tunnel is provided by Merino-Martínez et al. [119]. A picture of the rig in the anechoic chamber is reported in Fig. 3.13, which also shows a qualitative sketch of the experimental set-up with the main

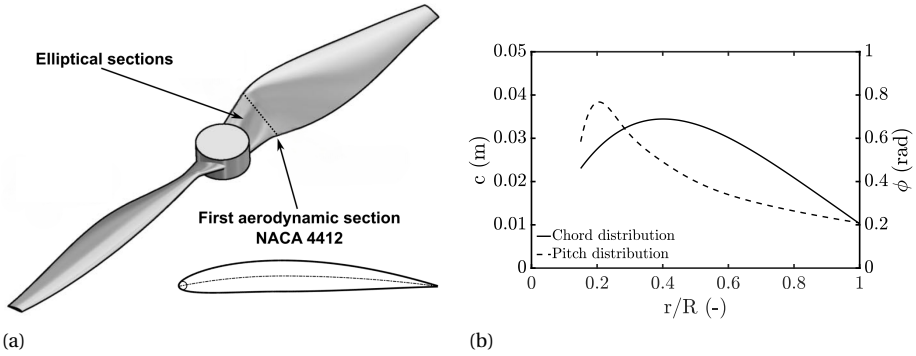

Figure 3.14: (a) 3D model of the two-bladed propeller and (b) chord and pitch angle distributions.

dimensions, distances, and operational parameters. The reference system is consistent with the notation used in Amiet's formulation [80]. The origin is set at the rotor hub, the axial direction, aligned with the free-stream velocity but oriented in the opposite direction, is denoted by x_3, and the x_1 and x_2 axes lie in the rotor plane, forming a right-hand coordinate system. The corresponding velocity components, as introduced in Chapter 2, are indicated with u_3, u_1 and u_2.

A constant-section circular nozzle with diameter H and length l_1 equal to 0.60 m has been placed at the exit of the tunnel. Turbulence is generated by a rectangular grid positioned upstream of the constant-section nozzle to minimise background noise. The grid consists of rectangular bars with a width of $d = 0.01$ m and a mesh length of $M = 0.10$ m, as shown in the detail of Fig. 3.13. The free-stream velocity at the nozzle exit is $U_\infty = 9.5\,\mathrm{m\,s^{-1}}$, with a turbulence intensity $\sqrt{\overline{u_3'^2}}/U_\infty = 6\,\%$ and an integral length scale of the axial velocity component in the same direction $L_3 = 0.018$ m. These flow characteristics have been obtained through hot-wire measurements, as described in Subsection 6.3.1, conducted at the nozzle exit without the propeller.

The propeller and test rig used in this experimental campaign are the same as used by Grande et al. [86]. The test rig consists of an aluminium nacelle with a diameter of 0.05 m, which stems from a stiffened hollow aluminium NACA-0012 wing with a 0.06 m chord. The entire structure is suspended above the tunnel nozzle by four steel-wire tubes, each with a diameter of 2 cm, secured to the tunnel to minimise vibrations and interference. Thin rubber layers have been added between the stiffened wing and the steel-wire tubes, as well as at the joints where the tubes attach to the nozzle lip, to further dampen vibrations.

The structure is mounted so that the propeller is positioned downstream of the exit of the nozzle at a distance $l_2 = 0.40$ m. The propeller APC 9 × 6, which has a diameter of 9″ (0.229 m) and a pitch of 6″ (0.152 m), has been used as a reference to design the propeller of the present investigation. This has been obtained by scaling the diameter to D = 0.30 m and reshaping the blade sections to a NACA-4412 profile, except for the first 0.01 m, which features an elliptical section. Figure 3.14 reports the chord and twist angle distributions of the blade. Further details on the design of the propeller can be found in

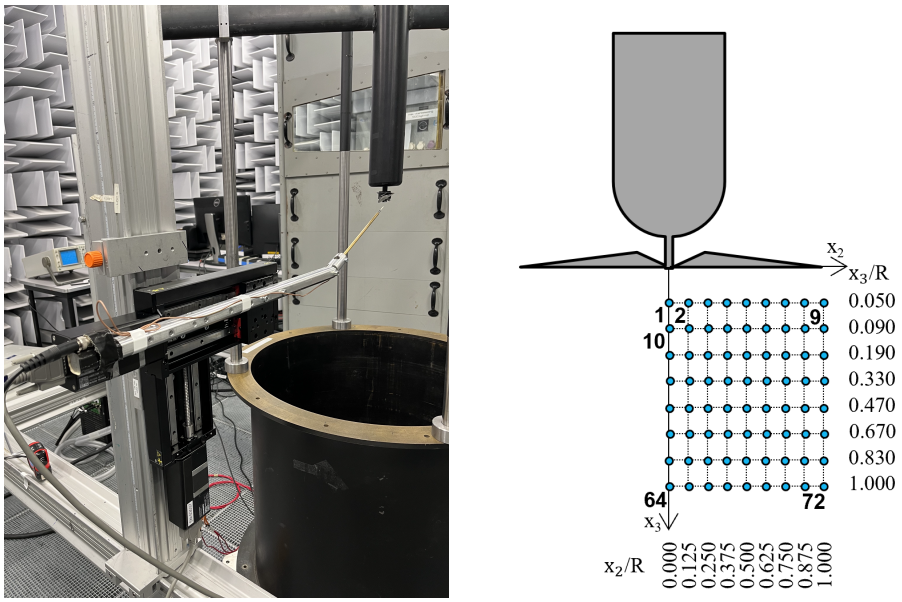

(a) (b)

Figure 3.15: (A) HWA setup and (B) HWA locations. Axial (streamwise) and radial (crosswise) distances are reported in terms of the propeller radius R.

Grande et al. [86].

The nacelle contains the motor driving the propeller, a Lehner Motors LMT 2280/34 brushless inrunner. It features 2280 windings, which results in a motor velocity constant K_v of 218 RPM/V. This constant defines how many revolutions per minute (RPM) the motor turns per volt of applied voltage under no-load conditions. The motor is controlled by a trapezoidal electronic speed controller (ESC) that operates using pulse width modulation (PWM) and is powered by an external programmable 5 kW direct current (DC) power source.

Three different rotational speeds, i.e. 4000 RPM, 6000 RPM, 8000 RPM, have been investigated to validate the proposed methodology. Calculating the advance ratio as $J = U_\infty / n\mathrm{D}$, with n being the propeller rotational frequency in Hz, the resulting values correspond to $J = 0.45$, $J = 0.30$, and $J = 0.23$, respectively.

ACOUSTIC MEASUREMENTS

A directivity arc, equipped with 10 G.R.A.S. 40PH analog free-field microphones, has been used to take acoustic measurements. The microphones have a diameter of 7 mm, a frequency range between 10 and 20 kHz, and a maximum sound pressure level (SPL) of 135 dB. The arc has a radius of 1.5 m, but the microphones have been placed at $R_{\mathrm{mic}} = 1.3$ m from the rotor hub. The angular positions of the 10 microphones are referenced to the rotor axis, as illustrated in Fig. 3.13. Microphone 1 is positioned at $\pi/3$, oriented upstream with respect to the rotor plane, while microphone 10 is located at $5\pi/6$. The

Table 3.5: Experimental Test Matrix. The free-stream velocity was kept constant at $9.5\,\mathrm{m\,s^{-1}}$, meaning that the advance ratios at the three rotational speeds considered are $J = 0.45$, $J = 0.30$, and $J = 0.23$, respectively. Colored cells indicate cases where HWA measurements are available.

Grid	Motor	Propeller	Rotational speed 4000 [RPM]	6000 [RPM]	8000 [RPM]	Description
Off	Off					Background noise (clean)
	On	Off	•	•	•	Background noise (clean) + motor
		On	•	•	•	Propeller noise with clean inflow
On	Off					Background noise (turbulent)
	On	Off	•	•	•	Background noise (turbulent) + motor
		On	•	•	•	Propeller noise with turbulent inflow

angular spacing between two adjacent microphones is $\Delta\theta_{\mathrm{mic}} = \pi/18$.

The calibration of the microphones has been performed using a G.R.A.S. 42AA pistonphone with a calibration level of 114 dB and a reference sound pressure of 20 µPa. A National Instrument PXIe-4499 has been used to acquire the acoustic data and the encoder signal. The signals measured by the microphones have been recorded for 60 s at a sampling frequency of 51.2 kHz. Finally, Welch's method has been applied with a Hanning window characterised by a 50% overlap to obtain the PSDs with a frequency resolution of 100 Hz.

AERODYNAMIC MEASUREMENTS

The flow approaching the propeller has been characterised by hot-wire anemometry (HWA). The fluctuations measured using this technique are primarily aligned with the mean velocity [120], which in this case corresponds to the axial direction. Flow velocity has been measured on a point grid of 8 streamwise positions and 9 radial positions, as shown in Fig. 3.15. The probe, a platinum-plated tungsten wire 5 µm wide and 1.25 mm long, is a Dantec Dynamics P11 ($R_{20} = 3.4$, $R_l = 0.5$, $\alpha_{20} = 0.36$) operated using a constant temperature bridge and is mounted on a remotely operated 2D traversing system. Measurements are performed at a sampling frequency of 51.2 kHz for 60 s. The same parameters for Welch's method as in the aeroacoustic measurements have been applied to process the HWA data.

TEST MATRIX

The investigated cases are summarised in the test matrix of Table 3.5. Acoustic measurements have been taken for all configurations, for a total of 14 cases considering that 3 different RPM values are taken into account for each flow condition. Conversely, HWA measurements have been performed only for the configuration without the propeller in order to characterise the turbulent inflow at the nozzle exit and in the propeller case at 6000 RPM, considered the baseline one. The configurations where aerodynamic measurements are available are indicated with a colored cell in the table.

4

PHYSICAL ANALYSIS

The objective of this chapter is to improve the understanding of turbulence-distortion mechanisms and their impact on sound radiation by analysing the velocity field and unsteady surface pressures in the stagnation region of realistic aerofoils. This physical description represents a key step for developing approaches that can accurately predict leading-edge noise in low-fidelity methods. The results discussed support a prediction methodology for extending the theory of Amiet [16] by incorporating turbulence-distortion effects into the model. This approach eliminates the need to prescribe a sampling location for the turbulence characteristics, as done in prior studies, and requires only knowledge of the upstream turbulence conditions and the distortion characteristic dimension a of the aerofoil. The identification of this parameter makes it possible to extend the RDT results to model the flow-field alteration in the stagnation region of realistic aerofoil geometries, as suggested by Zamponi et al. [82].

The analysis has been conducted numerically using the grid-aerofoil configuration for the NACA 0012 and NACA 0012-103, replicating the experimental setup from the University of Southampton [34], as explained in Chapter 3.

4.1. ANALYSIS OF THE VELOCITY FIELD

The behaviour of the turbulent field approaching the aerofoil and the extension of the region where distortion occurs can be identified by considering the root-mean-square of the velocity components along the stagnation streamline. Figure 4.1 shows the trends for the streamwise and upwash velocity components u_1 and u_2 for the NACA 0012 and the NACA 0012-103 aerofoils (the spanwise velocity component u_3 is not shown, as its fluctuations remain constant, as also confirmed by Hunt [45]). As the flow approaches the stagnation point, the blockage induced by the body causes the streamwise velocity fluctuations to abruptly decrease and the upwash fluctuations to increase [45]. This distortion mechanism prevails in the case of large-scale turbulence, i.e. when the ratio of the scale of the incoming turbulence to the characteristic dimension of the body, identified in the literature as the aerofoil leading-edge radius (see Chapter 1), is greater than

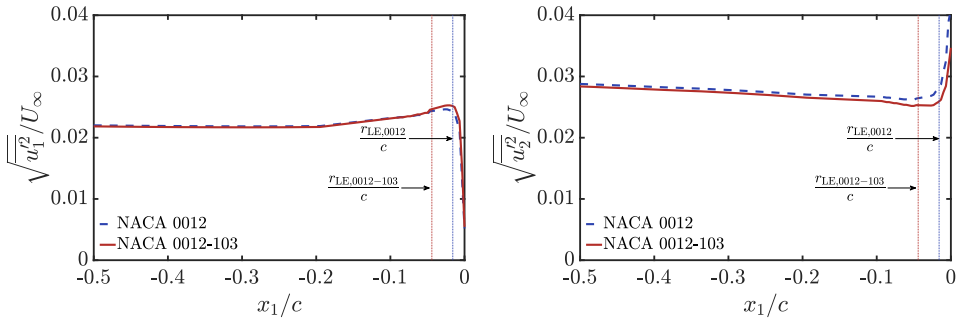

Figure 4.1: Comparison of the root-mean-square of the spanwise-averaged (a) streamwise and (b) upwash velocity components along the stagnation streamline for the two aerofoil configurations. The dashed lines highlight the position corresponding with one leading-edge radius upstream of the leading edge for both cases.

Table 4.1: Sampling locations of the velocity components along the stagnation streamline.

x_1 [m]	x_1/c [−]	$x_1/r_{LE,0012}$ [−]	$x_1/r_{LE,0012-103}$ [−]
-0.75	-0.50	-31.3	-11.4
-0.023	-0.15	-9.38	-3.41
-7.50×10^{-3}	-0.050	-3.13	-1.14
-2.25×10^{-3}	-0.015	-0.94	-0.34
-7.50×10^{-4}	-5.00×10^{-3}	-0.31	-0.11
-2.25×10^{-4}	-1.50×10^{-3}	-0.09	-0.03

0.5 [121]. This is the case for two aerofoils under investigation: L_1/r_{LE} amounts to 2.5 and 1 for the NACA 0012 and NACA 0012-103, respectively.

Notably, the trends of the root-mean-square of the velocity components along the stagnation streamline coincide both far away and in the vicinity of the stagnation point, despite the significant difference between the two leading-edge radii. The variation due to the presence of the body occurs at a distance from the stagnation point that appears unrelated to the leading-edge radius. These findings differ from those of Mish and Devenport [53, 54] and De Santana et al. [50], according to whom turbulence-distortion effects are detected within $1r_{LE}$ from the stagnation point, and challenge the relevance of this geometrical parameter in the alteration of the velocity field.

Further indications about the alteration of the velocity field due to the deformation of the turbulent structures are provided by the velocity spectra at different positions along the stagnation streamline. Figure 4.2 reports the spectra of the streamwise velocity component Θ_{11} at 6 different upstream locations from the stagnation point, listed in the legend of the figure. Data are spatially averaged in the spanwise direction. The turbulence frequency spectra for both aerofoils overlap up to $x_1/c \simeq -5\times10^{-3}$, while, for smaller distances, the effects caused by the presence of the body start to be apparent, i.e. Θ_{11}

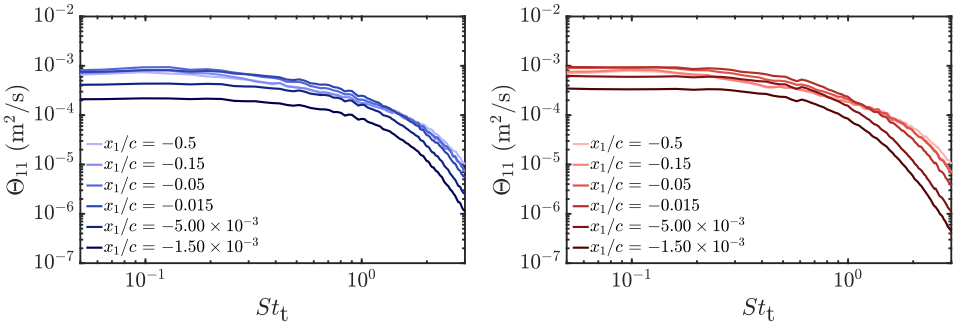

Figure 4.2: Turbulence frequency spectra of the streamwise velocity component along the stagnation streamline at different distances from the aerofoil leading edge for the (a) NACA 0012 and the (b) NACA 0012-103. All the spectra are spatially averaged in the spanwise direction.

4

decreases for all the frequencies.

The same analysis is also repeated for the upwash velocity component, whose turbulence frequency spectra Θ_{22} are reported in Fig. 4.3. Notably, for both aerofoils, the variation of Θ_{22} approaching the stagnation point differs from that of the spectra of the streamwise velocity. In this case, the amplitude of the low-frequency part increases, whereas that for the high-frequency part decreases. These two different trends depend on the ratio L_1/a, which is related to the leading-edge geometry, as explained by the findings of the RDT of Hunt [45]. The crossover frequency between the two trends thus indicates the wavelength at which they balance each other, corresponding to turbulent structures similar in size to the characteristic dimension of the obstacle. This explains why the crossover frequency is observed at $St_t \simeq 1$ in the case of the NACA 0012 (Fig. 4.3a), which features a sharper leading edge, while it is slightly lower, around $St_t \simeq 0.6$, for the more rounded NACA 0012-103 (Fig. 4.3b). Lastly, at locations along the stagnation streamline where turbulence is already distorted, the low-frequency part of the spectrum does not change significantly with the decreasing distance from the surface, while the slope of the high-frequency part keeps increasing.

Since the high-frequency attenuation has been identified as the most significant effect on the aerofoil aerodynamic and acoustic response in the presence of a realistic aerofoil geometry, it is worth focusing on the decay slopes of the spectra at different distances from the leading edge, also depicted in the plots of Fig. 4.3. For large distances from the leading edge, i.e. $|x_1/c| > |-0.015|$, the decay slope is $-5/3$, as foreseen by the linearised theory for the inertial subrange [108]. For the spectrum sampled at $x_1/c = -0.015$, it is still close to $-5/3$ but progressively decreases as the stagnation point is approached. At $x_1/c = -5 \times 10^{-3}$, Θ_{22} is characterised by a decay slope of $-10/3$ for both aerofoils. This value is predicted by the RDT for spectra in the vicinity of the leading edge but for angular positions away from the stagnation streamline [45]. The spectra sampled closest to the body for both aerofoils feature a steeper *exponential* decay slope, for which the following expression derived by Hunt [45] for the normalised Θ_{22} in the

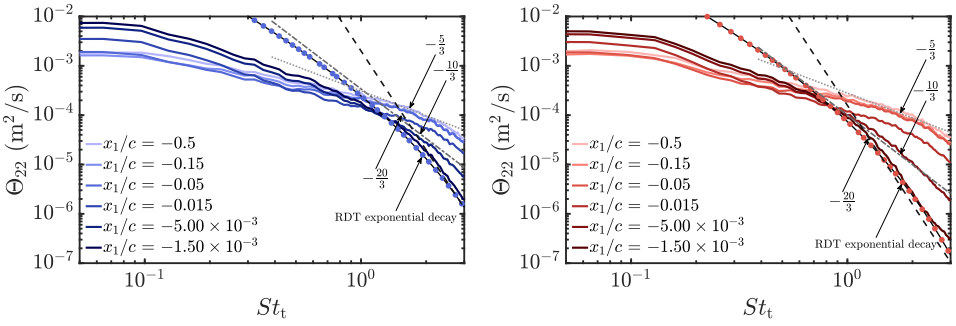

Figure 4.3: Turbulence frequency spectra of the upwash velocity component along the stagnation streamline at different distances from the aerofoil leading edge for the (a) NACA 0012 and the (b) NACA 0012-103. All the spectra are spatially averaged in the spanwise direction.

immediate vicinity of the stagnation point reads

$$\frac{\Theta_{22}}{u'^2 L_1} \simeq G_1 \left(a/L_1\right)^{-\frac{2}{3}} \kappa_1^{-\frac{7}{3}} \mathrm{e}^{-\frac{1}{2}\pi\kappa_1}, \tag{4.1}$$

which corresponds to Eq. (2.95). In this case, the characteristic size of the body a has been set equal to the geometrical parameter $\mathrm{l_{dis}}$, which will be introduced in the subsection Section 4.3. Interestingly, in the frequency range of analysis, this exponential decay can be approximated by a linear decay with a slope of $-20/3$, as shown in Fig. 4.3.

The spanwise evolution of turbulence as the aerofoil leading edge is approached is analysed in terms of spanwise coherence length $l_3(\omega)$ using Eq. (2.15), which is linked to the inflow-turbulence noise produced by the aerofoil, as shown in Eq. (2.13). The coherence of the upwash velocity component in the spanwise direction is calculated at the locations listed in the legend of the figure along the stagnation streamline. Results, which are reported in Fig. 4.4, show that the $l_3(\omega)$ values in the low-frequency range increase as the stagnation point is approached, whereas the high-frequency range is not affected by the turbulence distortion and does not vary with the increasing proximity to the leading edge.

4.2. TURBULENCE-DISTORTION EFFECTS ON UNSTEADY SURFACE PRESSURE

Relevant indications about the noise-generation mechanism and effect of aerofoil geometry can be inferred by looking at the pressure distribution on the aerofoil surface. The root-mean-square of the spanwise-averaged surface-pressure fluctuations, which are normalised by the free-stream dynamic pressure q_∞, is shown for both aerofoils in Fig. 4.5. The distributions, reported as a function of the curvilinear abscissa s, are compared to the spatial derivative with respect to s of the time-averaged pressure coefficient C_p along the surface. For both aerofoils, the position along the surface at which the

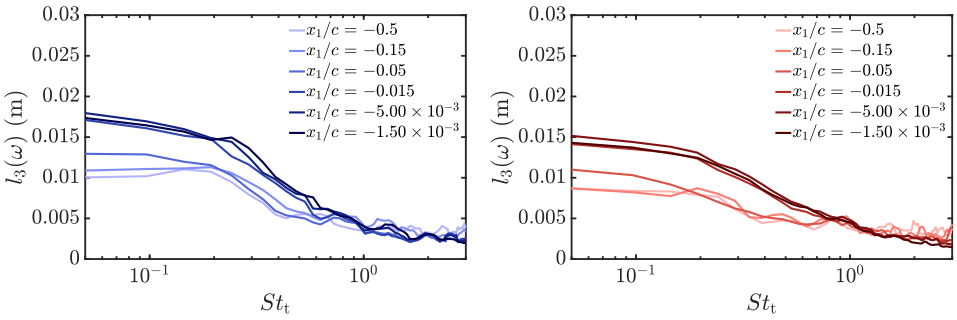

Figure 4.4: Spanwise coherence length of the upwash velocity component along the stagnation streamline at different distances from the aerofoil leading edge for the (a) NACA 0012 and the (b) NACA 0012-103.

pressure fluctuation is maximum occurs downstream of the stagnation point, in agreement with the results of Zamponi et al. [122]. More precisely, the point of maximum surface-pressure fluctuations is slightly downstream of the position where the pressure gradient peaks. This result suggests a direct relation between the pressure gradient along the aerofoil, which is associated with the mean flow around the body, and the spatial distribution of the surface-pressure fluctuations, which are connected with the noise-generation efficiency of the body [123].

The distributions of these quantities are also compared with the spatial derivative of the non-dimensional curvature C_s with respect to the curvilinear abscissa s (Figs. 4.5c and 4.5d for the NACA 0012 and NACA 0012-103, respectively). As expected, the pressure gradient is maximum where the curvature changes more abruptly, i.e. at the position where the derivative of the curvature reaches its utmost. This observation identifies in the *variation* of curvature, which is related to the sharpness of the leading edge, a relevant geometrical feature for noise-generation efficiency, as also shown by Lockard and Morris [29], Oerlemans [32] and Moriarty et al. [124]. Indeed, even though the far-field noise spectra for the two aerofoils are comparable (see Fig. 3.6), a noise reduction of around 5 dB occurs for the NACA 0012-103, which is characterised by a more rounded leading edge, for $St_t > 0.6$. This is attributed to the lower peak (around 80 %) of the surface-pressure fluctuations with respect to that induced on the NACA 0012 (see Fig. 4.5), confirming that the shape of the leading edge has an impact on the sound-radiation efficiency of the aerofoil even when the thickness is kept constant, in agreement with Gill et al. [36]. In addition, the pressure-gradient intensity, associated with the variation of curvature in the front part of the aerofoil, seems to affect the distortion of the turbulent structures as they accelerate along the surface, as also concluded by Gershfeld [39].

The impact of the alteration of the velocity field due to turbulence distortion on the noise generation is investigated by analysing the frequency spectra of the pressure fluctuations at different positions along the surface of the aerofoils and averaged in the spanwise direction (Fig. 4.6). The five sampling locations are set as multiples of the curvilin-

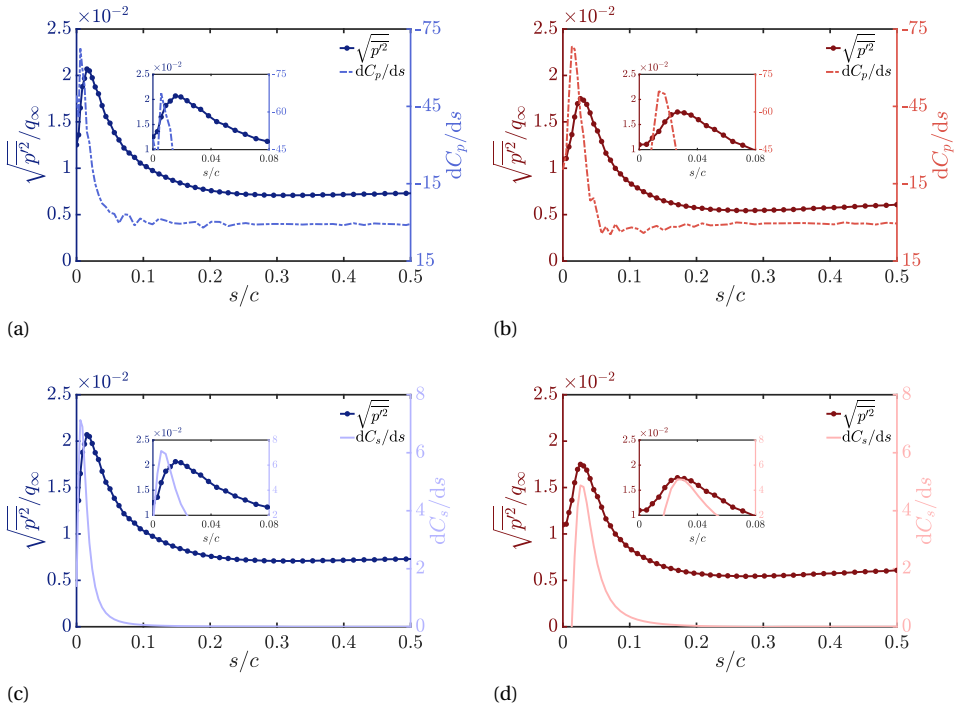

Figure 4.5: Analysis of the surface pressure. The root-mean-square of the surface-pressure fluctuations is compared with the time-averaged pressure gradient and the derivative of the curvature of the leading edge of the aerofoil for the (a)- (c) NACA 0012 and the (b)- (d) NACA 0012-103.

ear abscissa of the point of maximum pressure fluctuations with respect to the stagnation point, defined as l_{dis}. The purpose is to analyse the variation of surface-pressure characteristics in the surroundings of the point where the noise source is maximum. For both NACA 0012 and NACA 0012-103, the surface-pressure spectra in the vicinity of the leading edge feature an exponential decay slope in the high-frequency range. Such decay is caused by the pile-up of the vortical structures on the stagnation point, which leads to a more effective cancellation of the pressures induced by the eddies with respect to other positions around the body [125]. At the stagnation point and in the high-wavenumber asymptotic limit, which describes the effects on the surface pressure caused by the distortion of small-scale structures, this physical mechanism can be modelled by [125]

$$\Theta_{pp} \propto (a/L_1)^{-\frac{2}{3}} (L_1\kappa_1/a)^{-\frac{7}{3}} \mathrm{e}^{-\pi\kappa_1 Q}. \tag{4.2}$$

Here, Q is a factor derived from the expansion of Lighthill's drift function [83] computed on the surface boundary, which the linearised theory estimates to be $O(1)$. This parameter has been determined by matching the exponent to that of the high-frequency exponential decay of the upwash velocity spectrum identified by Hunt [45], resulting in $Q = 0.6$ for both aerofoils. Under this assumption, Fig. 4.6 shows that the analytical

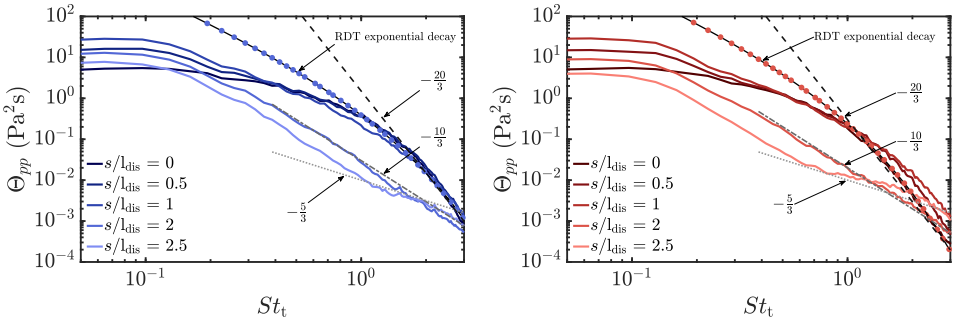

Figure 4.6: Surface-pressure spectra at different positions along the aerofoil surface for the (a) NACA 0012 and the (b) NACA 0012-103. All the spectra are spatially averaged in the spanwise direction.

4

calculations correctly approximate the surface-pressure spectra sampled at the closest positions to the stagnation point for both aerofoils, proving that, in the vicinity of the leading edge, the unsteady surface pressure in the high-frequency range decays as the upwash velocity. Moreover, similarly to the velocity field, the exponential roll-off characterizing the high-frequency range of the surface-pressure spectrum is very close to a linear decay with a slope of $-20/3$. This result agrees with the experimental findings of Bowen et al. [37], who showed that the high-frequency slope of the surface-pressure PSD in the vicinity of the stagnation point of a NACA 0012 scales approximately with the 7th power of the frequency. As the surface-pressure spectra are sampled more downstream, a significant reduction in the absolute value of the decay slope and amplitudes at high frequencies is observed, whereas the levels in the low-frequency range increase up to the location of maximum surface-pressure fluctuations and then decrease.

The effects of the distorted velocity field on the surface-pressure distribution are now studied in terms of coherence $\gamma^2_{u_2' p'}$ between the surface pressure and the upwash velocity sampled at two different locations along the stagnation streamline using Eq. (2.16). Figure 4.7 shows the $\gamma^2_{u_2' p'}$ distribution along the aerofoil using as reference points $x_1/c = -0.5$ and $x_1/c = -1.5 \times 10^{-3}$, i.e. the furthest and closest positions with respect to the leading edge among those previously considered. Higher coherence between the surface pressure on the leading edge and the upwash velocity component is obtained when the velocity is taken very closely to the stagnation point, particularly in the high-frequency range. In agreement with Bowen et al. [37] and Zamponi et al. [122], the highest $\gamma^2_{u_2' p'}$ values are found slightly downstream of the stagnation point, specifically at the location where the root-mean-square of the surface-pressure fluctuations is maximum, i.e. at the position where the curvature changes more abruptly. The high coherence between the surface pressures and upwash velocity fluctuations in the vicinity of the stagnation point confirms that sound-production mechanisms are affected by the alteration experienced by the velocity field due to the distortion of the turbulence structures. Consequently, the investigation of the surface pressure can provide meaningful insight into the deforma-

tion mechanisms experienced by the incoming turbulence, as will be demonstrated in the next subsection.

4.3. DESCRIPTION OF TURBULENCE-DISTORTION MECHANISMS AND INFLUENCE OF AEROFOIL GEOMETRY

The turbulence-distortion mechanism is now further elucidated in view of the results of the analyses of the surface pressure and the velocity field. As shown in Section 4.1, the frequencies marking the crossover between the large-scale distortion behaviour (low-frequency part of the spectra) and the small-scale one (high-frequency part of the spectra) differ for the two aerofoils. This finding hints at an effect of the leading-edge geometry on the distortion mechanisms of the incoming turbulent structures, which are dictated by the conditions $L_1/a \gg 1$ and $L_1/a \ll 1$.

What remains to be elucidated yet is which geometrical parameter a determines these different behaviours. The evolution of the surface-pressure fluctuations provides a valuable indication for it. Indeed, if turbulence distortion, as well as noise generation, is affected by the flow accelerating along the aerofoil surface, it is reasonable to assume that the relative size of the eddies with respect to the space available for accelerating is also relevant in determining the deformation mechanism the eddies will experience in the interaction with the leading edge. As previously mentioned, this distance l_{dis} can be estimated from the geometrical characteristics of the aerofoil, being this parameter comparable to the arc length going from the stagnation point to the position of maximum variation of curvature. This location also coincides with the point where the aerofoil geometry at the leading edge starts diverging from the curve of the osculating circle, i.e. $l_{dis} = \theta_{dis} r_{LE}$, with θ_{dis} being the angular position along the leading-edge circle associated with the point of the maximum derivative of the aerofoil curvature (Fig. 4.8).

By employing a Strouhal number $St_{l_{dis}}$ defined with this quantity, the impact of l_{dis} on the distortion of the incoming turbulence structures can be assessed. The turbulent spectra of the upwash velocity component at three different distances from the stagnation point are shown in Fig. 4.9 for both aerofoils. Using $St_{l_{dis}}$, the spectra collapse for all the considered distances, suggesting that the *distortion length* l_{dis} is the geometrical parameter to consider to evaluate the turbulence-distortion effects and legitimate the extension of the RDT results to aerofoil applications. This is also a further indication that the leading-edge radius *indirectly* plays a role in the identification of the turbulence-distortion mechanisms via the length of the arc from the stagnation point to the position of maximum curvature. Interestingly, in the case of the NACA 0012, the value of l_{dis} almost coincides with the leading-edge radius, supporting the literature results outlined in Chapter 1 that considered r_{LE} as the characteristic dimension of the aerofoil noise dictating the turbulence distortion.

4.4. TURBULENCE-DISTORTION EFFECTS ON LEADING-EDGE NOISE PREDICTION

The results of the analysis of the velocity field in the vicinity of the leading edge and the unsteady surface pressure on the aerofoil allow the assessment of turbulence-distortion

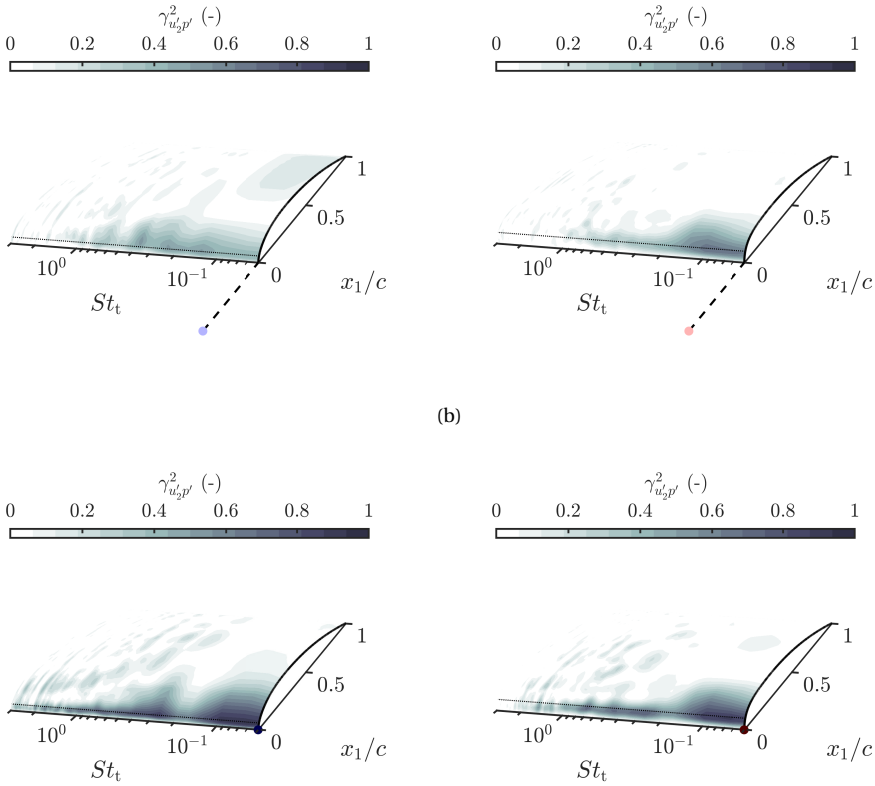

Figure 4.7: Coherence between the surface pressure and the upwash velocity sampled at (a) $x_1/c = -0.5$ and (c) $x_1/c = -1.5 \times 10^{-3}$ for the NACA 0012 and at (b) $x_1/c = -0.5$ and (d) $x_1/c = -1.5 \times 10^{-3}$ for the NACA 0012-103. In the figures, the position where the upwash velocity is sampled is shown with a dot, while the dotted line depicts the position along the aerofoil where surface-pressure fluctuations peak.

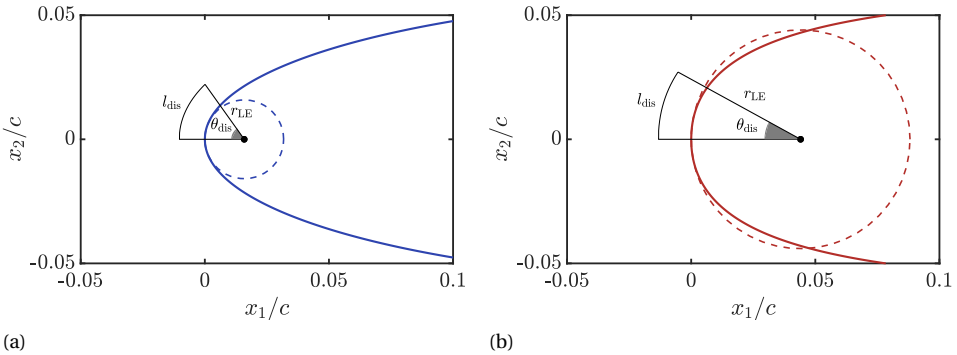

Figure 4.8: Geometry of the leading edge of the (a) NACA 0012 and the (b) NACA 0012-103 with highlighted the parameter l_{dis}, geometrically comparable to the distance along the aerofoil surface between the stagnation point and the position of maximum curvature variation.

effects in low-fidelity models. A first attempt to account for these effects in Amiet's model is carried out by using Eq. (2.10), which relates the far-field noise to the cross-spectral density of the surface pressure on the aerofoil by means of Curle's analogy. This has been solved by using an in-house routine implemented in MATLAB by MathWorks. The outcome of this implementation of Amiet's model compared to the noise prediction obtained with the solid formulation of FWH analogy is shown in Fig. 4.10 in terms of SPL, whose calculation considers the observer above the leading edge ($\theta = \pi/2$) at a distance of R = 1.2 m. The noise prediction obtained with Amiet's model coincides with the results of the FWH analogy, correctly estimating the noise levels and the decay slope in the range of interest, up to the frequency associated with the sampling spatial resolution of the surface pressures in Amiet's model. Indeed, this resolution was kept significantly lower than that employed by PowerFLOW for the FWH analogy due to the excessive computational cost required by solving Eq. (2.10) in MATLAB. This results in an insufficient characterization of destructive interference effects, which explains the discrepancy observed at very high frequencies.

The comparison, on the one hand, shows that the analytical model of Amiet is able to accurately predict inflow-turbulence noise also for the case of aerofoils with non-negligible thickness but, on the other hand, is not particularly interesting from an applicative point of view since its implementation requires the knowledge of the surface pressure field on the whole aerofoil. The advantage of using a low-fidelity method to decrease the computational cost would be, hence, lost.

The most relevant and practically useful formulation of Amiet's model is that of Eq. (2.11), which allows the calculation of the far-field noise starting from the characteristics of the incoming turbulence by using a transfer function to model the response of the aerofoil to the perturbation. Given the results obtained in the previous section regarding the modification of the velocity field in the vicinity of the surface, a possible approach to account for the turbulence-distortion effects in the noise prediction by means of Amiet's model is to consider turbulence characteristics in the vicinity of the stagnation point. The simplified version of Eq. (2.13) is employed to consider the turbulence spectrum along the

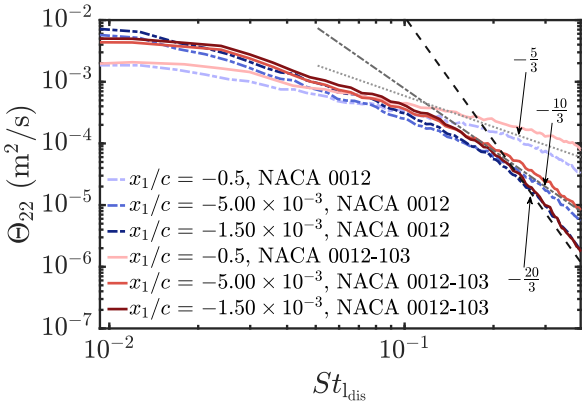

Figure 4.9: Comparison of the upwash velocity component spectra for the two aerofoils as a function of the Strouhal number defined using the quantity l_{dis}, which represents the arc length along the surface for which the aerofoil is approximated as a circle.

stagnation streamline as input. In particular, the $\Theta_{22}(\omega)$ acquired in the closest position to the aerofoil leading edge ($x_1/c = -1.5\times10^{-3}$) is used in the equation. The spanwise coherence length $l_3(\omega)$ is calculated at the same position. The noise prediction obtained using this low-fidelity method is compared to the results of the FWH analogy in terms of SPL and PWL. For the calculation of the SPL, the observer location has been considered to be right above the leading edge ($\theta = \pi/2$) in the midspan plan, at a distance of R = 1.2 m.

The comparison in SPL between the analytical prediction and the FWH analogy is reported in Fig. 4.11, while Fig. 4.12 shows the corresponding PWL. Amiet's model using as input the turbulence spectrum sampled 1.5×10^{-3} c upstream of the leading edge, indicated with $\Theta_{22,dis}$, is compared with the prediction using a spectrum sampled far upstream as input, i.e. at 0.5 c from the stagnation point, expressed as $\Theta_{22,ups}$. In agreement with the literature findings, the canonical application of Amiet's model, i.e. considering a spectrum representing the undistorted conditions, correctly estimates the noise level in the low-frequency range up to $St_t = 0.35$, while overpredicts it for higher frequencies, for which the decay slope of the spectrum is not correctly calculated. Conversely, the prediction of Amiet's model using the distorted spectrum features the same trend as that computed with the FWH analogy, including the correct decay slope in the high-frequency range. A general overestimation in the entire frequency range is obtained, though. This overestimation is traced back to the results of the velocity-field analysis in the stagnation region, where the upwash velocity spectrum increases in the low-frequency range and decreases in the high-frequency one, and depends on the fact that the aeroacoustic transfer function in Eq. (2.45) and Eq. (2.46) have not been modified accounting for the distortion effects. Given the crucial role played by the transfer function in the quantitative prediction of the emitted noise levels, Section 4.5 will be dedicated to investigating these effects.

The consequences of incorporating turbulence-distortion effects into Amiet's model are now evaluated by varying the sampling position of the turbulence spectrum across

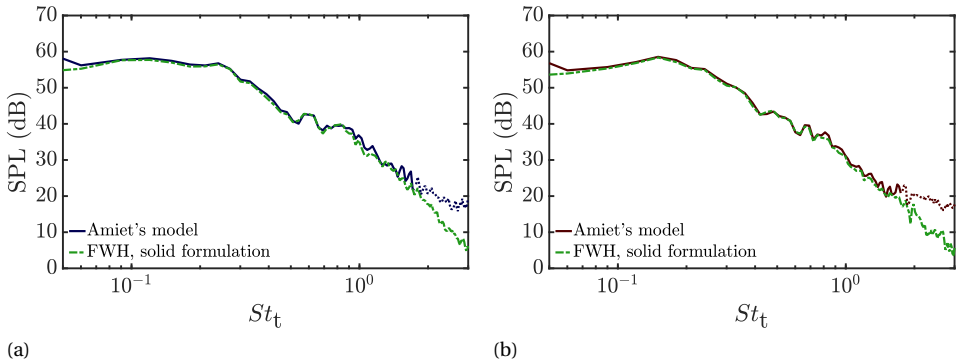

Figure 4.10: Sound pressure level in the far-field calculated for an observer placed at R = 1.2 m and $\theta = \pi/2$, with the angular position computed with respect to the downstream direction, for the (a) NACA 0012 and (b) NACA 0012-103. Amiet's implementation using surface pressure cross-PSD as input is compared to the calculation provided by the FWH analogy. The reference pressure for the SPL calculation is 2×10^{-5} Pa.

the entire stagnation region. The analysis involves calculating the difference in the overall sound pressure level ΔOASPL between Amiet's model using the distorted spectrum as input and the results provided by the FWH analogy. The difference between these two noise predictions has been calculated in the frequency range in which leading-edge noise prevails, i.e. $0.15 < St_t < 1.5$.

It is useful to combine such analysis with the assessment of the difference in decay slope in the high-frequency range $|\Delta m|$ between the spectrum obtained with the FWH analogy and Amiet's model with different positions where Θ_{22} is sampled. The decay slopes of the sound power levels in the range going from $St_t = 0.4$ to $St_t = 2$ are taken as reference. Figure 4.13 reports the contour plot of both these quantities for the two aerofoils. On the one hand, the results for the ΔOASPL in Fig. 4.13a and 4.13b demonstrate that a substantial increase in terms of noise levels up to 6 dB in comparison with the numerical simulations is obtained by sampling Θ_{22} closer to the stagnation point. On the other hand, the difference in decay slope between Amiet's model and FWH shown in Figs. 4.13c and 4.13d indicates that a significant improvement is achieved in the high-frequency range with respect to the canonical application of Amiet's model, with Δm tending to zero when the turbulence spectrum is sampled at the aerofoil stagnation region.

4.5. AEROACOUSTIC TRANSFER FUNCTION MODIFICATION FOR DISTORTED-TURBULENCE INPUT

In view of the above, the effects of turbulence distortion on the velocity field must be taken into account in the physical modelling of the noise-generation mechanism at the basis of low-fidelity noise-prediction methods. This can be achieved by considering the turbulence spectrum in the immediate vicinity of the stagnation point to capture the characteristics of the unsteady loading on the leading edge. Indeed, the closer the

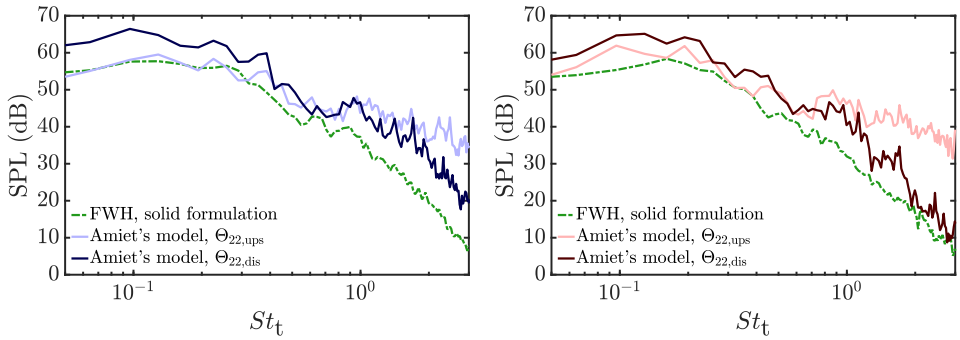

Figure 4.11: Sound pressure level in the far-field calculated for an observer placed at R = 1.2 m and $\theta = \pi/2$, with the angular position computed with respect to the downstream direction, for the (a) NACA 0012 and the (b) NACA 0012-103. Amiet's implementation using spectra sampled far upstream $\Theta_{22,\text{ups}}$ and in the distorted region of the flow field $\Theta_{22,\text{dis}}$ is compared to the calculation provided by the FWH analogy. The reference pressure used to calculate the SPL is 2×10^{-5} Pa.

sampling location is, the more accurate the prediction of the decay slope will be. The constant noise overestimation across the entire frequency range, however, indicates that the effects of turbulence distortion have not been fully accounted for. The comparison with the accurate prediction obtained implementing Eq. (2.10), which does not require a transfer function to relate the unsteady loading distribution to the incoming turbulence characteristics, suggests that potential distortion effects on the aerofoil response must be assessed.

As outlined in Subsection 2.1.1, Amiet's model relies upon the relation between the pressure distribution on the aerofoil surface (specifically, a flat plate) and the upstream incident gust that induces the unsteady loading. The analytical expression for this relation (Eq. (2.3)) is obtained in the assumption of monochromatic sinusoidal gust with amplitude $u_{2,0}$ (Eq. (2.2)), which introduces the transfer function $g(x_1, K_1, k_3)$. Employing a transfer function based on the response of a flat plate is equivalent to following a *quasi-steady* theory, which is based on the hypothesis that the only effect of turbulence added to the incoming flow is a small change in the angle of incidence and magnitude of the upstream velocity [125]. This corresponds to assuming the surface pressure on the flat plate to be induced by undistorted large-scale turbulence. Nevertheless, it has been shown in Section 4.1 that, for both aerofoils, the realistic geometry effects entail a variation of the turbulent velocity as the stagnation point is approached due to the blockage caused by the surface (see Fig. 4.1). This variation in the energy content, which can also be interpreted as an increase in the perturbation amplitude, supports the increase in the low-frequency range observed for upwash-velocity spectra sampled in the stagnation region, which is related to the distortion of large-scale turbulent structures. However, the original formulation of the transfer function does not encompass these effects, explaining the observed overestimation once the altered turbulence spectrum is used in the prediction. This can be shown by applying the same analytical procedure

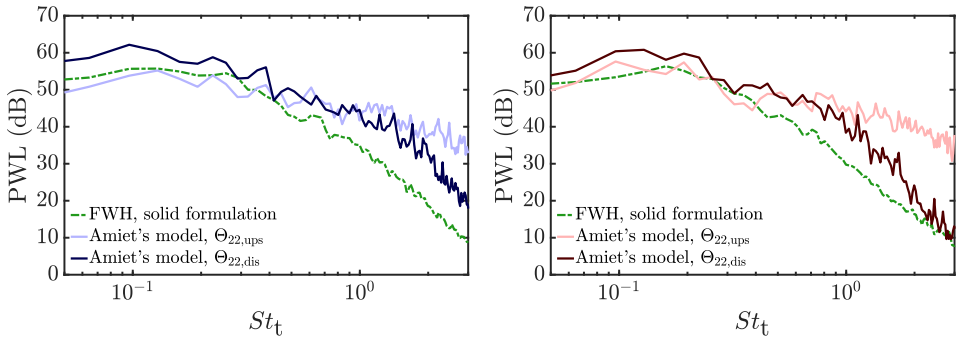

Figure 4.12: Sound power level in the far-field for the (a) NACA 0012 and the (b) NACA 0012-103. Amiet's implementation using spectra sampled far upstream $\Theta_{22,\text{ups}}$ and in the distorted region of the flow field $\Theta_{22,\text{dis}}$ is compared to the calculation provided by the FWH analogy. The reference power used to calculate the PWL is 10^{-12} W.

followed by Amiet but considering a sinusoidal gust $u_{2,\text{dis}}(x_1, x_3)$ with amplitude scaled by a factor λ_{dis} with respect to the upstream undistorted one v_0 as input:

$$u_{2,\text{dis}}(x_1, x_3) = \left(\lambda_{\text{dis}} u_{2,0}\right) \mathrm{e}^{\mathrm{i}[K_1(U_\infty t - x_1) - k_3 x_3]} = \lambda_{\text{dis}} u_2(x_1, x_3). \tag{4.3}$$

In the framework of the quasi-steady theory, this distorted gust is considered to be mathematically related to the altered turbulence spectrum that accounts for distortion effects.

Note that the aeroacoustic transfer function terms are not formally affected by the variation of the gust amplitude. Indeed, as detailed in Subsection 2.1.3, $u_2(x_1, x_3)$ cancels out in the calculation of leading-edge term $\mathscr{L}_1$ (Eq. (2.45)) and the trailing-edge one $\mathscr{L}_2$ (Eq. (2.46)) by substituting the pressure terms induced by the sinusoidal perturbation (Eq. (2.39) and Eq. (2.40)) in the expression for $g(x_1, K_1, k_3)$ (Eq. (2.44)). This indicates that the intensity of the aerodynamic and acoustic response of the aerofoil depends on the gust amplitude in Eq. (2.3) and the turbulence spectrum once the formulation is expressed in statistical quantities. This passage from time and space-dependant expressions to statistical operators is worth a more detailed analysis. The cross-PSD of the surface pressure in Eq. (2.7) is indeed retrieved from Eq. (2.6) through

$$S_{QQ}\left(x_1, x_1', x_3, x_3', \omega\right) = \lim_{T\to\infty} \frac{\pi}{T} \langle \Delta\hat{p}(x_1, x_3, \omega)\, \Delta\hat{p}^{\dagger}\left(x_1', x_3', \omega\right)\rangle, \tag{4.4}$$

with $\langle\cdot\rangle$ indicating the expected-value operator and the superscript † identifying the complex conjugate. At this point, once Eq. (2.6) with the distorted gust as input is substituted into Eq. (4.4), the only non-deterministic quantity is the Fourier transform of the gust $\hat{u}_{2,\text{R,dis}}(K_1, k_3)$. Taking all the other terms out of the expected value yields

$$\langle \hat{u}_{2,\text{R,dis}}(K_1, k_3)\, \hat{u}^{\dagger}_{2,\text{R,dis}}(K_1, k_3)\rangle = \frac{R}{\pi} \Phi_{22,\text{dis}}(K_1, k_3), \tag{4.5}$$

where the distorted turbulence spectrum used as input in the model appears. Considering Eq. (4.3) and the linearity of the expected-value operator, which allows the amplitude-

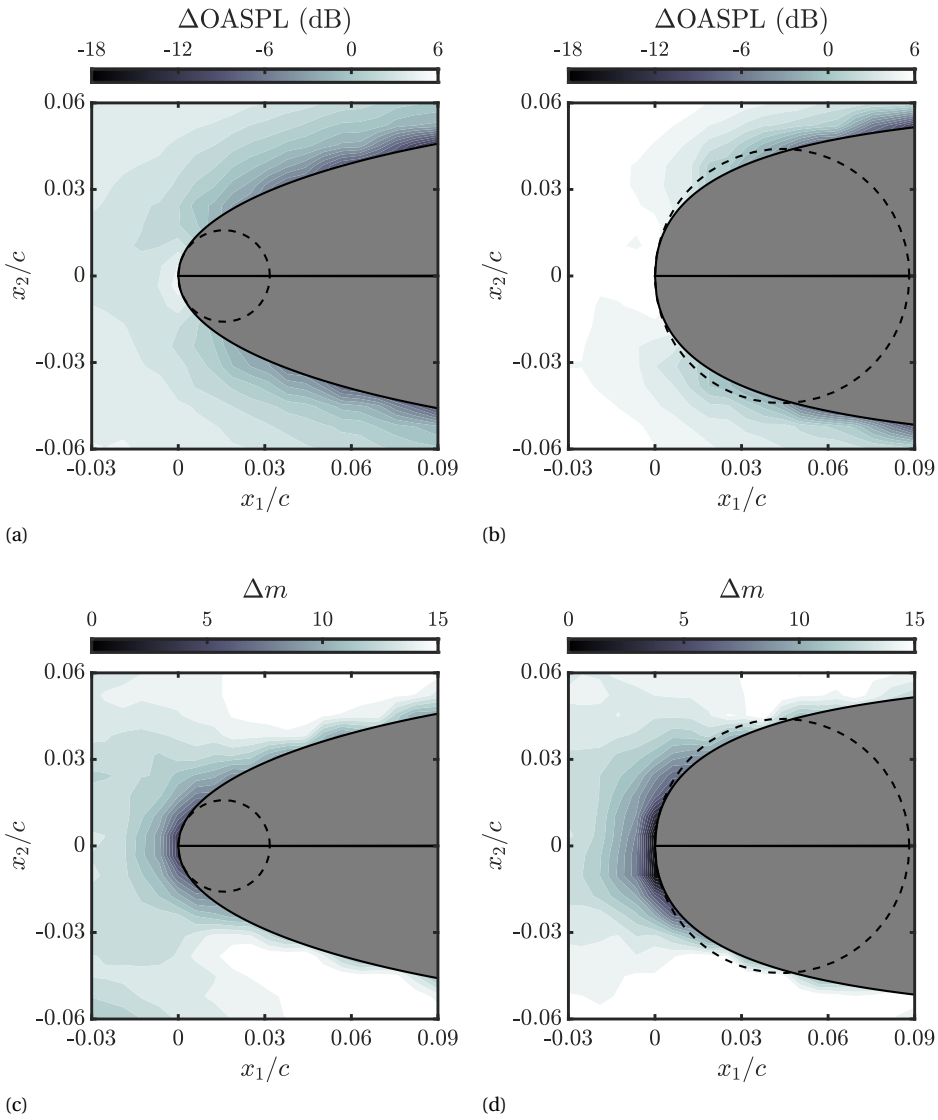

Figure 4.13: Difference in overall sound pressure level ΔOASPL and in slope Δm of the PWL between the noise prediction from the FWH analogy and from Amiet's model using different sampling positions for the turbulence spectrum. These quantities are shown respectively in (a) and (c) for NACA 0012 and in (b) and in (d) for the NACA 0012-103. For the ΔOASPL, the observer is placed at R = 1.2 m and $\theta = \pi/2$, with the angular position computed with respect to the downstream direction. The slope is calculated in the range $St_t = 0.4 - 2$.

variation factor λ_{dis} to be brought outside, it follows that

$$\lambda_{\text{dis}}^2 \Phi_{22}(K_1, k_3) = \Phi_{22,\text{dis}}(K_1, k_3), \tag{4.6}$$

the expected value of the magnitude squared of $\hat{u}_{2,R}(K_1, k_3)$ being the upstream turbulence spectrum $\Phi_{22}(K_1, k_y)$. This equation indicates that substituting the undistorted turbulence spectrum with an altered one to account for the effects of turbulence distortion introduces an increase in the energy content of the turbulence term in input. This variation is due to the distortion of the energy-containing scales in the stagnation region and is not encompassed in the original formulation of Amiet's model, which indeed overestimates the radiated noise by a constant offset across the entire frequency range compared to FWH. A modification of the turbulence term without accounting for this mechanism thus yields a noise prediction corresponding to the interaction of an undistorted perturbation featuring increased amplitude with the aerodynamic surface.

The validity of this discussion also holds for the simplified formulation of Amiet's model (Eq. (2.13)), implemented in the present study, where $\Theta_{22}(\omega)$ and $l_3(\omega)$ are used in place of the wavenumber spectrum. Indeed, in the case of large aerofoil spans, it is shown that

$$\Psi_{22}(K_1, 0) = \frac{U_\infty}{\pi} \Theta_{22}(\omega)\, l_3(\omega) \tag{4.7}$$

since the dependency on k_3 of both the aeroacoustic transfer function and the wavenumber upwash-velocity spectrum becomes negligible.

Amiet's analytical procedure can be resumed from Eq. (4.5), which leads to Eq. (2.7). This relates the cross-PSD of the surface pressure $S_{QQ}(x_1, x_1', \eta, \omega)$ to the wavenumber spectrum $\Phi_{22}(K_1, k_3)$ via the transfer function $g(x_1, K_1, k_3)$. Taking into account Eq. (4.6) and 4.7, through Eq. (2.10) and 2.11, the following formulation for a distortion-corrected equation of Amiet's model is derived:

$$S_{pp}(x_1, x_2, 0, \omega) = \left(\frac{\omega y \rho_\infty c M_\infty}{2\sigma_0^2} \right)^2 \frac{\mathrm{L}}{2} |\mathscr{L}_{\text{dis}}(\boldsymbol{x}, K_1, 0)|^2 \Theta_{22,\text{dis}}(\omega)\, l_3(\omega), \tag{4.8}$$

with $\mathscr{L}_{\text{dis}}$ indicating the corrected aeroacoustic transfer function defined to account for the increase of the gust amplitude due to the turbulence distortion at the stagnation region, whose expression is

$$\begin{aligned} \mathscr{L}_{\text{dis}}(x_1, K_1, k_3) &= \frac{1}{\lambda_{\text{dis}}} \mathscr{L}(x_1, K_1, k_3) = \\ &= \int_{-L/2}^{L/2} \frac{1}{\lambda_{\text{dis}}} g(x_{1,0}, K_1, k_3)\, \mathrm{e}^{-\mathrm{i}\omega x_{1,0}(M_\infty - x_1/\sigma)/c_\infty \beta^2} \mathrm{d}x_0. \end{aligned} \tag{4.9}$$

Indeed, considering the factor λ_{dis} as a scaling coefficient for the aeroacoustic transfer function is motivated by the fact that the pressure jump on the aerofoil surface, which produces the noise radiation, is induced by the altered velocity field in the stagnation region, as shown in Section 4.2. Therefore, the aerodynamic and acoustic response of the aerofoil must be scaled in order to correctly encompass the flow-field alteration caused by the aerofoil geometry. This strategy, which allows the gust amplitude in $g(x_1, K_1, k_3)$ to

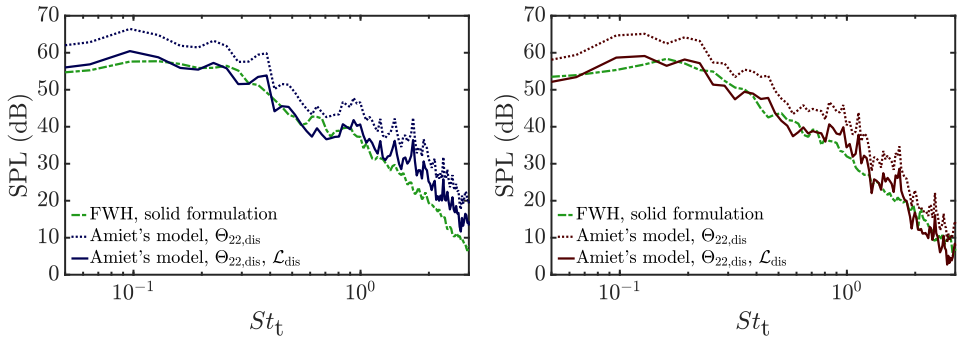

Figure 4.14: Sound pressure level in the far-field calculated for an observer placed at R = 1.2 m and $\theta = \pi/2$, with the angular position computed with respect to the downstream direction, for the (a) NACA 0012 and the (b) NACA 0012-103. Amiet's model implementations using spectra sampled in the distorted region of the flow field $\Theta_{22,\text{dis}}$ and the one also with the corrected transfer function $\mathcal{L}_{\text{dis}}$ are compared to the calculation provided by the FWH analogy. The reference pressure used to calculate the SPL is 2×10^{-5} Pa.

be scaled, is consistent with the approach proposed by Christophe [49] and De Santana et al. [50], which is based on the modification of the von Kármán model considering a different decay slope of the upwash velocity spectrum and imposing the conservation of the turbulent kinetic energy.

A straightforward approach to model the energy variation with respect to upstream conditions, owing to the same assumption of large-scale turbulence interacting with the aerodynamic body, is by using the RDT analytical expressions for the asymptotic case $L_1/a \gg 1$ to evaluate the evolution of the root-mean-square of the velocity components along the stagnation streamline. The outcome of this quasi-steady calculation reads [45]

$$\sqrt{\overline{u_1'^2}} = \sqrt{\overline{u_{1,\infty}'^2}}\left(1 - \frac{1}{\left(1 - \frac{x_1}{a}\right)^2}\right); \tag{4.10}$$

$$\sqrt{\overline{u_2'^2}} = \sqrt{\overline{u_{2,\infty}^2}}\left(1 + \frac{1}{\left(1 - \frac{x_1}{a}\right)^2}\right). \tag{4.11}$$

The trends of the two velocity components as a function of the characteristic dimension of the body are valid close to the stagnation point [120]. While the asymptotic analysis confirms the results discussed in Fig. 4.1, the root-mean-square of the undistorted upwash component near the body surface is amplified by a factor 2. Consequently, since the upwash velocity spectrum is sampled in the immediate vicinity of the surface, the amplitude-scaling factor λ_{dis} is taken equal to 2.

It is important to stress that, in the case of thicker aerodynamic surfaces, the quasi-steady approach may no longer be representative of the acoustic response of the aerofoil, leading to deviations of the gust-amplitude variation along the stagnation streamline from the large-scale behaviour predicted by the linearised theory.

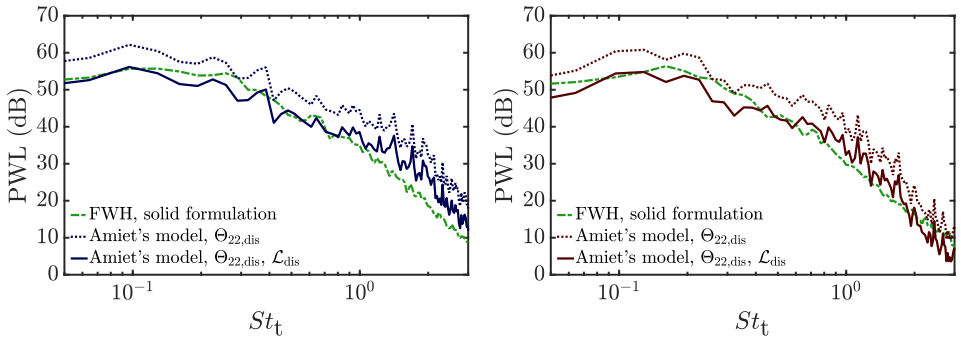

Figure 4.15: Sound power level in the far-field for the (a) NACA 0012 and the (b) NACA 0012-103. Amiet's model implementations using spectra sampled in the distorted region of the flow field $\Theta_{22,\text{dis}}$ and the one also with the corrected transfer function $\mathscr{L}_{\text{dis}}$ are compared to the calculation provided by the FWH analogy. The reference power used to calculate the PWL is 10^{-12} W.

4.6. DISTORTION-CORRECTED LEADING-EDGE NOISE PREDICTION

As explained in Section 4.1, the assumption of large-scale turbulence can be considered valid for the two aerofoils under investigation. This means that the corrected expression of the model of Eq. (4.8), using the altered aeroacoustic transfer function $\mathscr{L}_{\text{dis}}$ and the turbulence spectrum sampled as close as possible to the leading edge Θ_{dis}, can be applied and used to draw a comparison with the results of the FWH analogy.

The outcomes of the above analysis are shown in terms of SPL, PWL and far-field noise directivity patterns in Figs. 4.14, 4.15, and 4.16, respectively. For the latter investigation, two different frequency ranges of integration are selected: a low-frequency range $St_t = [0.15, 0.35]$ and a high-frequency one $St_t = [0.35, 1.5]$, i.e. the part of the spectrum where the noise levels are correctly estimated by the canonical application of Amiet's model and that where they are overestimated because of the wrong prediction of the spectrum decay slope.

The results of the SPL and the PWL show that this distortion-corrected formulation of Amiet's model leads to an overall good agreement with the noise prediction yielded by the FWH analogy in terms of high-frequency decay slope and noise levels, demonstrating that the proposed approach correctly encompasses the physical mechanisms that are responsible for leading-edge noise generation. The necessity to account for a gust amplitude correction in the aeroacoustic transfer function is also confirmed by the directivity patterns. Indeed, in the low-frequency range for both aerofoils (Figs. 4.16a and 4.16b), a constant overestimation is found for the application of Amiet's model using only the spectrum sampled close to the stagnation point as input. Also in the high-frequency range, a similar trend is found for the NACA 0012 and NACA 0012-103, as reported in Figs. 4.16c and 4.16d, respectively. Once the correction of the transfer function is included in the formulation, a good agreement is obtained with the numerical

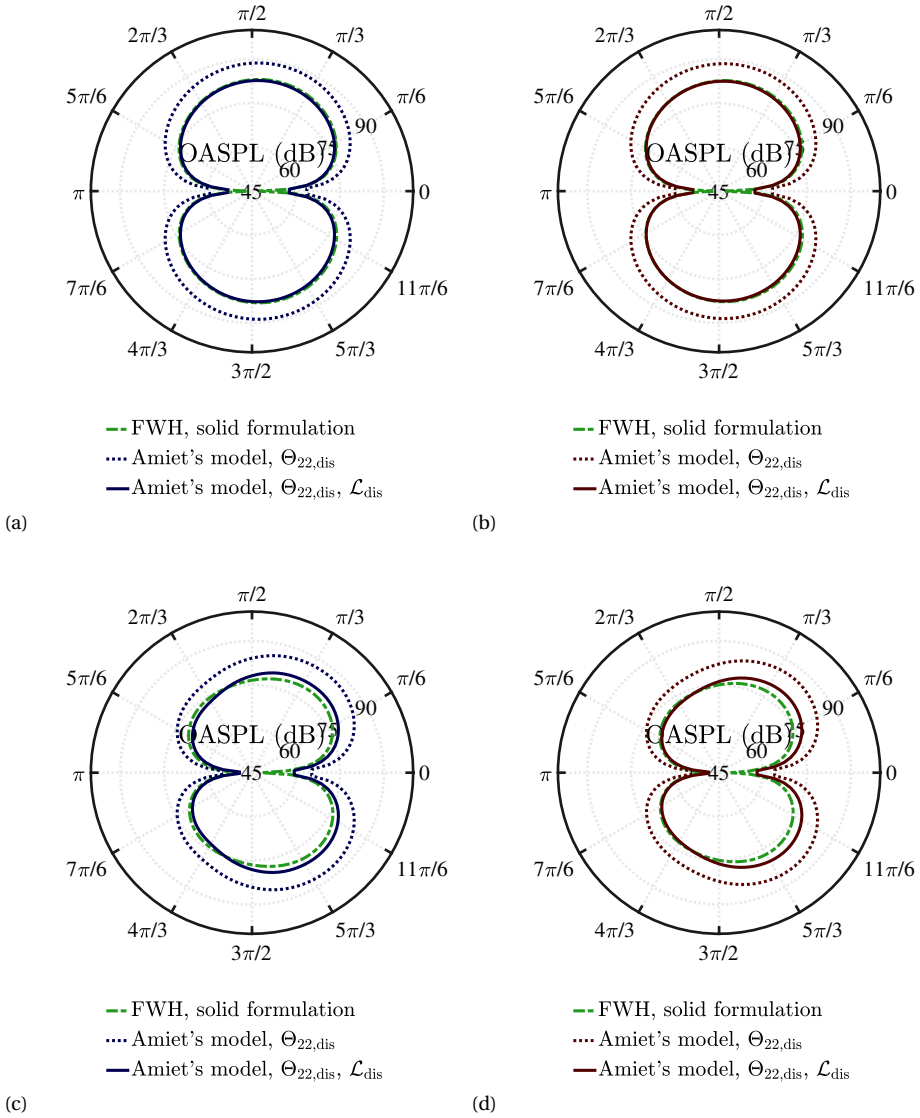

Figure 4.16: Far-field noise directivity patterns in the low-frequency range $St_t = [0.15, 0.35]$ for the (a) NACA 0012 and (b) NACA 0012-103 and in the high-frequency range $St_t = [0.35, 1.5]$ for the (c) NACA 0012 and (d) NACA 0012-103. Amiet's model implementations using the distorted spectrum as input with and without the corrected transfer function are compared with the FWH results.

simulations for both aerofoils in the two considered frequency ranges, although a slight discrepancy is still present in the range $-\pi/3 < \theta < \pi/3$.

The implementation of this correction proves that modifying the term describing the turbulence characteristics in Amiet's model allows the distortion effects due to the realistic aerofoil geometry to be accounted for in the turbulence term. The physical modelling of the noise generation is thus enhanced without requiring significant modifications in the analytical formulation of the aerofoil acoustic response, at least for $L_1/a > 1$. Indeed, a correct estimation of the noise levels can be achieved through the flat-plate-based formulation of the aeroacoustic transfer function, which must be scaled accordingly to consider the effects of the altered perturbation, associated in turn with the increase in the energy content of the distorted upwash velocity component in the stagnation region.

5

ANALYTICAL MODELLING

The key finding from the physical analysis in Chapter 4 is that the influence of realistic geometries can be effectively captured within Amiet's model by incorporating a distorted turbulence spectrum, $\Theta_{22,\mathrm{dis}}$, evaluated at the stagnation point. This results in accurate noise predictions for these configurations. However, to make this correction practical, a procedure is required to calculate such distorted turbulence characteristics from upstream, well-known turbulence properties.

Building on this finding, this chapter presents a turbulence-distortion modelling methodology for Amiet's model enhancement. This methodology accounts for the alteration of the velocity field at the stagnation point and accounts for the resulting effects on the aerofoil acoustic response. This approach is based on the use of the asymptotic results of the RDT to calculate the alteration of the upwash velocity component spectrum and the variation of the upwash-gust energy starting from upstream flow conditions. The application of RDT results for aerofoil configurations has been made possible through the identification of the geometrical feature affecting turbulence distortion for such geometries presented in Chapter 4. The result is the formulation of a consistent and general procedure to enhance the noise prediction using only upstream undistorted flow characteristics (integral length scale and turbulence intensity) and the characteristic "distortion length", eliminating the need to specify a position in the stagnation region for sampling distorted-turbulence characteristics.

The present analytical study entails three conceptual steps: (i) generalising the physical insights from Chapter 4 by investigating additional configurations; (ii) formulating analytical expressions to model the observed behaviour and characterise turbulence interaction with aerofoil geometries; and (iii) incorporating these expressions into a general framework, i.e. the proposed turbulence-distortion modelling methodology.

As explained in Chapter 3, this work has been validated through four LBM numerical simulations of three aerofoils — NACA 0012, NACA 0012-103, and NACA 4412 — interacting with grid-generated turbulence under zero lift and lifting conditions.

5.1. DISTORTION MECHANISM FOR REALISTIC AEROFOIL GEOMETRIES

The application of the RDT for an aerofoil depends on the identification of the geometrical parameter a with respect to which the scale of the incoming turbulence L_1 shall be compared, for which no agreement in the literature has been reached yet. To this aim, the surface-pressure distribution on the aerofoil leading edge for the numerical configurations is investigated to gain knowledge on the geometry effects on turbulence distortion and noise generation. The analysis builds on the results of Chapter 4, obtained for symmetrical aerofoils, and extends them to the cambered and loaded geometries examined in this study. The non-dimensional pressure gradient along the surface and the root-mean-square of the surface-pressure fluctuations are shown in Fig. 5.1 for the numerical configurations considered. These two quantities have been plotted with respect to the curvilinear abscissa s, which originates at the trailing edge and is directed from the upper to the lower side of the aerofoil. The leading edge is localised around $s/c = 1$, depending on the camber and the aerofoil curvature, while the position of the stagnation point is determined by the flow incidence. In the case of the symmetrical aerofoils at a zero angle of attack, the leading edge and stagnation point coincide (Figs. 5.1a and 5.1b), resulting in $s_{\text{stag}} \simeq s_{\text{LE}}$. For the NACA 4412 at zero-lift conditions, the stagnation point is on the upper side of the aerofoil, i.e. $s_{\text{stag}} < s_{\text{LE}}$ (Fig. 5.1c), while, at lifting conditions, it is placed on the lower side, i.e. $s_{\text{stag}} > s_{\text{LE}}$ (Fig. 5.1d).

For both symmetrical and cambered aerofoils, two peaks of the root-mean-square of the surface-pressure fluctuations are found in the vicinity of the stagnation point, on the pressure and the suction side. As expected, the two symmetrical aerofoils feature symmetric peaks on the two sides, whereas this is not the case for the cambered configurations. These peaks are further apart in the case of the NACA 0012-103, which features a larger leading-edge circle with respect to the baseline NACA 0012. Interestingly, in all four configurations, surface-pressure fluctuations and pressure gradient reach the maximum value almost at the same positions on the pressure and suction sides, with the latter peaking slightly closer to the stagnation point.

As proposed by Piccolo et al. [126], the results suggest that the increase in unsteady surface pressure, typically associated with sound generation, may be related to the flow acceleration due to the pressure gradients caused by the leading-edge curvature. Therefore, it can be assumed that the acceleration can be responsible for the deformation of the turbulent structures impinging on the aerofoil. As a consequence, considering a turbulent eddy convected along a streamline curved by the action of the aerofoil on the flow, the size of the eddy with respect to the space available to accelerate on the pressure and the suction sides of the aerofoil impacts its deformation during the interaction with the surface. This "distortion length" can be estimated by considering the length along the leading edge from the stagnation point to the two positions where the surface-pressure fluctuations peak on the pressure and suction sides of the aerofoil. A good estimate of this length can be thus obtained by halving the distance between these two positions. This parameter, denoted as l_{dis}, is chosen as the geometrical characteristic dimension a to be used for the application of the RDT in the case of more realistic aerodynamic surfaces. The corresponding values for the 4 numerical configurations considered are

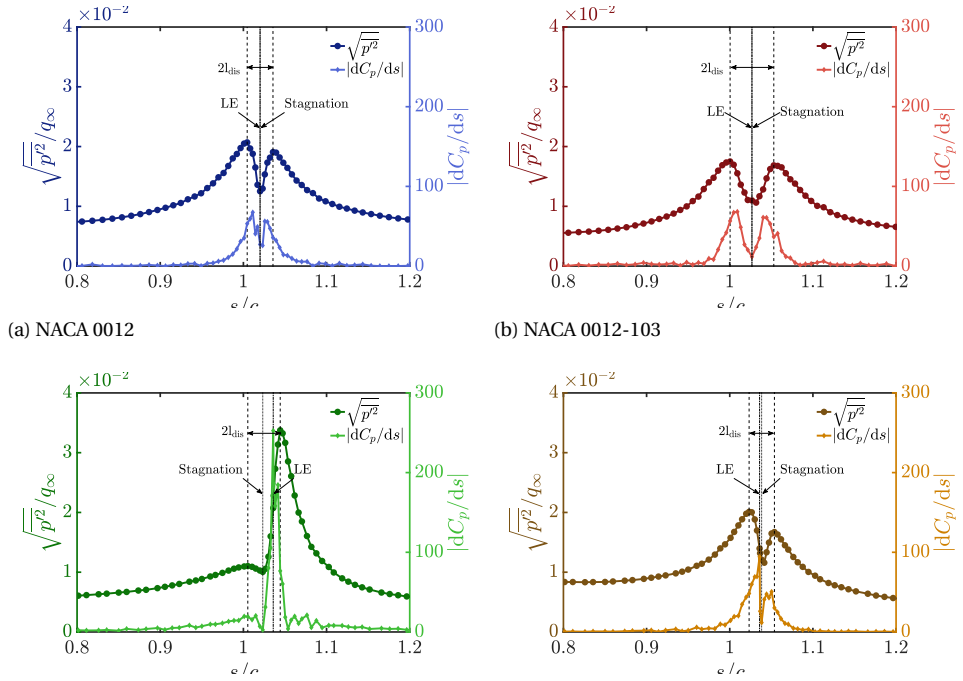

(a) NACA 0012

(b) NACA 0012-103

(c) NACA 4412, $\alpha = \alpha_{ZL}$

(d) NACA 4412, $\alpha = 1°$

Figure 5.1: Distribution of the time-averaged pressure gradient and root-mean-square of the surface-pressure fluctuations with respect to the curvilinear abscissa s.

reported in Table 5.1.

It is worth now investigating the potential links between the surface-pressure distribution and the aerofoil geometry to identify a practical criterion to determine l_{dis} and hence the parameter a without the knowledge of the flow field. Figure 5.2 shows the time-averaged surface pressure gradient along s together with the derivative of the aerofoil-surface curvature. In the case of the symmetrical aerofoils at a zero angle of attack, a correspondence exists between the position where the root-mean-square of the pressure fluctuations reaches its maximum value, the location where pressure gradient peaks, and the curvilinear abscissa where the curvature of the aerofoil changes more abruptly. For both NACA 0012 and NACA 0012-103, the pressure gradient and curvature derivative peaks occur slightly earlier than the maximum surface pressure fluctuations. While a similar physical behaviour is observed for the cambered aerofoil, with the surface-pressure fluctuations peaking alongside the pressure gradient because of the strong curvature variation, there is no exact correspondence between these peak positions, neither at zero loading condition (Fig. 5.2c) nor at a small incidence (Fig. 5.2d).

These observations thus identify a relationship between the pressure gradient, which induces the flow acceleration and the deformation of the turbulent structures, with the curvature of the flow around the leading edge. In the case of symmetrical thin aero-

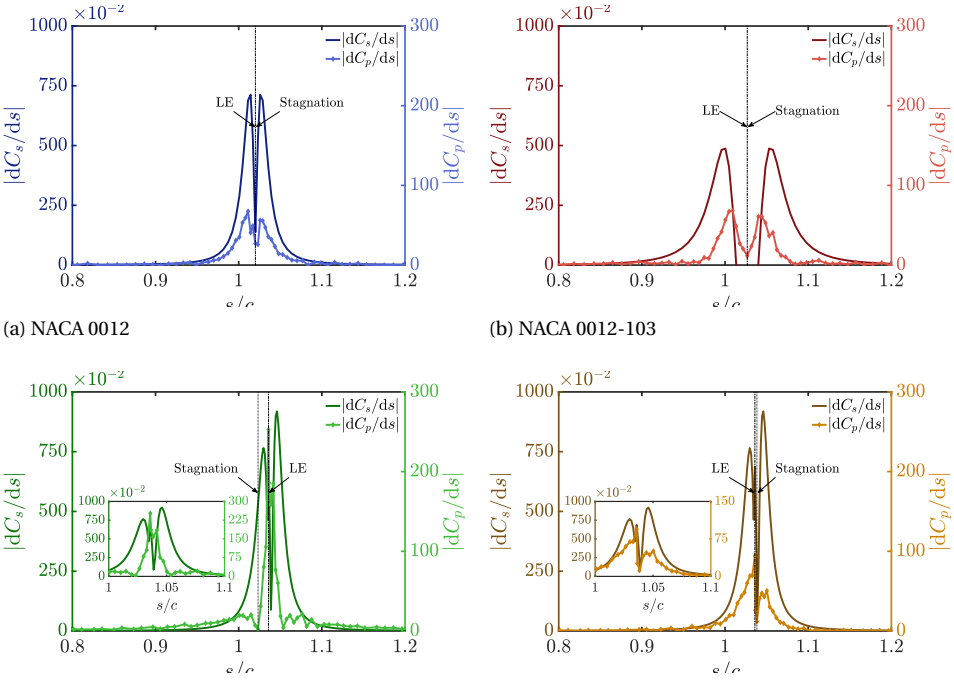

(a) NACA 0012

(b) NACA 0012-103

(c) NACA 4412, $\alpha = \alpha_{ZL}$

(d) NACA 4412, $\alpha = 1°$

Figure 5.2: Distribution of the aerofoil surface-curvature derivative and the time-averaged pressure gradient with respect to the curvilinear abscissa s.

foils at zero angle of attack, the flow follows the aerofoil surface, explaining the correspondence between the peaking positions of the curvature derivative and the pressure gradient. Therefore, a possible way to estimate a knowing only the aerofoil geometry is by evaluating $|\mathrm{d}C_s/\mathrm{d}s|$, for instance using the panel method code XFOIL [127]. This will be evaluated in Subsection 5.3.2 using XFOIL data to validate the proposed methodology against the experimental data of Chaitanya et al. [34]. Regarding the cambered aerofoils, while the physical description of the distortion mechanism remains valid, further investigations are needed to establish an equivalent procedure for estimating the reference geometric parameter for RDT applications solely from geometrical and aerodynamic data known *a priori*.

5.2. TURBULENCE-DISTORTION MODELLING FOR LOW-FIDELITY NOISE-PREDICTION METHODS

The proposed methodology aims to calculate, starting from undistorted turbulence data at upstream conditions, the alteration of the velocity field and acoustic response induced by turbulence distortion. Referring to Amiet's formulation for large-span aerofoils (Eq. (2.13)), this is achieved by modelling the alteration of the turbulence frequency

NACA	$l_{\text{dis}} = a$ (m)	L_1/a (−)
0012	2.40×10^{-3}	2.50
0012-103	3.30×10^{-3}	1.80
4412, $\alpha = \alpha_{\text{zl}}$	2.90×10^{-3}	2.00
4412, $\alpha = 1°$	2.20×10^{-3}	2.66

Table 5.1: "Distortion length" for the 4 aerofoil configurations. The ratio L_1/a is reported as well. The RDT parameter a has been taken equal to l_{dis}, estimated by halving the distance between the positions where the root-mean-square of the surface pressure fluctuations peaks on the two sides of the aerofoil.

spectrum Θ_{22} and the spanwise coherence length $l_3(\omega)$ of the upwash velocity component, and the aeroacoustic transfer function $\mathscr{L}$.

The corrections, detailed in Subsection 5.2.1, Subsection 5.2.2, and Subsection 5.2.3, result in the following formulation for a distortion-corrected Amiet's model to retrieve the PSD of the far-field acoustic pressure $S_{pp}(\omega)$ at a listener position $\boldsymbol{x} = (x_1, x_2, 0)$:

$$S_{pp}(x_1, x_2, 0, \omega) = \left(\frac{\omega x_2 \rho_\infty c M_\infty}{2\sigma_0^2}\right)^2 \frac{L}{2} |\mathscr{L}_{\text{dis}}(\boldsymbol{x}, K_1, 0)|^2 \Theta_{22,\text{dis}}(\omega)\, l_{3,\text{mod}}(\omega)\,. \tag{5.1}$$

This corresponds to Eq. (2.13), valid for a listener in the midspan position of the aerofoil. For a detailed derivation of the expression, the reader is referred to 2.1, where Amiet's theory for leading-edge noise is presented.

5.2.1. DISTORTED-TURBULENCE SPECTRUM MODELLING

As explained in Section 2.2, in the asymptotic cases of very large-scale and very small-scale turbulence, the four partial differential equations derived by Hunt [45] in the RDT framework to model the distorted field from upstream conditions are simplified into closed-form analytical expressions.

The semi-analytical method discussed here entails the interpolation of these equations to retrieve a single expression for $\Theta_{22,\text{dis}}$ valid on the whole wavenumber range. This holds true under the assumption $L_1/a > 1$, which justifies the use of the asymptotic result obtained for large-scale turbulence to model the alteration of the spectrum in the low-wavenumber range ($k \to 0$). This procedure allows the distorted spectrum near the stagnation point to be estimated using only the intensity and integral length scale of the upstream undistorted turbulence as inputs, along with the geometrical characteristic length of the aerofoil.

ASYMPTOTIC ANALYSES IN THE CASE OF LARGE-SCALE TURBULENCE AND LOW-WAVENUMBER ALTERATION MODELLING

For large-scale turbulence ($L_1/a \gg 1$), the asymptotic analysis of Hunt [45] leads to Eq. (2.90) for the one-dimensional distorted spectrum of the upwash velocity component $\Theta_{22,\text{dis}}$ along the stagnation streamline. The equation is reported here for conveni-

ence

$$\Theta^*_{22,\mathrm{dis}}(\kappa_1) = \underbrace{\left[1 + \frac{1}{\left(1-\frac{x_1}{a}\right)^2}\right]^2}_{\lambda_2^2(x_1)} \Theta^*_{22,\mathrm{ups}}(\kappa_1)\,.$$

This expression indicates that the alteration of the velocity spectra consists of an increase in the upwash velocity component with respect to the upstream undistorted conditions. A factor $\lambda_2^2(x_1)$, depending on the distance from the stagnation point, is employed to represent this variation, which is related to the momentum transfer from the streamwise to the upwash velocity component occurring for large-scale turbulence, as explained by Hunt [45].

The alteration of the velocity spectra in the low-wavenumber range for an aerofoil can thus be evaluated by extending the analytical relations derived for the cylinder case. By replacing x_1 with a curvilinear abscissa ξ_1 for the distance along a generically curved stagnation streamline, it is finally obtained

$$\Theta_{22,\mathrm{dis}}(k_1)\Big|_{\mathrm{lowk}} = \lambda_2^2(\xi_1)\Big|_{\xi_1=0} \Theta_{22,\mathrm{vK}}(k_1)\,, \tag{5.2}$$

with $\Theta_{22,\mathrm{vK}}$ indicating a canonical von Kármán expression (see Eq. (3.6)) employed to model the upstream undistorted flow conditions. The alteration in the immediate vicinity of the stagnation point can be described by considering the distance from the stagnation point $\xi_1 \to 0$, which results in $\lambda_2^2(0) \approx 4$.

ASYMPTOTIC ANALYSES IN THE CASE OF SMALL-SCALE TURBULENCE AND HIGH-WAVENUMBER ALTERATION MODELLING

For small-scale turbulence, Hunt [45] showed that the spectrum of the upwash velocity component in the immediate vicinity of the stagnation point decays with an exponential slope according to Eq. (2.95). Note that this equation is non-dimensional and will be converted to dimensional form by multiplying it by $u_1'^2 L_1$ and by a/L_1 (see Eq. (2.82)). Additionally, it is important to highlight that this expression is obtained from Eq. (2.81), which calculates the spectrum by performing two integrations between $-\infty$ and ∞ of a double-sided spectrum. Consequently, a factor 8 is necessary for comparison with one-dimensional single-sided spectra.

In the high-wavenumber range, the alteration of the upwash velocity spectrum in the case of an aerofoil can hence be modelled through

$$\Theta_{22,\mathrm{dis}}(k_1)\Big|_{\mathrm{highk}} = 8\left(u_1'^2 L_1\right)(a/L_1)\, G_1(a/L_1)^{-\frac{2}{3}} (ak_1)^{-\frac{7}{3}} \mathrm{e}^{-\frac{1}{2}\pi a k_1}. \tag{5.3}$$

The small-scale turbulence limit formally holds for $k_1 \to \infty$. However, considering that this expression models the attenuation of the upwash velocity fluctuation with respect to upstream undistorted conditions, the proposed semi-analytical method adopts Eq. (5.3) for $k_1 > k_{1,\mathrm{CP}}$, with $k_{1,\mathrm{CP}}$ indicating the intersection with the von Kármán spectrum describing undistorted turbulence (the subscript CP standing for “crossing point").

NACA	$\xi_{1,\text{ups}}$		$\xi_{1,\text{dis}}$	
	$x_{1,\text{ups}}$ (m)	$x_{2,\text{ups}}$ (m)	$x_{1,\text{dis}}$ (m)	$x_{2,\text{dis}}$ (m)
0012	-0.075	0	1.50×10^{-5}	0
0012-103			1.50×10^{-5}	0
4412, $\alpha=\alpha_{\text{zl}}$			1.61×10^{-5}	-1.56×10^{-3}
4412, $\alpha=1°$			3.32×10^{-4}	4.76×10^{-3}

Table 5.2: Cartesian coordinates of the sampling positions of the turbulence characteristics in the undistorted ($\xi_{1,\text{ups}}$) and distorted ($\xi_{2,\text{ups}}$) flow-field regions selected to assess turbulence-distortion effects.

MID-WAVENUMBERS INTERPOLATION

Differently from the very large and very small-scale turbulence limit cases, the transition region before $k_{1,\text{CP}}$ lacks any empirical or theoretical description providing simplified analytical relations and can be derived only through the solution of the RDT equations [45].

In order to finalise the semi-analytical method and provide a continuous piece-wise spectrum as an output, the distorted spectrum in this wavenumber range has been modelled by merging the analytical equations of the two limit cases. The expression used for low wavenumbers is considered valid up to $k_1 = k_{1,\text{CP}}$ but it is multiplied by an exponential function, which models the decay in the high-wavenumber range, to obtain a continuous and gradual transition. The alteration of the upwash velocity spectrum in the low and the mid-wavenumber region will be thus described by

$$\Theta_{22,\text{dis}}(k_1)\Big|_{\text{low-midk}} = \Theta_{22,\text{dis}}(k_1)\Big|_{\text{lowk}} \mathrm{e}^{Bk_1} = \lambda_2^2(\xi_1)\Big|_{\xi_1=0} \Theta_{22,\text{vK}}(k_1)\,\mathrm{e}^{Bk_1}, \tag{5.4}$$

with the coefficient B determined by imposing the continuity of the function at $k_1 = k_{1,\text{CP}}$.

Finally, the distortion-corrected upwash velocity spectrum yielded by the proposed semi-analytical method will hence read

$$\Theta_{22,\text{dis}}(k_1) = \begin{cases} \lambda_2^2(\xi_1)\Big|_{\xi_1=0} \Theta_{22,\text{vK}}(k_1)\,\mathrm{e}^{Bk_1}, & k_1 \le k_{1,\text{CP}} \\ 8\left(u_1'^2 L_1\right) G_1(a/L_1)^{\frac{1}{3}} (a\,k_1)^{-\frac{7}{3}}\,\mathrm{e}^{-\frac{1}{2}\pi a k_1}, & k_1 \ge k_{1,\text{CP}} \end{cases}. \tag{5.5}$$

The expression for $\Theta_{22,\text{dis}}$ is of differentiability class C^0, since the derivative is not continuous at $k_{1,\text{CP}}$.

Figure 5.3 shows the validation of the upwash velocity spectra provided by Equation (5.5) and the numerical ones obtained with PowerFLOW (PF in the plots) in the stagnation region. These spectra are displayed as a function of the Strouhal number, St_t, calculated using the aerofoil thickness, to be consistent with the investigation of Chaitanya et al. [34]. Being ξ_1 the distance from the stagnation point along the stagnation streamline, the numerical upwash velocity spectra have been considered far upstream from the leading edge ($\xi_{1,\text{ups}}/c = -0.5$) and in the immediate vicinity of the stagnation point ($\xi_{1,\text{ups}}/c = -1.5\times10^{-3}$). The coordinates of these positions are reported in Table 5.2,

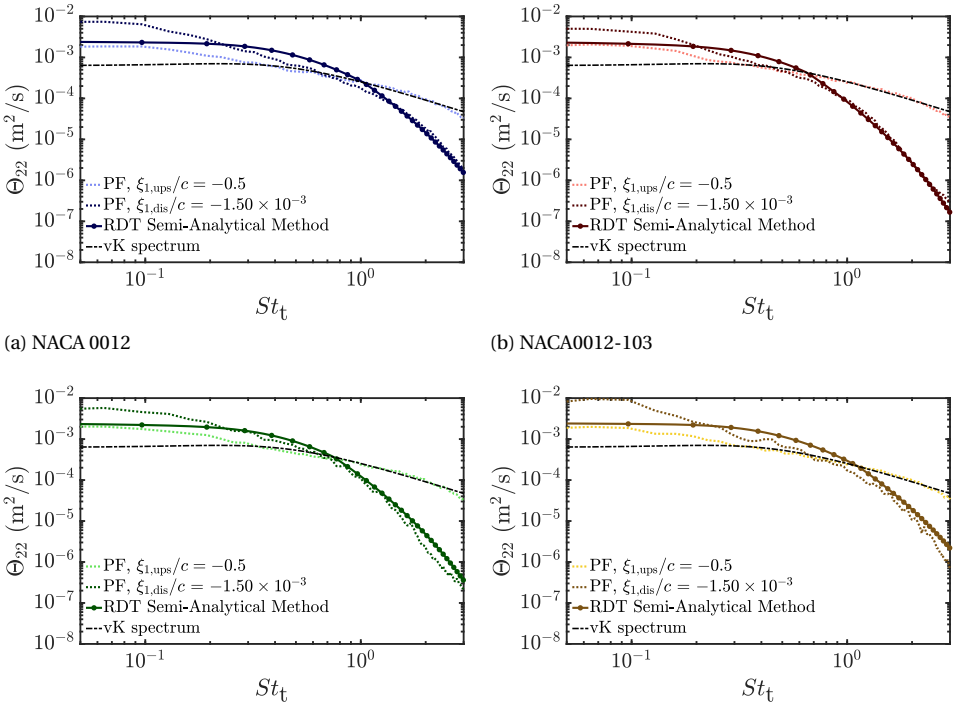

(a) NACA 0012

(b) NACA0012-103

(c) NACA 4412, $\alpha = \alpha_{ZL}$

(d) NACA 4412, $\alpha = 1°$

Figure 5.3: Comparison between the upwash velocity component spectra obtained with the semi-analytical method based on the RDT findings and the turbulence spectra derived numerically.

while the L_1/a ratios for the four configurations are reported in Table 5.1 (information about the integral length scale is reported in 3.2.2). Such position is not required to retrieve the semi-analytical spectra, calculated in the limit $\xi_1 \to 0$.

With the exception of the mid-frequencies range, the semi-analytical method proposed herein is able to provide a good estimate of the alteration of the upwash velocity component spectrum using as input only the upstream undisturbed values of the turbulence integral length scale and intensity. The slight discrepancy observed in the low-frequency range is due to the small flow anisotropy caused by the strong contraction of the nozzle (see 3.2.2 and Piccolo et al. [126]). This is not taken into account in the present application of the model, which employs a von Kármán expression, valid in the case of homogeneous isotropic turbulence, to describe upstream flow characteristics. As a matter of fact, slight anisotropic turbulence conditions in the upstream flow could be accounted for using *ad hoc* analytical expressions for the velocity spectrum as input in the semi-analytical method.

These results prove that this approach represents a viable and efficient tool to model the alteration of the upwash velocity component spectrum caused by turbulence distortion.

The semi-analytical method is generalised beyond the narrow range of L_1/a considered by comparing the resulting distorted spectra with those provided by the solution of the RDT equations. This implementation, based on the work of Zamponi et al. [82] and validated against experimental data, allows the modelling of the alteration of the velocity field through Eq. (2.81) for any L_1/a ratio using as input only the analytical expression for a velocity spectrum describing homogeneous isotropic flow conditions. However, the high computational cost associated with the implementation of this formulation prevents it from being directly used to enhance the low-fidelity prediction.

The comparison between the distorted upwash velocity spectrum obtained through Eq. (5.5) and using the solution of the RDT equations is reported in Fig. 5.4. The spectra are shown with respect to the wavenumber $\hat{\boldsymbol{\kappa}}$. Differently from the proposed semi-analytical method, solving the RDT equations requires specifying the distance from the stagnation point. The altered turbulence spectra have been hence calculated at a distance from the stagnation point equal to $\xi_1/a = -2.5 \times 10^{-3}$, while the upwash velocity spectrum representing upstream undistorted conditions have been calculated implementing RDT equations at $\xi_1/a = -20$. The von Kármán spectrum has been included as a reference for the undistorted turbulence conditions, together with the two curves representing the two asymptotic trends describing the alteration of the one-dimensional velocity spectrum in the low and the high-wavenumber ranges. The validation has been carried out for a wide range of $L_1/a \gg 1$, reported in the respective plots. For all the cases, the large-scale-turbulence asymptotic trend provides a good approximation of the RDT results up to the non-dimensional wavenumber $\hat{\kappa}_1 = 1$. The high-frequency asymptote overlaps with the spectrum obtained with the solution of the RDT equations for $\hat{\kappa}_1 > \hat{\kappa}_{1,\mathrm{CP}}$. A good result is also achieved in the transient region, between $1 < \hat{\kappa}_1 < \hat{\kappa}_{1,\mathrm{CP}}$. This represents a further confirmation that the semi-analytical spectrum provided by Eq. (5.5) represents a valid methodology to effectively model the alteration of the velocity field due to the interaction of incoming turbulence with a realistic aerofoil geometry across a wide range of conditions.

5.2.2. EMPIRICAL MODIFICATION OF THE SPANWISE COHERENCE LENGTH EQUATION

The spanwise coherence length is introduced in Amiet [16] to model the spanwise characteristics of the incoming turbulent flow. This is obtained in Amiet's theory as the ratio between the von Kármán expressions of the two-dimensional wavenumber spectrum $\Psi_{22}(k_1, k_3)$ and the single-wavenumber one $\Theta_{22}(k_1)$ of the upwash velocity component, resulting in

$$l_3(\omega) = \pi \frac{\Psi_{22}(k_1, 0)}{\Theta_{22}(k_1)} = \frac{8L_1}{3} \left[\frac{\Gamma(1/3)}{\Gamma(5/6)}\right]^2 \frac{(k_1/k_e)^2}{\left(3 + 8(k_1/k_e)^2\right)\sqrt{1 + (k_1/k_e)^2}}, \tag{5.6}$$

with k_e defined as the wavenumber scale of the largest eddies [108] according to

$$k_e = \frac{\sqrt{\pi}}{L_1} \frac{\Gamma(5/6)}{\Gamma(1/3)}. \tag{5.7}$$

Figure 5.5 shows the implementation of Eq. (5.6) together with the spanwise coherence length calculated numerically for the four analysed configurations far upstream at $\xi_{1,\mathrm{ups}}/c =$

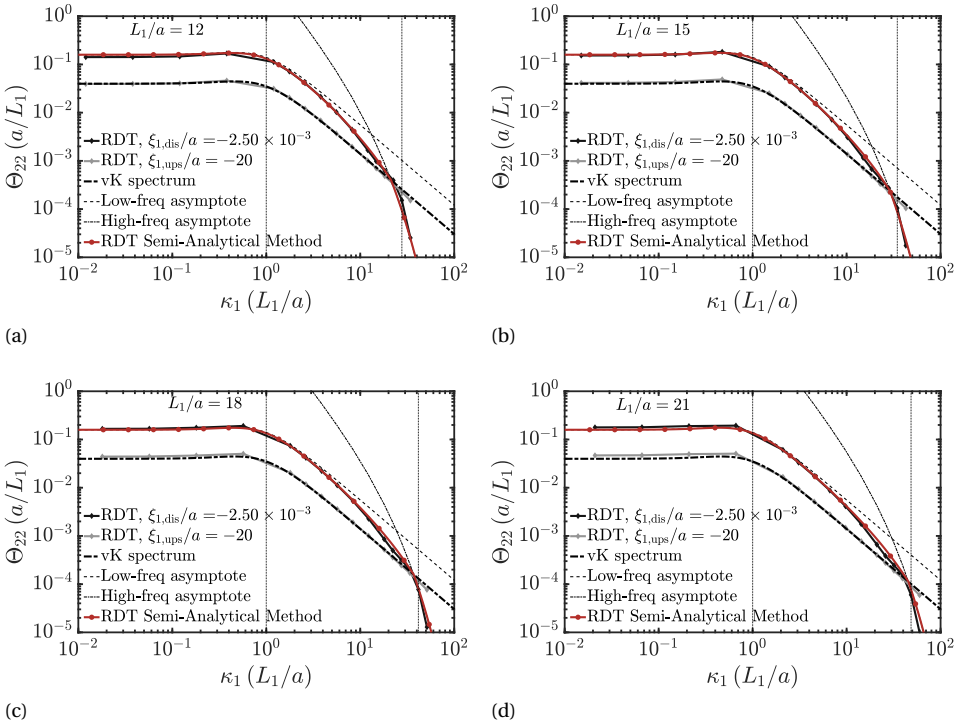

Figure 5.4: Comparison between the upwash velocity component spectra obtained with the solution of the RDT equations and the semi-analytical expression of Eq. (5.5) based on the asymptotic results.

-0.5 and in the stagnation region at $\xi_{1,\mathrm{dis}}/c = -1.5 \times 10^{-3}$. A significant discrepancy is found in the low-frequency range with respect to Amiet's analytical expression. Moreover, turbulence distortion appears to alter the spanwise coherence as well, inducing an evident increase at low frequencies. This range is associated with the behaviour of large-scale turbulent structures, suggesting that only the distortion of these scales affects the turbulent field in the spanwise direction.

Turbulence-distortion effects in this direction can be investigated by assessing the variation along the stagnation streamline of the correlation length L_{22}^3, relative to the distribution along the direction x_3 of the upwash velocity component u_2 and representative of the energy contained at large turbulence scales. Table 5.3 reports the value of L_{22}^3 sampled at the upstream position and in the proximity of the stagnation point. This has been calculated using Eq. (3.4). The variation of this parameter, which doubles as the leading edge is approached for all the four configurations taken into account, confirms that the large turbulence scales, as they approach the stagnation region, become increasingly more coherent in the spanwise direction.

This effect can be accounted for by empirically modifying Eq. (5.6) to include the correlation length of the upwash velocity component L_{22}^3 rather than the streamwise integral length scale L_1. Indeed, it must be noted that the von Kármán expressions for

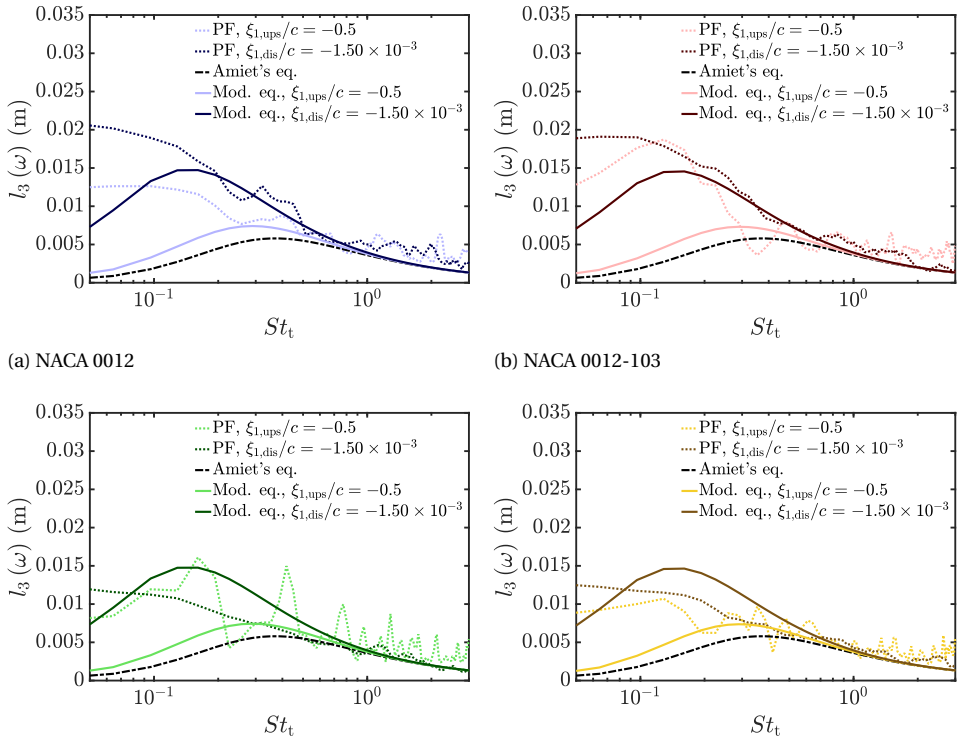

(a) NACA 0012

(b) NACA 0012-103

(c) NACA 4412, $\alpha = \alpha_{ZL}$

(d) NACA 4412, $\alpha = 1°$

Figure 5.5: Spanwise coherence length of the upwash velocity component far upstream ($\xi_{1,\mathrm{ups}}/c = -0.5$) and in the vicinity ($\xi_{1,\mathrm{dis}}/c = -1.5 \times 10^{-3}$) of the stagnation point. The numerical calculation is shown together with the result of the original analytical expression proposed by Amiet (Eq. (5.6)) and the proposed semi-empirical approach (indicated as "Mod. eq.", Eq. (5.8)).

the one and two-dimensional spectra of the upwash velocity component $\Theta_{22}(k_1)$ and $\Psi_{22}(k_1, k_3)$, from which the equation for the spanwise coherence length is obtained, feature the streamwise integral length scale L_1 because they are formulated in the assumption of homogeneous isotropic turbulence. Under this hypothesis, the length scales of the velocity components are related, meaning that the expressions can be modified to make explicit the dependency on the correlation length of the upwash velocity component L_{22}^3. By doing so and by using the local value of L_{22}^3, the effects associated with the alteration of this velocity component can be encompassed. The following expression is hence obtained:

$$l_{3,\mathrm{mod}}(\omega, \xi_1) = \frac{16 L_{22}^3(\xi_1)}{3} \left[\frac{\Gamma(1/3)}{\Gamma(5/6)}\right]^2 \frac{\left(k_1/k_{e,\mathrm{mod}}\right)^2}{\left(3+8\left(k_1/k_{e,\mathrm{mod}}\right)^2\right)\sqrt{1+\left(k_1/k_{e,\mathrm{mod}}\right)^2}}, \tag{5.8}$$

with the wavenumber non-dimensionalised using L_{22}^3 and the parameter k_e, obtained

NACA	$L_{22}^3\big\|_{\xi_1=\xi_{1,\text{ups}}}$ (m)	$L_{22}^3\big\|_{\xi_1=\xi_{1,\text{dis}}}$ (m)
0012	7.5×10^{-3}	0.015
0012-103		0.014
4412, $\alpha=\alpha_{\text{zl}}$		0.020
4412, $\alpha=1°$		0.021

Table 5.3: Length scale of the upwash velocity component calculated in the spanwise direction in the undistorted ($\xi_{1,\text{ups}}$) and distorted ($\xi_{1,\text{dis}}$) flow-field regions selected to assess turbulence-distortion effects for the four aerofoil configurations.

through Eq. (5.7), modified accordingly through

$$k_{e,\text{mod}}(\xi_1)=\frac{\sqrt{\pi}}{L_{22}^3(\xi_1)}\frac{\Gamma(5/6)}{\Gamma(1/3)}, \tag{5.9}$$

the subscript $_{\text{mod}}$ standing for “modified".

The spanwise coherence length at the stagnation point will be hence retrieved from the local value of the correlation length L_{22}^3, which, following the physical observations for the four aerofoil configurations, can be expressed as twice the value measured far upstream. This allows distortion effects on the spanwise coherence length to be predicted in terms of the upstream undistorted flow conditions.

The implementation of the physics-based correction for the spanwise coherence length (Eq. (5.8)) is reported in Fig. 5.5 for the four aerofoil configurations. For the two symmetrical aerofoils, acceptable results are obtained in the modelling of the spanwise coherence length through Eq. (5.8) for both the undistorted and distorted cases. As in the case of the upwash velocity spectra, the slight turbulence anisotropy is supposed to affect the accuracy of the modelling in the low-frequency range. For the NACA 4412, instead, a less convincing agreement is obtained to model the altered spanwise coherence length close to the leading edge, meaning that further investigations are still required to propose a more effective and general modification for these configurations.

5.2.3. TURBULENCE-DISTORTION EFFECTS ON THE AEROACOUSTIC TRANSFER FUNCTION

The effects of turbulence distortion on the acoustic response have been widely explained in Section 4.5, both from a physical and a modelling perspective. For completeness, the modelling perspective is briefly revisited here to integrate the modification of the aeroacoustic transfer function into the broader analytical framework presented in this chapter.

Referring to the overview of the theory in 2.1.1, Amiet models the aerofoil acoustic response by calculating the pressure jump on a flat plate using a quasi-steady theory. This approach, which models turbulence-related effects as variations in free-stream velocity and incidence, is valid for large-scale structures interacting with an infinitely thin aerodynamic surface. As a result, surface-pressure distribution and noise scattering

are assumed to be generated by large-scale undistorted turbulence. However, the RDT demonstrates that large-scale turbulence is actually distorted because of the presence of the aerofoil, with the resulting alteration of the velocity field consisting of a decrease of the streamwise velocity component fluctuations and an increase of the upwash velocity component fluctuations [45]. This variation can be modelled through asymptotic relations, as proposed in Subsection 5.2.1, which the present methodology thus employs to capture this effect. In the limit case $L_1/a \gg 1$, starting from Eq. (2.94) and expressing the velocity tensor through Eq. (2.89), the following expressions are obtained for the root-mean-square of the velocity components as a function of the distance from the leading edge along the stagnation streamline

$$\sqrt{\overline{u_1'^2}} = \sqrt{\overline{u_{1,\mathrm{ups}}'^2}} \left[1 - \frac{1}{\left(1 - \frac{x_1}{a}\right)^2} \right] \tag{5.10a}$$

$$\sqrt{\overline{u_2'^2}} = \sqrt{\overline{u_{2,\mathrm{ups}}'^2}} \underbrace{\left[1 + \frac{1}{\left(1 - \frac{x_1}{a}\right)^2} \right]}_{\lambda_2(x_1)} \tag{5.10b}$$

$$\sqrt{\overline{u_3'^2}} = \sqrt{\overline{u_{3,\mathrm{ups}}'^2}}. \tag{5.10c}$$

The function $\lambda_2(x_1)$ in Eq. (5.10b) has been introduced to describe the variation with respect to upstream conditions of the upwash velocity component. This same distortion mechanism is causing the alteration of the velocity spectra in the low-wavenumber range, detailed in Subsection 5.2.1 and modelled through Eq. (2.90), which indeed features the function $\lambda_2(x_1)$ squared. Note that this factor corresponds to the same λ_{dis} introduced in the physical analysis of the same mechanism carried out in Section 4.5. Consequently, it has been proven that a higher-energy turbulence input is taken into account once an altered upwash velocity component spectrum is used in Amiet's expression to enhance the modelling of the velocity field in the case of realistic aerofoil geometries. This implies that the transfer function relating the surface-pressure jump to the incoming gust should be scaled accordingly, as explained in Section 4.5.

This approach marks a significant difference from the procedures currently available in the literature, which model the alteration of the velocity spectrum by imposing the conservation of the variance with respect to upstream conditions [49, 50]. Not only is this assumption proven to be physically inaccurate by the results presented herein, but it also produces an incorrect description of the alteration of the velocity field in the low-wavenumber range, associated with the distortion of the large energy-containing eddies. Additionally, it must be kept into account that the unsteady surface loading and, hence, the sound scattering are induced by this higher-energy altered velocity field in the stagnation region [36, 37]. Requiring the altered velocity field to be characterised by the same energy content as the upstream undistorted conditions thus results in a poor representation of the noise-generation mechanisms.

A distortion-corrected aeroacoustic transfer function $\mathscr{L}_{\mathrm{dis}}$ can be formulated using the factor $\lambda_2(\xi_1)$ in the limit $\xi_1 \to 0$ to account for the increase of the gust amplitude with respect to the upstream conditions. The following expression is hence obtained

from Eq. (2.12):

$$\mathscr{L}_{\text{dis}}\left(x_1, K_1, k_3\right) = \left(\frac{1}{\lambda_2\left(\xi_1\right)}\right)\Big|_{\xi_1=0} \mathscr{L}\left(x_1, K_1, k_3\right) = \int_{-L/2}^{L/2} \left(\frac{1}{\lambda_2\left(\xi_1\right)}\right)\Big|_{\xi_1=0} g\left(x_{1,0}, K_1, k_3\right) \mathrm{e}^{-\mathrm{i}\omega x_{1,0}\left(M_\infty - x_1/\sigma\right)/c_\infty \beta^2} \mathrm{d}x_{1,0}, \quad (5.11)$$

with $\boldsymbol{x}_0 = \left(x_{1,0}, x_{2,0}, x_{3,0}\right)$ indicating the coordinates of a point on the aerofoil platform area. The reader can refer to Subsection 2.1.1 for the derivation of the expression.

5.3. APPLICATION OF THE TURBULENCE-DISTORTION MODELLING METHODOLOGY TO AMIET'S MODEL

5.3.1. VALIDATION WITH NUMERICAL DATA

The accuracy of the proposed methodology for correcting Amiet's model has been assessed by comparing the prediction with the far-field noise provided by the solid formulation of the FWH analogy in terms of SPL and far-field noise directivity patterns.

Figure 5.6 reports the SPL for an observer at 1.2 m from the leading edge and at an angular position of $\theta = \pi/2$ with respect to the direction of the aerofoil chord. For all aerofoil configurations, the distortion-corrected Amiet's model shows excellent agreement with the noise calculated using the solid formulation of the FWH analogy. The semi-analytical method is able to correctly model the decay of the noise spectrum in the high-frequency range, related to the alteration of the vorticity field characterising the distortion of small-scale structures. An underestimation of less than 5 dB can be observed in the low-frequency range (up to $St_t \simeq 0.2$) for Amiet's model with respect to the FWH results. This is due to the fact that the RDT results, upon which the semi-analytical method is based, are obtained in the assumption of homogeneous and isotropic upstream turbulence and do not take into account the small anisotropy observed for the upwash velocity component spectrum at the exit of the nozzle (see 3.2.3). The discrepancy in this frequency range could be reduced by refining the modification of the spanwise coherence length, as it has a slight effect on the noise levels at low frequencies.

The analysis of the far-field noise directivity patterns has been carried out considering the frequency range where leading-edge noise dominates, $St_t = [0.15, 1.5]$. This corresponds to frequencies ranging from 500 Hz to 5 kHz. The comparison between the FWH results and the noise prediction provided by the semi-analytical method is reported in Fig. 5.7, where the OASPL is shown. An excellent agreement with FWH can be observed in the four cases at all angular positions, with the exception of a slight overestimation in the angular ranges $-\pi/3 < \theta < 0$ and $0 < \theta < \pi/3$. In this case, the polar coordinates are referred to the direction of the aerofoil chord in order to account for the fact that the cambered aerofoil is at $\alpha \neq 0$.

5.3.2. FURTHER VALIDATION WITH EXPERIMENTAL DATA

The robustness of the proposed methodology has been further evaluated against experimental data of four symmetrical aerofoils (NACA 0006, NACA 0009, NACA 0012, and NACA 0018) at different free-stream velocities ($U_{\infty,1} = 40\,\mathrm{m\,s^{-1}}$, $U_{\infty,2} = 60\,\mathrm{m\,s^{-1}}$, and

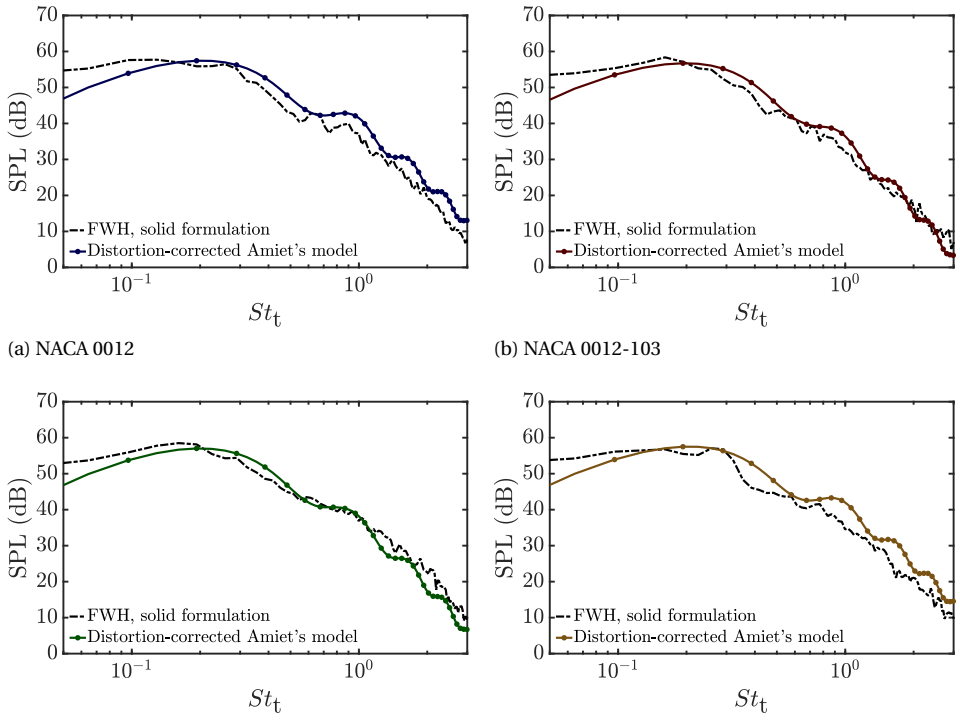

(a) NACA 0012

(b) NACA 0012-103

(c) NACA 4412, $\alpha = \alpha_{ZL}$

(d) NACA 4412, $\alpha = 1°$

Figure 5.6: Sound pressure level calculated with Amiet's model corrected using the turbulence-distortion modelling methodology compared to that calculated with the FWH analogy. The listener position is right above the leading edge ($R = 1.2\,\mathrm{m}$, $\theta = \pi/2$ with respect to the aerofoil chord direction), while the reference pressure to calculate the SPL is $2 \times 10^{-5}\,\mathrm{Pa}$.

$U_{\infty,3} = 80\,\mathrm{m\,s^{-1}}$) investigated by Chaitanya et al. [34]. Data for a flat plate at the same free-stream velocities, also reported by Chaitanya et al. [34], have been used as a reference to compute the relative SPL.

The methodology has been implemented taking as input the turbulence characteristics obtained experimentally ($L_1 = 0.0075\,\mathrm{m}$, $\mathrm{Tu}_2 = 2.5\,\%$), while the distortion length has been computed using XFOIL. In particular, as proposed in Section 5.1, the RDT parameter a for the application of the proposed approach has been taken equal to the distance between the peaks of the curvature derivative l_{dis}, which coincides with the distance between the maximum values of the pressure gradient. These values are reported in Table 5.4 together with the leading-edge radius, provided as a reference. Notably, the latter parameter closely approximates the distortion length, but this relationship holds only for smaller thicknesses and leading-edge radii. As these parameters increase, the distortion length diverges from the leading-edge radius, as observed in the NACA 0018 and previously in the NACA 0012-103. This indicates that r_{LE} is not the geometrical characteristic directly influencing turbulence distortion.

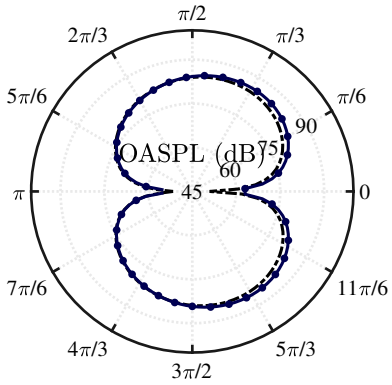

FWH, solid formulation

Distortion-corrected Amiet's model

(a) NACA 0012

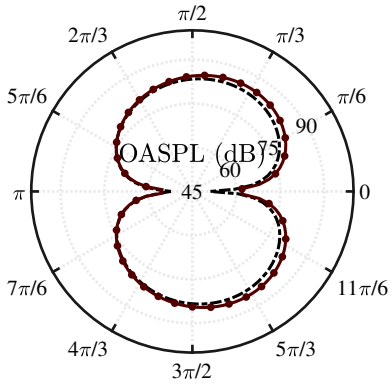

FWH, solid formulation

Distortion-corrected Amiet's model

(b) NACA 0012-103

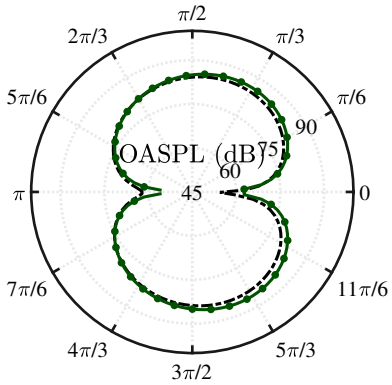

FWH, solid formulation

Distortion-corrected Amiet's model

(c) NACA 4412, $\alpha = \alpha_{ZL}$

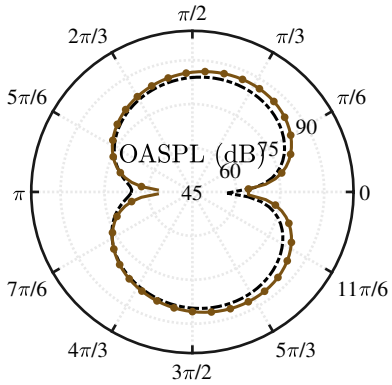

FWH, solid formulation

Distortion-corrected Amiet's model

(d) NACA 4412, $\alpha = 1°$

Figure 5.7: Far-field noise directivity patterns in the frequency range $St_t = [0.15, 1.5]$. The corrected Amiet's model implementations are compared with the FWH results.

NACA	r_{LE} (m)	$\Delta s\left\vert_{\frac{dC_p}{ds}}\right\vert_{max}$ (m)	$\Delta s\left\vert_{\frac{dC_s}{ds}}\right\vert_{max} = l_{dis} = a$ (m)	$\frac{L_1}{a}$ [−]
0006	5.95×10^{-4}	6.32×10^{-4}	5.68×10^{-4}	11.87
0009	1.34×10^{-3}	1.19×10^{-3}	1.18×10^{-3}	6.25
0012	2.38×10^{-3}	2.48×10^{-3}	2.48×10^{-3}	3.16
0018	5.36×10^{-3}	5.49×10^{-3}	5.69×10^{-3}	1.37

Table 5.4: Comparison of the geometrical and mean-flow characteristics obtained using XFOIL for the four NACA aerofoils considered to validate experimentally the semi-analytical method.

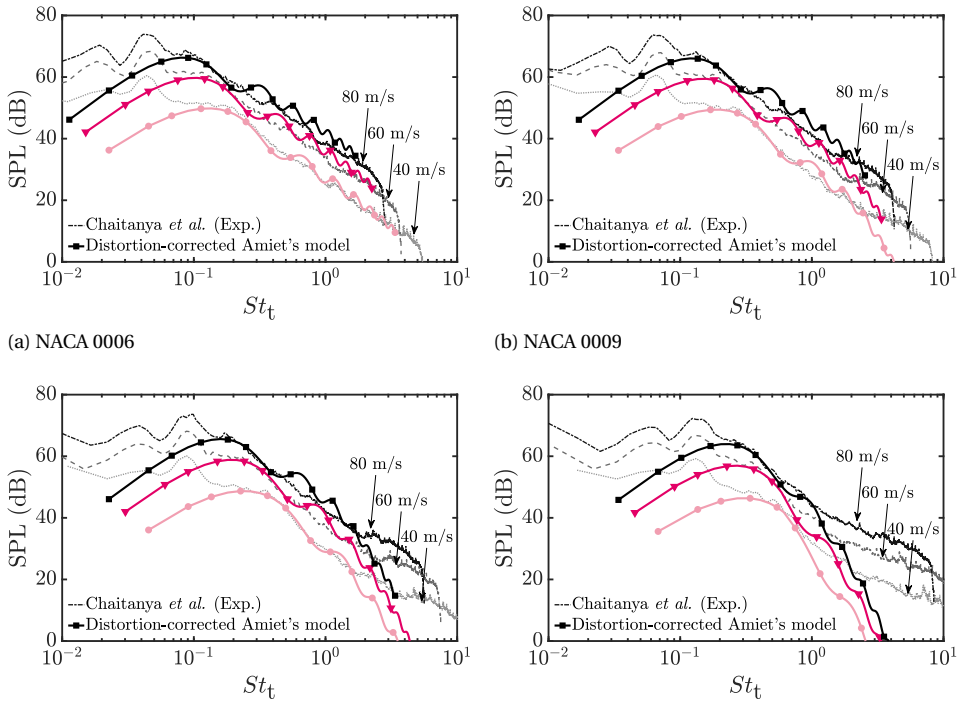

(a) NACA 0006

(b) NACA 0009

(c) NACA 0012

(d) NACA 0018

Figure 5.8: Sound pressure level calculated with Amiet's model corrected using the turbulence-distortion modelling methodology compared with experimental data from Chaitanya et al. [34] at different free-stream velocities. Amiet's model correction has been implemented using experimental turbulence characteristics and XFOIL data as input. The listener position is right above the leading edge ($R = 1.2\,\text{m}$, $\theta = \pi/2$), while the reference pressure to calculate the SPL is 2×10^{-5} Pa.

The comparison between the measured and predicted SPL above the leading edge ($R = 1.2\,\text{m}$, $\theta = \pi/2$) is shown in Fig. 5.8, while Fig. 5.9 reports the relative SPL (ΔSPL) with respect to that radiated by a flat plate. It is important to note that, in the case of the flat plate, the proposed corrected Amiet's model reduces to the canonical for-

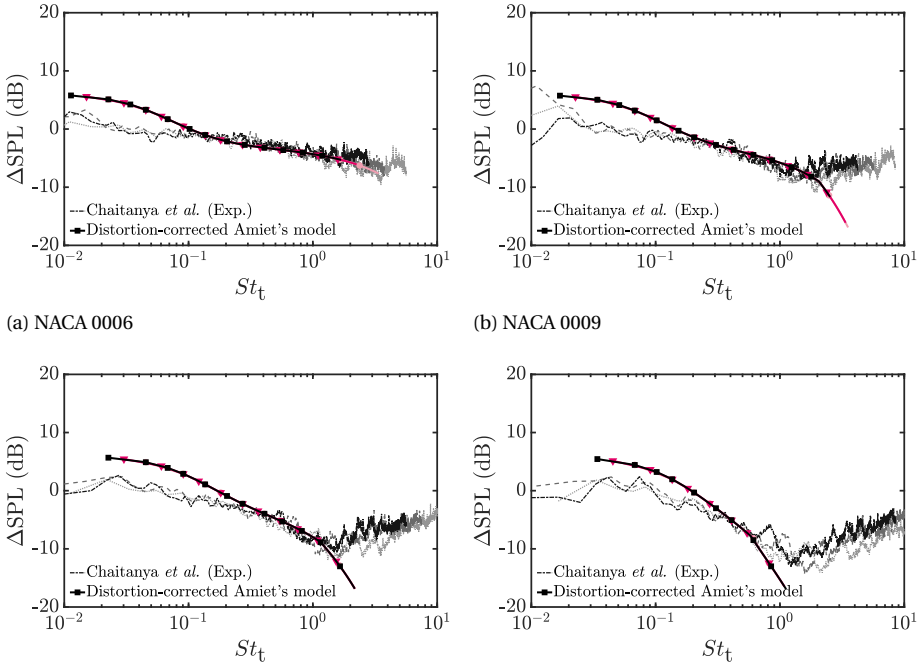

(a) NACA 0006 (b) NACA 0009

(c) NACA 0012 (d) NACA 0018

Figure 5.9: Difference in sound pressure level between the four aerofoils and a flat plate, calculated using Amiet's model corrected using the turbulence-distortion modelling methodology and compared with experimental data from Chaitanya et al. [34] at different free-stream velocities (refer to Fig. 5.8 for legend details). The listener position is right above the leading edge ($R = 1.2\,\text{m}, \theta = \pi/2$).

mulation. A very good agreement is observed for all aerofoil configurations and free-stream velocities considered, in the frequency range where leading-edge noise dominates ($St_t = [0.15, 1.5]$). For the NACA 0018, for which the application of the methodology is expected to lose validity ($L_1/a \simeq 1$, see Table 5.4), the agreement is still acceptable - the slope in the frequency range of interest is accurately captured - but not equally satisfactory. However, it is worth noting that the frequency range where leading-edge noise prevails is particularly narrow for this aerofoil due to the early onset of self-noise, as explained by Chaitanya et al. [34]. This characteristic complicates the comparison in this specific case.

This analysis demonstrates that the methodology proposed here is reliable across a wide range of aerofoil thicknesses, leading-edge radii, and free-stream velocities. This also applies in cases where the aerofoil introduces non-negligible disturbances, such as those associated with significant thickness or camber. Nevertheless, in these cases, additional analyses are still required to estimate the distortion length, related to the distribution of surface-pressure fluctuations, from geometric and mean-flow properties.

6

CHARACTERISATION AND MODELLING OF ROTOR INFLOW CONDITIONS

This chapter responds to the need identified in Chapter 1 to advance the state-of-the-art in low-fidelity modelling of turbulence-ingestion noise by enhancing the characterisation of inflow characteristics. This is achieved by proposing a modification to Amiet's model that allows pointwise flow measurements with local velocity information to be used as input. Indeed, the canonical formulation of Amiet's model relies on a three-dimensional turbulence input, which is notably difficult to measure and compute, both experimentally and numerically. Glegg et al. [128, 129] introduced a time-domain approach - not based on Amiet's theory - to pursue the same goal, but the model still requires measuring the four-dimensional velocity correlation function in the rotor plane, which is not always feasible. Similar limitation affect the prediction method developed by Brooks and Burley [130] for blade-wake interaction (BWI) noise, which is based on the measured leading-edge surface pressures as input. By retaining Amiet's frequency-based framework and reducing the three-dimensional turbulence input to a one-dimensional form, this study enables the use of hot-wire measurements as input in experimental configurations or pointwise acquisitions in numerical simulations. This formulation makes the model a simple yet effective hybrid tool for estimating acoustic performance and assessing inflow effects in complex configurations where sophisticated measurements are impractical and inflow modelling is unavailable. Additionally, it enables the application of turbulence-distortion models developed for rectilinear motion to rotors, such as the one presented in 5, potentially improving predictions in configurations where the distortion due to leading-edge bluntness is significant.

The analytical modification to Amiet's model for turbulence-ingestion noise prediction in rotors is presented in 6.1 and validated in 6.2 with the results of the experimental campaign of the two-bladed propeller detailed in Chapter 3. The proposed methodology is finally applied using hot-wire measurements as in Section 6.3.

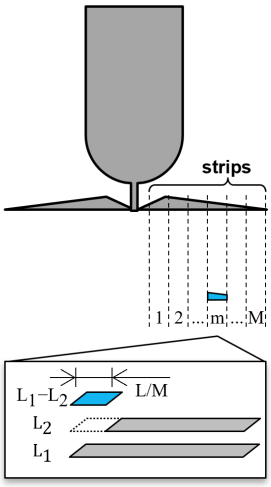

Figure 6.1: Sketch of the application of the inverse strip theory approach for the calculation of the blade instantaneous sound emission.

6.1. ANALYTICAL FORMULATION OF AMIET'S MODEL MODIFICATION

The modification of Amiet's model proposed in the present study consists in converting the three-dimensional spectrum $\Phi_{33}\left(K_1, K_2, K_3^{(n)}\right)$ in Eq. (2.33) into a one-dimensional one $\Theta_{33}(K_1)$. This is achieved by applying a strip-theory approach [131], which models the noise produced by a blade of span L as the summation of the noise contributions generated by M narrow spanwise portions of the blade, referred to as *strips*. The present procedure implements the theory in its inverse formulation, as done by Kücükcoskun [132], in which the noise emitted by a blade strip is calculated as the difference of the sound produced by two very large-span blades whose difference in width is equal to the strip width L/M itself, as shown in the conceptual sketch of the inverse strip theory approach reported in Fig. 6.1. For the present case, this is expressed considering $S'_{pp}\left(\mathbf{x}_\mathrm{B}, \omega_0, \gamma\right)$ as the noise emitted by the strip m, which is therefore obtained through

$$S'_{pp}\left(\mathbf{x}_\mathrm{B}, \omega_0, \gamma\right)\Big|_m = \left(S'_{pp}\left(\mathbf{x}_\mathrm{B}, \omega_0, \gamma\right)\Big|_{L_1} - S'_{pp}\left(\mathbf{x}_\mathrm{B}, \omega_0, \gamma\right)\Big|_{L_2}\right)\Big|_m, \tag{6.1}$$

with $L_1 - L_2 = L/M$ and $L_1, L_2 \to \infty$.

The overall noise produced is hence computed by applying Amiet's model M times, one for each blade considering local inflow conditions. By using Eqs. (2.29) and (2.33), all the contributions are summed through

$$S_{pp}\left(\mathbf{x}_\mathrm{B}, \omega_0\right) = B \sum_{m=1}^{M} S_{pp}\left(\mathbf{x}_\mathrm{B}, \omega_0\right)\Big|_m, \tag{6.2}$$

with B indicating the number of blades. The application of the inverse strip theory does

not involve any assumption or modification of the turbulence term: the analytical spectrum selected to describe the inflow will be scaled through the local turbulence characteristics regardless of its form.

The substitution of $\Phi_{33}(K_1, K_2, K_3^{(n)})$ with $\Theta_{33}(K_1)$ in Eq. (2.33) can be carried out considering the work of Wilson [133], who calculated the three-dimensional correlations and spectral functions in the case of homogeneous isotropic turbulence. Indeed, considering a generic three-dimensional reference system x_1, x_2, and x_3 with corresponding wavenumbers k_1, k_2, and k_3, the three-dimensional turbulence spectrum of the u_3 velocity component $\Phi_{33}(k_1, k_2, k_3)$ is obtained as the Fourier transform with respect to k_3 of the two-dimensional cross-spectrum $R_{33}(k_1, k_2; x_3)$

$$\Phi_{33}(k_1, k_2, k_3) = \frac{1}{2\pi}\int_{-\infty}^{+\infty} R_{33}(k_1, k_2; x_3)\, \mathrm{e}^{-\mathrm{i}x_3 k_3}\, \mathrm{d}k_3. \tag{6.3}$$

Starting from the analytical expression of Φ_{33} valid in the case of homogeneous isotropic turbulence, Wilson [133] explicitly calculated $R_{33}(k_1, k_2; x_3)$ as

$$R_{33}(k_1, k_2; x_3) = \frac{\overline{u_1'^2} k_h^2 L_3^4 \zeta_h^{\nu+2}}{\pi 2^{\nu+1}\Gamma(\nu)\left(1 + k_h^2 L_3^2\right)^{\nu+2}} \mathscr{B}_{\nu+2}(\zeta_h), \tag{6.4}$$

with $k_h^2 = k_1^2 + k_2^2$, $\zeta_h = (x_3/L_3)\sqrt{1 + k_h^2 L_3^2}$, $\mathscr{B}_{\nu+2}$ being the Bessel's function of the second kind of order $\nu + 2$. and ν setting the generic power law dependence in the inertial subrange.

For $x_3 = 0$, $R_{33}(k_1, k_2; x_3)$ can be seen as the two-dimensional wavenumber spectrum $\Psi_{33}(k_1, k_2)$, and Eq. (6.4) simplifies into

$$\Psi_{33}(k_1, k_2) = \frac{\nu(\nu+1)\,\overline{u_1'^2} k_h^2 L_3^4}{\pi\left(1 + k_h^2 L_3^2\right)^{\nu+2}}. \tag{6.5}$$

Using Eq. (6.5), Eq. (6.4) can be rewritten as

$$R_{33}(k_1, k_2; x_3) = \left[\frac{1}{\nu(\nu+1)} \frac{\zeta_h^{\nu+2}}{2^{\nu+1}\Gamma(\nu)} \mathscr{B}_{\nu+2}(\zeta_h)\right] \Psi_{33}(k_1, k_2) = A(k_1, k_2; x_3)\, \Psi_{33}(k_1, k_2), \tag{6.6}$$

with the auxiliary function $A(k_1, k_2; x_3)$ introduced to indicate the terms in square brackets.

This relationship between the two-dimensional cross-spectrum and the two-dimensional wavenumber spectrum (Eq. (6.6)) can be used to modify the turbulence term of Eq. (2.33). Indeed, it is possible to write

$$\Phi_{33}\left(K_1, K_2, K_3^{(n)}\right) = \mathscr{F}\left\{R_{33}\left(K_1, K_2; Z^{(n)}\right)\right\} = \frac{1}{2\pi}\int_{-\infty}^{\infty} R_{33}\left(K_1, K_2; X_3^{(n)}\right) \mathrm{e}^{-\mathrm{i}x_3^{(n)} K_3^{(n)}}\, \mathrm{d}K_3^{(n)}, \tag{6.7}$$

with $X_3^{(n)}$ indicating a fictitious spatial coordinate corresponding to the wavenumber $K_3^{(n)}$ and $\mathscr{F}$ representing the Fourier transform operator. By applying Eq. (6.6) to the

present case, and moving the two-dimensional wavenumber spectrum outside the Fourier transform operator, it follows that

$$\Phi_{33}\left(K_1, K_2, K_3^{(n)}\right) = \mathscr{F}\left\{A\left(K_1, K_2; X_3^{(n)}\right)\Psi_{33}\left(K_1, K_2\right)\right\} = \Psi_{33}\left(K_1, K_2\right)\tilde{A}\left(K_1, K_2, K_3^{(n)}\right), \quad (6.8)$$

with A indicating the auxiliary function allowing the conversion of the turbulence term from three-dimensional to two-dimensional and $\tilde{A}$ its Fourier transform. However, rather than performing the Fourier transform of A, $\tilde{A}$ can be conveniently obtained as

$$\tilde{A}\left(K_1, K_2, K_3^{(n)}\right) = \frac{\Phi_{33}\left(K_1, K_2, K_3^{(n)}\right)}{\Psi_{33}\left(K_1, K_2\right)}, \quad (6.9)$$

considering that, under the assumption of homogeneous isotropic turbulence, analytical expressions exist for Φ_{33} and Ψ_{33}. Since any axial dependence has now been removed from the turbulence velocity spectrum, the auxiliary function $\tilde{A}\left(K_1, K_2, K_3^{(n)}\right)$ can be defined as *axial correlation length*.

Owing to von Kármán's assumptions and framework for homogeneous isotropic turbulence [134], ν is finally considered equal to 1/3, resulting in Kolmogorov's $-5/3$ power law, and the three-wavenumber spectrum of the upwash velocity component with respect to the blade, i.e. corresponding to the axial velocity component in the present reference frame, reads

$$\Phi_{33}\left(k_1, k_2, k_3\right) = \frac{E\left(k\right)}{4\pi k^2}\left(1 - \frac{k_3^2}{k^2}\right), \quad (6.10)$$

with

$$E\left(k\right) = \frac{55}{9\sqrt{\pi}}\frac{\Gamma\left(5/6\right)}{\Gamma\left(1/3\right)}\frac{\overline{u_3'^2}}{k_e}\frac{k}{\left[1 + \left(\frac{k}{k_e}\right)^2\right]^{\frac{17}{6}}}. \quad (6.11)$$

The expression of the two-wavenumber spectrum of the same velocity component is then

$$\Psi_{33}\left(k_1, k_2\right) = \frac{4}{9\pi}\frac{\overline{u_3'^2}}{k_e^2}\frac{\left(\frac{k_1}{k_e}\right)^2 + \left(\frac{k_2}{k_e}\right)^2}{\left[1 + \left(\frac{k_1}{k_e}\right)^2 + \left(\frac{k_2}{k_e}\right)^2\right]^{\frac{7}{3}}}, \quad (6.12)$$

leading to the following expression for $\tilde{A}\left(K_1, K_2, K_3^{(n)}\right)$:

$$\tilde{A}\left(K_1, K_2, K_3^{(n)}\right) = \left(\frac{55}{16}\frac{L_3}{\pi}\right)\frac{\left(1 + \hat{k}_h^2\right)^{\frac{7}{3}}}{\left(1 + \hat{k}^2\right)^{\frac{17}{6}}}. \quad (6.13)$$

The last step consists of turning the two-dimensional wavenumber spectrum Ψ_{33} into the product of a one-dimensional spectrum Θ_{33} and another auxiliary function. As shown in Chapter 2, this has been done by Amiet [16] for his formulation for an aerofoil

in rectilinear motion under the assumption of large span. This is a reasonable assumption considering that the inverse approach of the strip theory considers the sound as produced by an aerofoil of infinite span. It is hence possible to write

$$\Psi_{33}(K_1, K_2) = \frac{1}{\pi}\Theta_{33}(K_1)\, l_2(K_1), \tag{6.14}$$

with $l_2(K_1)$ being the spanwise coherence length of the upwash velocity component, for which Amiet [16] proposes the following expression

$$l_2(K_1) = \frac{8L_3}{3}\left[\frac{\Gamma(1/3)}{\Gamma(5/6)}\right]^2 \frac{\hat{K}_3^2}{\left(3+8\hat{K}_3^2\right)\sqrt{1+\hat{K}_1^2}}. \tag{6.15}$$

This formulation, which incorporates the one-dimensional turbulence term and the spanwise coherence length, is valid for a listener positioned in the midspan plane of a blade in rectilinear motion. However, as will be shown in Section 6.2, this modification does not impact the accuracy of noise directivity compared to the canonical implementation of Amiet's model.

The introduction of the axial correlation length $\tilde{A}\left(K_1, K_2, K_3^{(n)}\right)$ and the spanwise coherence length $l_2(K_1)$ allows hence the turbulence term to be expressed in terms of the one-dimensional spectrum $\Theta_{33}(K_1)$, finally converting Eq. (2.33) (applied to the m-th strip) into

$$S_{pp}\left(\mathbf{x}_\mathrm{B}, \omega_\mathrm{B}, \gamma\right)\Big|_m = G\left|\mathscr{L}(K_1, K_2, M_1)\right|^2 \left(\frac{1}{\pi}\Theta_{33}(K_1)\, l_2(K_1)\right) \sum_{n=-\infty}^{\infty} \tilde{A}\left(K_1, K_2, K_3^{(n)}\right) \frac{2\pi}{\left(\frac{c}{2}\right)^2 \overline{u_3'^2} X_3}. \tag{6.16}$$

The one-dimensional spectrum can be modeled using a von Kármán spectrum

$$\Theta_{33}(K_1) = \frac{2}{27\sqrt{\pi}}\frac{\Gamma(5/6)}{\Gamma(7/3)}\frac{\overline{u_3'^2}}{k_e}\frac{3+8\left(K_1/k_e\right)^2}{\left[1+\left(K_1/k_e\right)^2\right]^{\frac{11}{6}}}, \tag{6.17}$$

with $k_e = \sqrt{\pi}/L_3\Gamma(5/6)/\Gamma(1/3)$. This implementation, whose validation is presented in Section 6.2, only requires the knowledge of the turbulence intensity, free-stream velocity, and integral length scale. Alternatively, it is possible to use a direct probe measurement in the frequency domain as input, such as that obtained by means of HWA, as in Section 6.3.

6.2. VALIDATION WITH EXPERIMENTAL DATA

The proposed modification is validated using acoustic measurements from the experimental set-up featuring the two-bladed propeller interacting with grid-generated turbulence (detailed in Chapter 3). Amiet's model has been applied using the radial distribution of flow characteristics sampled far upstream at the nozzle exit in the configuration without the propeller (see Section 3.3). Comparisons between the predictions

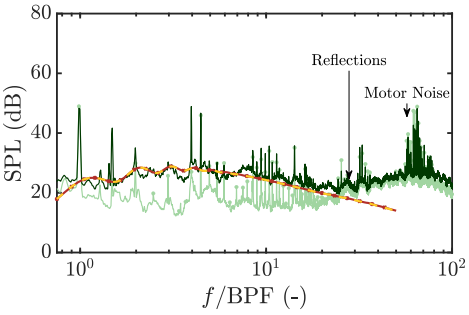

(a) $\Omega = 4000$ RPM, $\theta = \pi/3$ (mic. 1)

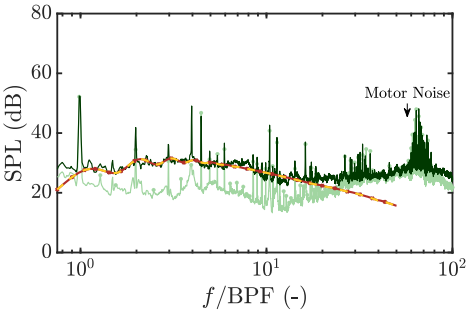

(b) $\Omega = 4000$ RPM, $\theta = 13\pi/18$ (mic. 8)

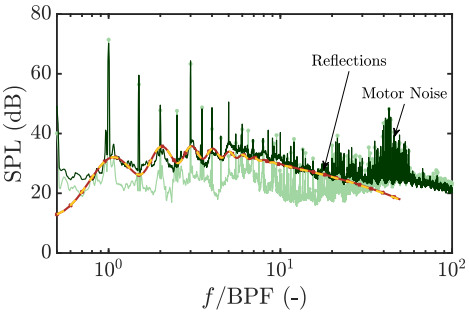

(c) $\Omega = 6000$ RPM, $\theta = \pi/3$ (mic. 1)

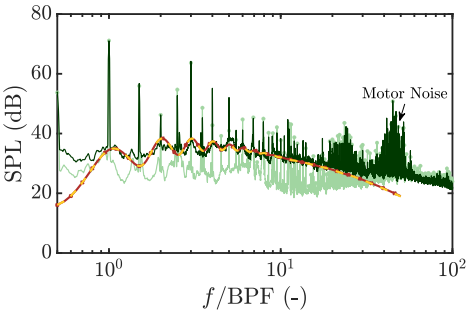

(d) $\Omega = 6000$ RPM, $\theta = 13\pi/18$ (mic. 8)

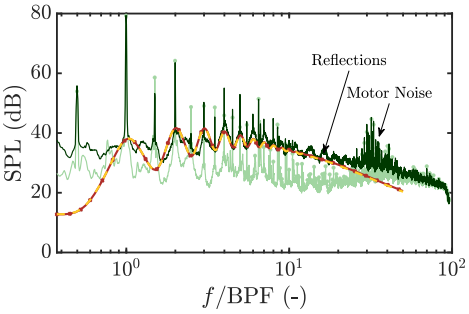

(e) $\Omega = 8000$ RPM, $\theta = \pi/3$ (mic. 1)

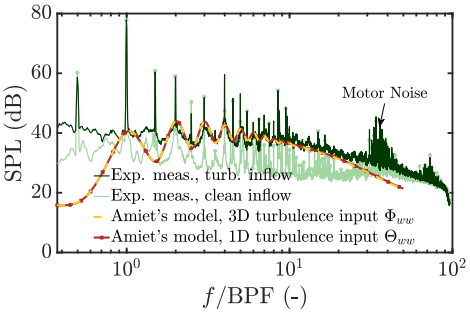

(f) $\Omega = 8000$ RPM, $\theta = 13\pi/18$ (mic. 8)

Figure 6.2: Sound pressure level predicted by Amiet's model with 3D and 1D turbulence input compared to experimental measurements with turbulent and clean inflow at the three rotational speeds and at two different microphone positions. The reference pressure used to calculate the SPL is 2×10^{-5} Pa.

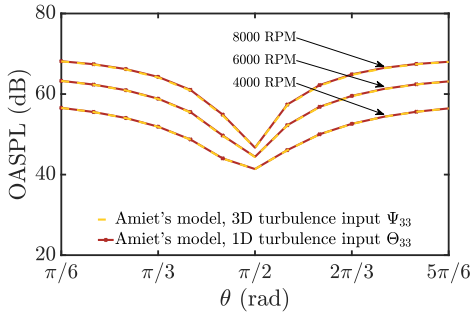

Figure 6.3: Overall sound pressure level predicted by Amiet's model with 3D and 1D turbulence for the angular range $\theta = [\pi/6, 5\pi/6]$ at 4000 RPM, 6000 RPM, and 8000 RPM. The reference pressure used to calculate the SPL is 2×10^{-5} Pa.

and the measurements are reported in terms of SPL in Fig. 6.2 for 4000 RPM, 6000 RPM, and 8000 RPM, respectively. For each case, the experimental measurements with both turbulent and clean inflow are presented, with listener positions considered at $\pi/3$ and $13\pi/18$. Background noise, omitted from the figures for clarity, was verified to be well belo the propeller noise levels in both inflow cases.

Amiet's model has been implemented in two formulations featuring the three-dimensional turbulence spectrum Φ_{33} and the one-dimensional one Θ_{33}. These have been modeled using the von Kármán expressions given in Eq. (6.10) and Eq. (6.17), respectively. Both have been applied with the inverse strip theory approach, retaining the B2B correlation modelling. This comparison allows possible effects resulting from the modification of the turbulence term to be identified.

Turbulence-ingestion noise dominates the sound spectra in the low- and mid-frequency range, approximately up to the 20-th - 30-th BPF [135], as can be seen from the cases at 4000 RPM and 6000 RPM with respect to the clean inflow configuration. At higher frequencies, up to the 100-th BPF, the spectra feature a clear bump with tones concentrated between the 40-th and the 70-th BPF. These are clearly caused by the propeller motor, as indicated in the plots with an arrow, while the bump can likely be attributed to the blade self-noise and laminar separation [136, 137]. The bump in the high-frequency range can hardly be recognised for the case at 8000 RPM, as the noise levels related to turbulence-ingestion noise increase significantly in this rotation regime.

In general, the acoustic spectra exhibit clear signs of reflections, most likely originating from the nozzle, nacelle, or support rig. These reflections primarily affect the high-frequency range beyond the 10-th BPF, introducing “saw-tooth" peaks in the spectra. These peaks, particularly evident for the listener position at $\pi/3$ and marked in the plots with an arrow, should not be confused with the haystacking features in the low- and mid-frequency ranges. Indeed, here the far-field acoustic spectra exhibit distinct broadband characteristics along with quasi-tonal peaks resulting from B2B correlation. As expected, the prominence of these narrow peaks and the frequency range over which they appear increase with rotational speed. This occurs because, at higher speeds, turbulent eddies are more likely to be chopped by multiple blades.

Regarding the low-fidelity prediction, the two formulations of Amiet's model retrieve

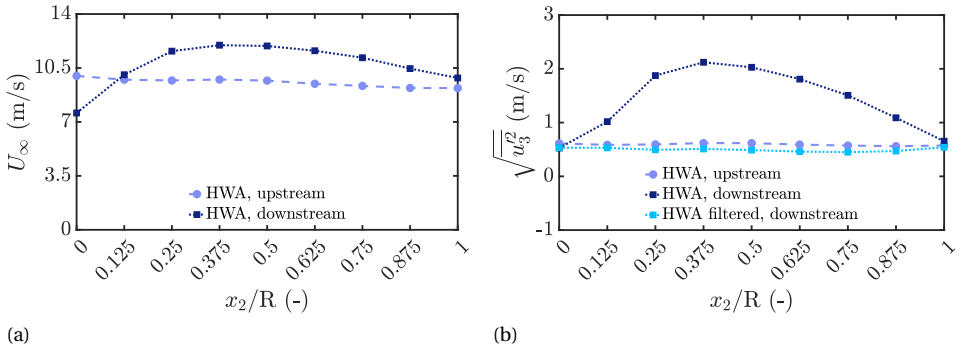

Figure 6.4: Radial distributions far upstream at x_3/R = 1.000 and near the rotor plane at x_3/R = 0.050 (in the filtered and non-filtered cases) for the (a) time average and (B) root-mean-square of the axial velocity component measured using HWA.

nearly identical results at 4000 RPM, 6000 RPM and 8000 RPM. Only a slight difference, seemingly proportional to the rotational speed, becomes noticeable at frequencies above the 10-th BPF. Specifically, the curve corresponding to the original implementation of Amiet's model with the three-dimensional turbulence spectrum lies slightly below that of the modified approach using the one-dimensional spectrum. The match between the two formulations is confirmed by the directivity plots in Fig. 6.3. These show the OASPL calculated in the frequency range where turbulence-ingestion noise dominates (f = [0.1BPF – 30BPF]). Experimental measurements have not been included, as microphone data is dominated by other flow-induced noise sources in the angular range where turbulence-ingestion noise directivity decreases. As a result, these additional noise contributions would hinder a meaningful comparison.

The exact agreement between Amiet's model in its original formulation with the three-dimensional spectrum and the modified approach using a one-dimensional turbulence input serves as a validation of the proposed methodology. At the same time, both predictions closely match the experimental SPL, accurately capturing both the broadband and quasi-tonal components within the low-fidelity framework. The tonal peaks at BPF harmonics are not captured as the turbulence input term in Amiet's model does not include the description of this contribution.

6.3. APPLICATION OF THE METHODOLOGY WITH HOT-WIRE MEASUREMENTS AS INPUT

The formulation with the one-dimensional turbulence term is applied for the case at 6000 RPM using the velocity frequency spectra obtained from the HWA measurements as input. The probe specifically measures velocity fluctuations in the axial direction, as explained in Section 3.3, which corresponds to the upwash component relative to the rotor plane. This velocity component is responsible for inducing the unsteady loading on the blades, meaning that this measurement can be rightfully used as input in the low-fidelity model.

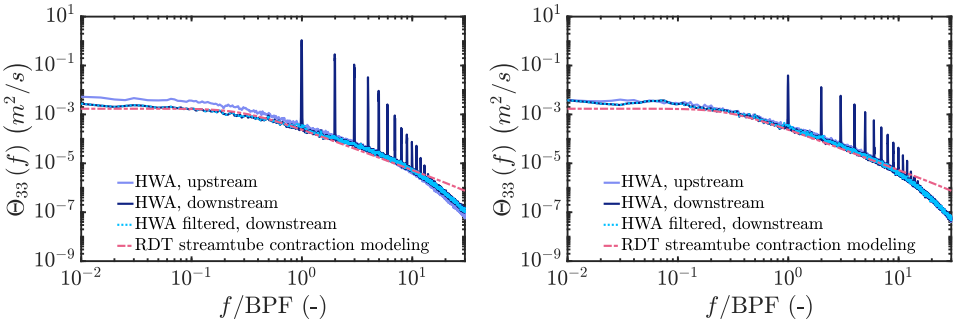

(a) Mid-span radial position (x_2/R = 0.500)

(b) Tip radial position (x_2/R = 1.000)

Figure 6.5: Frequency spectra of the inflow velocity at the radial positions (a) x_2/R = 0.500, and (B) x_2/R = 1.000. The spectra sampled far upstream at x_3/R = 1.000 and near the rotor plane at x_3/R = 0.050 (in the filtered and non-filtered cases) are compared with the altered spectrum modelled by the RDT from upstream flow conditions.

6.3.1. TURBULENT INFLOW CHARACTERIZATION

Figure 6.4 presents the radial distributions of the time-averaged velocity and the root-mean-square of the velocity component measured with HWA. The distributions sampled far upstream at x_3/R = 1.000 (indicated in the figure with “upstream") are compared to those measured near the rotor plane at x_3/R = 0.050 (indicated with “downstream"). For the latter, the root-mean-square is reported both for the original signal and after filtering out tonal components caused by blade passage. The filtering is performed using an in-house peak detection algorithm applied to the PSDs of the HWA signals.

While the time-averaged velocity increases relative to upstream conditions, the removal of tonal components reveals a slight decrease in axial velocity fluctuations compared to upstream conditions. This effect is due to the streamtube contraction, which, as it stretches the turbulent structures in the streamwise direction, causes a simultaneous reduction in the streamwise velocity fluctuation, similar to what occurs in the convergent section of a wind tunnel [22, 47].

Figure 6.5 compares the HWA velocity spectra for the 2 sampling positions along the axial direction and for 2 different radial positions, x_2/R = 0.500 and x_2/R = 1.000. The plot also presents the filtered HWA velocity spectra sampled at the rotor plane, with the tones removed.

The HWA spectra sampled close to the rotor plane present lower levels in the low-frequency range (approximately up to f/BPF $\simeq$ 0.6). This is especially evident at the central radial locations, whereas positions near the rotor axis and towards the blade tip exhibit upstream and downstream spectra that almost perfectly overlap. This behaviour is attributed to the reduction in streamwise velocity fluctuations due to streamtube contraction, as observed in the root-mean-square variation. This variation can be calculated from upstream conditions using RDT, as done by Majumdar and Peake [70] and Simonich et al. [67]. An implementation of Goldstein’s formulation [71] has been implemented here following the approach of Glegg and Devenport [138] for the axysimmetric contraction, with the predicted altered spectra reported in Fig. 6.5 together with the

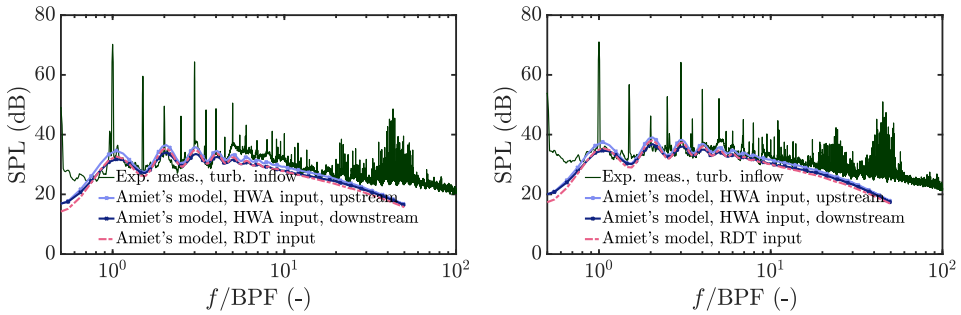

Figure 6.6: Sound pressure level predicted by Amiet's model applied using HWA spectra sampled far upstream ($x_3/\mathrm{R} = 1.000$) and near the rotor plane ($x_3/\mathrm{R} = 0.050$) compared to experimental measurements at $\Omega = 6000\,\mathrm{RPM}$ for (a) $\theta = \pi/3$ (microphone 1) and (B) $\theta = 13\pi/18$ (microphone 8). The comparison includes the prediction using the altered velocity spectrum from the RDT as input. The reference pressure used to calculate the SPL is 2×10^{-5} Pa.

HWA ones. Good agreement is observed between the RDT results and the experimental measurements at $x_3/\mathrm{R} = 0.050$, demonstrating how simple pointwise measurements can effectively describe the inflow conditions and their alteration. The impact of this alteration will become evident in the application of the modified Amiet's model using directly probe measurements as input.

6.3.2. NOISE PREDICTION

To correctly incorporate HWA measurements into the low-fidelity model, an appropriate conversion into a spatial wavenumber spectrum is required. This conversion relies on Taylor's hypothesis, which considers frozen turbulence, as also assumed by Amiet [16, 73]. By assuming the convective velocity to be equal to the inflow velocity U_∞, the spectrum $\Theta_{33}(K_1)$ used in Amiet's model can be derived from the experimental frequency spectrum through

$$\Theta_{33}(K_1) = \frac{U_\infty}{2\pi}\Theta_{33}(f)\Big|_{\mathrm{HW}}. \tag{6.18}$$

The advantage of using pointwise flow measurements as input is assessed by comparing the predictions obtained with the spectra sampled far upstream ($x_3/\mathrm{R} = 1.000$) and very close to the rotor plane ($x_3/\mathrm{R} = 0.050$), shown in Fig. 6.6. The modified Amiet's model has been implemented using the respective radial distributions of the time-average and root-mean-square of the axial velocity component shown in Fig. 6.4. The plot compares the low-fidelity predictions with the experimental acoustic measurements at the angular positions $\theta = \pi/3$, and $\theta = 13\pi/18$. An accurate result is obtained using the HWA frequency spectra as input on the whole frequency range where turbulence-ingestion noise dominates, proving the validity of the proposed approach.

As expected, the alteration undergone by turbulence as it approaches the rotor due to the streamtube contraction leads to different results in the prediction. The implementation of Amiet's model with the velocity spectrum sampled far upstream yields

a slight overprediction in the low-frequency range. In contrast, the velocity spectrum sampled near the rotor plane leads to a more accurate prediction in this frequency range. Such an effect plays a significant role in cases for which the variation of section of the streamtube is particularly pronounced, as in hovering conditions or high-speed rotation regimes. Figure 6.6 also shows Amiet's model implemented with the distorted spectrum obtained through RDT, which closely matches the prediction obtained using the downstream HWA spectra as input. This analysis demonstrates how the modified Amiet's model can be used to evaluate the impact of the inflow conditions on the acoustic spectra through direct HWA measurements.

7

CONCLUSIONS AND FUTURE WORKS

This research study has provided a comprehensive physical and analytical characterisation of turbulence-distortion effects to improve the low-fidelity prediction of turbulence-interaction noise. The conclusions of this work are presented below and are organised into two parts: the first provides a summary of the main findings of each chapter of the manuscript, which mirrors the conceptual structure of the project described in Chapter 1, with the most important takeaway explicitly highlighted; the second reports open questions and proposes directions for future research and development.

7.1. OVERVIEW AND DISCUSSION

1. **PHYSICAL ANALYSIS**: **description of turbulence distortion mechanism in the case of aerofoil of non-negligible thickness and assessment of the impact on noise generation and prediction.**

   Turbulence distortion, related to aerofoil bluntness, causes an alteration of the velocity field in the stagnation region, which affects unsteady surface pressure and noise generation.

   A physical investigation of leading-edge noise generation for aerofoil geometries has been carried out numerically to enhance the accuracy of low-fidelity methods. The characteristics of turbulence distortion have been analysed with a focus on the aerofoil-geometry effects.

   The analysis has shown that, as the leading edge is approached, the progressive alteration of the velocity field results in an exponential decay of the upwash velocity spectrum at the stagnation point in the high-frequency range. This exponential decay, consistent with the analytical findings of the RDT linearised theory of Hunt [45], also characterises the high-frequency behaviour of surface-pressure spectra near the stagnation point, suggesting that noise is produced by a pressure distribution induced by the distorted velocity field in the vicinity of the leading edge.

Noise-generation efficiency, quantified in terms of surface-pressure fluctuations, has been shown to be related to aerofoil curvature by means of the intensity of the pressure gradient along the leading edge. Indeed, the arc length l_{dis} extending from the stagnation point to the position of maximum curvature variation, which corresponds to the space available for the turbulent structures to accelerate along the aerofoil leading edge, is found to be the geometrical parameter dictating the turbulence-distortion mechanism. This finding legitimates the extension of the results of the RDT to aerofoil geometries. In addition, this approach defines a shift in perspective for determining the reference geometric parameter for turbulence distortion. This should be regarded not as a measure of obstacle dimensions, such as the thickness or leading-edge radius proposed so fa, but rather as a parameter related to flow acceleration and streamline deflection, in line with the concept of drift used by Lighthill [83], Hunt [45], and Goldstein [71].

The effects of turbulence distortion on the noise prediction are assessed by using as input in Amiet's model an upwash velocity spectrum acquired very close to the stagnation point and by accounting for the gust-amplitude variation with respect to upstream undistorted conditions in the aeroacoustic transfer function. Such a deviation is caused by the higher amplitude of the distorted gust, related to the increase of the root-mean-square of the upwash velocity component in the stagnation, which is not taken into account in the flat-plate-based formulation employed for the transfer function. An overall good agreement in terms of PWL and directivity patterns of the far-field noise is obtained in the whole frequency range of interest, especially in terms of trend and decay slope.

The proposed approach suggests a promising and more robust development for the characterisation of the aerofoil-geometry effects in low-fidelity noise-prediction methods by proving that the aerofoil-geometry effects are fully encompassed by modifying the input term describing the turbulence characteristics. This conclusion entails the evaluation of the frequency spectrum of the upwash turbulent velocity as close as possible to the stagnation point, allowing the high-frequency decay characterising the surface-pressure spectra at the leading edge to be correctly captured.

This enhanced understanding constitutes a significant step forward in improving the accuracy of the leading-edge noise-prediction methods. This indeed paves the way for developing analytical methodologies that predict the alteration of the flow field in the stagnation region knowing the upstream, undistorted turbulence characteristics and the aerofoil geometrical features and hence extend the applicability of Amiet's model.

2. **ANALYTICAL MODELLING: development of an analytical framework to incorporate turbulence-distortion effects into low-fidelity noise prediction tools.**

   Turbulence-distortion effects should be considered at stagnation point to enhance low-fidelity prediction. This could be done by using RDT asymptotic results starting from upstream undistorted flow conditions.

   An analytical methodology has been proposed in Chapter 5 to enhance the accur-

acy of Amiet's model for leading-edge noise prediction in the case of realistic aerofoil geometries by including and modelling the effects of turbulence distortion on the alteration of the velocity field and on the acoustic response.

These effects have been predicted using RDT asymptotic results, resulting in a methodology that requires as inputs only the turbulence integral length scale and intensity of the upstream undistorted flow and the equivalent RDT characteristic length for aerofoil configurations.

The characterisation of the distorted velocity field entails the modelling of the alteration of the frequency spectrum and the spanwise coherence length of the upwash velocity component. The identification of the distortion length has allowed the distorted spectrum of the upwash velocity component to be modelled by interpolating the RDT asymptotic expressions for the alteration of the velocity spectra in the low and the high-wavenumber ranges.

The alteration of spanwise coherence length in the distorted region of the flow field, characterised by an increase in the low-frequency range, has been modelled accounting for the variation of the length scale of the upwash velocity component, which doubles with respect to upstream conditions.

Regarding the turbulence-distortion effects on the acoustic response, the aeroacoustic transfer function has been corrected to account for the variation of the energy content of the perturbation, following the findings of the physical analysis. The required scaling has been implemented using the RDT expression modelling the variation of the variance in the asymptotic case of large-scale turbulence. Remarkably, this result shows that the flat-plate analytical formulation of the aeroacoustic transfer function can be retained for thicker aerofoil geometries once turbulence-distortion effects are taken into account.

This methodology has been validated by applying it to correct Amiet's model for four numerical simulations and four experimental configurations. The numerical simulations involve a NACA 0012, NACA 0012-103, and NACA 4412 at two different loading conditions, while the experimental configurations include a NACA 0006, NACA 0009, NACA 0012, and NACA 0018 at three different free-stream velocities. In the latter case, the distortion length was estimated using XFOIL. An accurate far-field noise prediction was retrieved whenever the methodology was applied within its validity range $L_1/a > 1$.

In light of the above, it can be concluded that the proposed methodology, based on the preservation of Amiet's model original formulation and the incorporation of the RDT asymptotic results, offers a valid approach for improving the accuracy of low-fidelity leading-edge noise predictions in realistic aerofoil geometries.

3. **FULL-SCALE APPLICATION: establishment of the physical and analytical framework needed to evaluate the impact of these advancements in the context of rotational motion.**

   Amiet's model modification in rotors enables the evaluation of the impact of inflow conditions on noise generation and prediction in complex configurations and paves

the way for the application of turbulence-distortion models developed for rectilinear motion.

A modification to Amiet's model for turbulence-ingestion noise prediction in rotors is proposed to directly use probe measurements of the inflow conditions as inputs. This formulation enables the model to be applied to complex configurations with limited turbulence modelling and measurement availability. It is achieved by transforming the original three-dimensional turbulence spectrum used as input into a one-dimensional one. This conversion is made possible by using an inverse-strip theory approach and introducing two auxiliary functions, i.e. the axial and spanwise correlation length. The former describes the radial correlation of the velocity fluctuations perpendicular to the rotor plane, while the latter accounts for the blade-to-blade correlation.

The proposed methodology is validated using experimental measurements of a two-bladed propeller interacting with grid-generated turbulence at three different advance ratios. Good agreement is found between the experimental measurements and the modified Amiet's model at all the considered advance ratios.

The outcome is, hence, a formulation that configures Amiet's model as a modular tool, where the various contributions affecting the turbulence interacting with the rotor and the resulting noise scattering are represented by decoupled terms. This enables the individual investigation and modelling of each physical mechanism and its relative impact on noise generation. The inherent structure of the model makes it well-suited for complex configurations, as limited inflow measurements are required for its application.

Furthermore, in its current state, the proposed framework lays the ground for combining different models available in the literature to describe the successive phases of turbulence alteration as it approaches the rotor. For instance, the deformation due to the streamtube contraction can be taken into account through the RDT into the velocity spectrum term, while the multiple chopping of the elongated turbulent eddies is modelled through the axial correlation length. In addition, future developments could focus on characterising the interaction between the chopped elongated turbulent structure and the leading edge, e.g. through the methodology developed in 5, which can now be incorporated through the conversion of turbulence input into a one-dimensional spectrum. The potential to account for such a mechanism, particularly relevant for cases introducing significant flow disturbances, makes the proposed model especially well-suited for capturing the effects of blades with realistic shapes and complex rotor geometries.

7.2. OPEN QUESTIONS AND FUTURE WORKS

The results obtained in the thesis, together with the limitations identified, have highlighted several areas for further investigation and indicated potential directions for future development. These possible future works are outlined and briefly described in the list below.

- The distortion length l_{dis}, i.e. the characteristic geometric dimension of the aero-

foil introduced in Chapter 4 that influences the distortion of the incoming turbulence and determines the distortion mechanism, has been identified as the distance between the peaks of the root-mean-square of surface pressure fluctuations at the leading edge. For symmetric aerofoils, a correspondence has been established between this unsteady flow parameter, the pressure gradient, and the curvature variation. However, such a relationship, which would enable the calculation of this characteristic length without detailed knowledge of the flow field near the aerofoil, has not been identified for cambered aerofoils. Understanding this parameter is critical for applying the proposed turbulence-distortion correction to improve the accuracy of Amiet's model when dealing with aerofoils of non-negligible thickness. Therefore, a detailed analysis of cambered configurations at different loading conditions is warranted to develop a reliable procedure to determine this parameter.

- The investigation into the influence of aerofoil geometry and loading conditions on the distortion mechanism can be further extended and generalised. Building on the previously discussed shift in perspective, according to which turbulence distortion is attributed to the curvature of the streamlines rather than solely to the size of the obstacle, a twofold investigation could be pursued. First, an analytical study should aim to establish a quantitative relationship between streamline curvature, pressure fluctuations, and the resulting distortion of turbulent structures. Second, an extensive experimental campaign exploring a range of inflow conditions, aerofoil thicknesses, leading-edge radii, and angles of incidence would be essential to identify potential trends linking distortion length with noise reduction, thereby providing empirical support for the analytical findings.

- Arguably, the most significant outcome of this work is the finding that the effects of turbulence distortion on noise prediction can be fully encompassed by limiting modifications to Amiet's flat-plate-based model solely to the term representing the characteristics of the incoming turbulence. In this framework, the aeroacoustic transfer function only needs to be adjusted to correctly describe the energy content of the incoming gust when the distorted turbulence spectrum is used as input. However, the validity of this approach is limited to the case of large-scale turbulent structures. A detailed investigation is therefore required to understand how turbulence distortion and realistic aerofoil geometries influence the aerodynamic and acoustic response of the aerofoil. Such a study would enable the development of an enhanced and more general formulation of the aeroacoustic transfer function for thick aerofoil geometries, thereby improving the overall robustness of the methodology.

- Defining a general procedure to calculate the distortion length for a generic aerofoil, and potentially identifying a relationship between this parameter and the aerofoil geometry, would allow the application of the turbulence-distortion modelling methodology for the enhancement of Amiet's model as a reverse engineering tool. Ideally, a target noise level could be specified as an input, allowing the methodology to determine the corresponding distortion length and, consequently, the aerofoil section producing those acoustic emissions. For wind turbines or UAM rotors, this would enable the identification of the optimal blade section at each

radial position. This would transform the low-fidelity prediction model into an optimisation tool, ultimately leading to the design of wings or rotors that minimise turbulence-interaction noise.

- The validity of the proposed modification to Amiet's model for turbulence-ingestion noise prediction has been demonstrated only for axial-flight configuration, which is characterised by less pronounced distortion due to streamtube contraction. However, while currently focused on improving the description and modelling of the input turbulence term, the proposed modification broadens the potential of the model for new applications. Upon adequate validation or adaptation, the inherent structure of the model makes it indeed well suited for complex configurations, such as propellers in vortex-ring state, rotors ingesting boundary layers, contra-rotating propeller cases, and strongly anisotropic inflow conditions, as limited inflow measurements are required for its application. Targeted investigations are therefore necessary for each of these configurations to assess the robustness of the modified Amiet's model and to identify potential further refinements.

- In the case of rotors, the alteration of the incoming turbulence caused by the streamtube has been demonstrated to play a significant role in noise generation. This highlights the importance of accurately modelling this mechanism within low-fidelity prediction tools to ensure reliable estimates of acoustic emissions. The effect is expected to be particularly pronounced in wind turbines, where the variation in streamtube cross-section is more substantial than in propellers or engine rotors. The modification of Amiet's model presented in Chapter 6 outlines an analytical procedure to incorporate the turbulence-distortion modelling methodology to describe leading-edge distortion. However, in its current form, it does not account for the turbulence alteration caused by streamtube contraction. Therefore, a complete distortion-corrected version of Amiet's model could integrate two distinct methodologies to capture both mechanisms, in accordance with the modular framework established by the proposed modification. The turbulence alteration due to streamtube contraction can be described using RDT in Goldstein's formulation, which requires only the contraction ratio as input. Such a parameter can be obtained using a Blade Element Momentum Theory (BEMT) code, which, in turn, needs the rotor geometry and polars. In the specific case of wind turbines, where the streamtube is strongly divergent, additional considerations are needed to ensure the accurate application of RDT.

BIBLIOGRAPHY

[1] EEA. *Quiet areas in Europe — The environment unaffected by noise pollution*. Tech. rep. 2016.

[2] WHO. *Environmental noise guidelines for the European Region*. 2018.

[3] EEA. *Environmental noise in Europe — 2020*. Tech. rep. 2020.

[4] EU. *Directive 2002/49/EC of the European Parliament and of the Council of 25 June 2002 relating to the assessment and management of environmental noise - Declaration by the Commission in the Conciliation Committee on the Directive relating to the assessment and management of environmental noise*. 2002.

[5] EEA. *Study on airport noise reduction: final report*. Publications Office of the European Union, 2022. ISBN: 978-92-76-55622-0.

[6] ISO. *ISO 1996-2:1987*. 1987.

[7] European Commission et al. *Assessment of potential health benefits of noise abatement measures in the EU: Phenomena project*. Tech. rep. 2021.

[8] B. Peeters and R. Nusselder. *European Network of the Heads of Environment Protection Agencies (EPA Network)*. 2019.

[9] European Commission and Directorate General for Environment. *Communication from the Commission to the European Parliament, the Council, the European Economic and Social Committee and the Committee of the Regions: Pathway to a healthy planet for all – EU action plan: 'Towards zero pollution for air, water and soil'*. Tech. rep. 2021.

[10] S. Oerlemans. *Wind turbine noise: primary noise sources*. Tech. rep. NLR, 2011.

[11] EEA. *The NOISE Observation & Information Service for Europe*. 2023.

[12] EASA and EEA. *European aviation environmental report 2016*. Publications Office, 2016.

[13] S. Buck et al. *Experimental characterization of turbulent inflow noise on a full-scale wind turbine*. Journal of Sound and Vibration 385 (2016), pp. 219–238.

[14] S. Buck et al. *Experimental validation of a wind turbine turbulent inflow noise prediction code*. AIAA Journal 56 (2018), pp. 1495–1506.

[15] J. M. R. Graham. *Similarity rules for thin aerofoils in non-stationary subsonic flows*. Journal of Fluid Mechanics 43 (1970), pp. 753–766.

[16] R. K. Amiet. *Acoustic radiation from an airfoil in a turbulent stream*. Journal of Sound and Vibration 41 (1975), pp. 407–420.

[17] R. W. Paterson and R. K. Amiet. *Acoustic radiation and surface pressure characteristics of an airfoil due to incident turbulence*. In: *3rd Aeroacoustics Conference*. Palo Alto, CA, American Institute of Aeronautics and Astronautics, 1976.

[18] R. W. Paterson and R. K. Amiet. *Noise and surface pressure response of an airfoil to incident turbulence*. Journal of Aircraft 14 (1977), pp. 729–736.

[19] R. W. Paterson and R. K. Amiet. *Noise of a model helicopter rotor due to ingestion of turbulence*. Tech. rep. National Aeronautics and Space Administration, 1979.

[20] M. S. Howe. *Aerodynamic noise of a serrated trailing edge*. Journal of Fluids and Structures 5 (1991), pp. 33–45.

[21] S. Oerlemans. *Reduction of wind turbine noise using blade trailing edge devices*. In: *22nd AIAA/CEAS Aeroacoustics Conference*. Lyon, France, American Institute of Aeronautics and Astronautics, 2016.

[22] R. K. Amiet et al. *Rotor noise due to atmospheric turbulence ingestion. Part II - Aeroacoustic results*. Journal of Aircraft 27 (1990), pp. 15–22.

[23] C. Teruna et al. *Numerical investigation of leading edge noise reduction on a rod-airfoil configuration using porous materials and serrations*. Journal of Sound and Vibration 494 (2021), p. 115880.

[24] O. Amoiridis et al. *Sound localization and quantification analysis of an automotive engine cooling module*. Journal of Sound and Vibration (2021).

[25] P. Moriarty et al. *Recent improvement of a semi-empirical aeroacoustic prediction code for wind turbines*. In: *10th AIAA/CEAS Aeroacoustics Conference*. Manchester, UK, American Institute of Aeronautics and Astronautics, 2004.

[26] M. E. Goldstein and H. Atassi. *A complete second-order theory for the unsteady flow about an airfoil due to a periodic gust*. Journal of Fluid Mechanics 74 (1976), pp. 741–765.

[27] W. Olsen and J. Wagner. *Effect of thickness on airfoil surface noise*. AIAA Journal 20 (1982), pp. 437–439.

[28] H. Atassi et al. *Acoustic radiation from lifting airfoils in compressible subsonic flow*. In: *13th Aeroacoustics Conference*. Tallahassee, FL, American Institute of Aeronautics and Astronautics, 1990.

[29] D. P. Lockard and P. J. Morris. *Radiated noise from airfoils in realistic mean flows*. AIAA Journal 36 (1998), pp. 907–914.

[30] S. A. L. Glegg and W. J. Devenport. *Unsteady loading on an airfoil of arbitrary thickness*. Journal of Sound and Vibration 319 (2009), pp. 1252–1270.

[31] S. A. L. Glegg and W. J. Devenport. *Panel methods for airfoils in turbulent flow*. Journal of Sound and Vibration 329 (2010), pp. 3709–3720.

[32] S. Oerlemans. *Wind tunnel aeroacoustic tests of six airfoils for use on small wind turbines*. Tech. rep. National Renewable Energy Laboratory, 2004, NREL/SR-500–35339, 15007773.

[33] A. Hall et al. *Effect of leading-edge thickness on high-speed airfoil-turbulence interaction noise*. In: *17th AIAA/CEAS Aeroacoustics Conference (32nd AIAA Aeroacoustics Conference)*. Portland, OR, American Institute of Aeronautics and Astronautics, 2011.

[34] P. Chaitanya et al. *Aerofoil geometry effects on turbulence interaction noise*. In: *21st AIAA/CEAS Aeroacoustics Conference*. Dallas, TX, American Institute of Aeronautics and Astronautics, 2015.

[35] W. J. Devenport et al. *Sound radiation from real airfoils in turbulence*. Journal of Sound and Vibration 329 (2010), pp. 3470–3483.

[36] J. R. Gill et al. *Symmetric airfoil geometry effects on leading edge noise*. The Journal of the Acoustical Society of America 134 (2013), pp. 2669–2680.

[37] L. Bowen et al. *A thorough experimental investigation on airfoil turbulence interaction noise*. Physics of Fluids 35 (2023), p. 035123.

[38] G. Guidati et al. *Simulation and measurement of inflow-turbulence noise on airfoils*. In: *3rd AIAA/CEAS Aeroacoustics Conference*. Atlanta, GA, American Institute of Aeronautics and Astronautics, 1997.

[39] J. Gershfeld. *Leading edge noise from thick foils in turbulent flows*. The Journal of the Acoustical Society of America 116 (2004), pp. 1416–1426.

[40] M. S. Howe. *Contributions to the theory of aerodynamic sound, with application to excess jet noise and the theory of the flute*. Journal of Fluid Mechanics 71 (1975), pp. 625–673.

[41] P. D. Lysak et al. *Prediction of high frequency gust response with airfoil thickness effects*. Journal of Fluids and Structures 39 (2013), pp. 258–274.

[42] D. Kim et al. *Inflow broadband noise from an isolated symmetric airfoil interacting with incident turbulence*. Journal of Fluids and Structures 55 (2015), pp. 428–450.

[43] L. Prandtl. *Attaining a steady air stream in wind tunnels*. 1933.

[44] G. I. Taylor. *Turbulence in a contracting stream*. ZAMM - Journal of Applied Mathematics and Mechanics / Zeitschrift für Angewandte Mathematik und Mechanik 15 (1935), pp. 91–96.

[45] J. C. R. Hunt. *A theory of turbulent flow round two-dimensional bluff bodies*. Journal of Fluid Mechanics 61 (1973), pp. 625–706.

[46] H. S. Ribner and M. Tucker. *Spectrum of turbulence in a contracting stream*. Tech. rep. National Advisory Committee for Aeronautics, 1953. Chap. Technical Reports.

[47] G. K. Batchelor and I. Proudman. *The effect of rapid distortion of a fluid in turbulent motion*. The Quarterly Journal of Mechanics and Applied Mathematics 7 (1954), pp. 83–103.

[48] S. Moreau and M. Roger. *Effect of angle of attack and airfoil shape on turbulence-interaction noise*. In: *11th AIAA/CEAS Aeroacoustics Conference*. Monterey, CA, American Institute of Aeronautics and Astronautics, 2005.

[49] J. Christophe. *Application of hybrid methods to high frequency aeroacoustics*. PhD thesis. Université Libre de Bruxelles, 2011.

[50] L. D. De Santana et al. *A rapid distortion theory modified turbulence spectra for semi-analytical airfoil noise prediction*. Journal of Sound and Vibration 383 (2016), pp. 349–363.

[51] F. L. dos Santos et al. *Modeling the turbulence spectrum dissipation range for leading-edge noise prediction*. AIAA Journal (2022), pp. 1–12.

[52] F. L. dos Santos et al. *Inflow turbulence distortion for airfoil leading-edge noise prediction for large turbulence length scales for zero-mean loading*. The Journal of the Acoustical Society of America 153 (2023), pp. 1811–1822.

[53] P. Mish and W. J. Devenport. *An experimental investigation of unsteady surface pressure on an airfoil in turbulence—Part 1: Effects of mean loading*. Journal of Sound and Vibration 296 (2006), pp. 417–446.

[54] P. Mish and W. J. Devenport. *An experimental investigation of unsteady surface pressure on an airfoil in turbulence—Part 2: Sources and prediction of mean loading effects*. Journal of Sound and Vibration 296 (2006), pp. 447–460.

[55] F. L. dos Santos et al. *Study of the inflow turbulence distortion for airfoils and cylinders*. In: *AIAA Aviation 2023 Forum*. San Diego, CA, American Institute of Aeronautics and Astronautics, 2023.

[56] L. D. De Santana. *Semi-analytical methodologies for airfoil noise prediction*. PhD thesis. KU Leuven, 2015.

[57] M. Roger and S. Moreau. *Back-scattering correction and further extensions of Amiet's trailing-edge noise model. Part 1: theory*. Journal of Sound and Vibration 286 (2005), pp. 477–506.

[58] S. Moreau and M. Roger. *Back-scattering correction and further extensions of Amiet's trailing-edge noise model. Part II: Application*. Journal of Sound and Vibration 323 (2009), pp. 397–425.

[59] A. Bresciani et al. *Generalization of Amiet's theory for small reduced-frequency and nearly-critical gusts*. Journal of Sound and Vibration 524 (2022), p. 116742.

[60] R. Miotto et al. *Numerical computation of aeroacoustic transfer functions for realistic airfoils*. Journal of Sound and Vibration 407 (2017), pp. 253–270.

[61] Christopher Thurman et al. *Broadband noise prediction of two small hovering rotors using FUN3D-ANOPP2*. In: *AIAA Scitech 2025 Forum*. Orlando, FL, American Institute of Aeronautics and Astronautics, 2025.

[62] Stephen A Rizzi. *Urban Air Mobility noise: current practice, gaps, and recommendations* (2020).

[63] M. A. Boucher et al. *Toward a psychoacoustic annoyance model for Urban Air Mobility vehicle noise* (2024).

[64] Nikolas S. Zawodny et al. *Acoustic characterization and prediction of representative, small-scale rotary-wing unmanned aircraft system components*. In: *American Helicopter Society (AHS) Annual Forum*. West Palm Beach, FL, 2016.

[65] Eric Greenwood et al. *Challenges and opportunities for low noise electric aircraft*. International Journal of Aeroacoustics 21 (2022), pp. 315–381.

[66] I. J. Sharland. *Sources of noise in axial flow fans*. Journal of Sound and Vibration 1 (1964), pp. 302–322.

[67] J. C. Simonich et al. *Helicopter rotor noise due to ingestion of atmospheric turbulence*. Tech. rep. 1986.

[68] D. B. Hanson. *Spectrum of rotor noise caused by atmospheric turbulence*. The Journal of the Acoustical Society of America 55 (1974), S3–S4.

[69] Henrique Raposo and Mahdi Azarpeyvand. *Turbulence ingestion noise generation in rotating blades*. Journal of Fluid Mechanics 980 (2024), A53.

[70] S. J. Majumdar and N. Peake. *Noise generation by the interaction between ingested turbulence and a rotating fan*. Journal of Fluid Mechanics 359 (1998), pp. 181–216.

[71] M. E. Goldstein. *Unsteady vortical and entropic distortions of potential flows round arbitrary obstacles*. Journal of Fluid Mechanics 89 (1978), pp. 433–468.

[72] J. C. Simonich et al. *Rotor noise due to atmospheric turbulence ingestion. I - Fluid mechanics*. Journal of Aircraft (2012).

[73] R. K. Amiet. *Noise produced by turbulent flow into a propeller or helicopter rotor*. In: *3rd Aeroacoustics Conference*. Palo Alto, CA, American Institute of Aeronautics and Astronautics, 1976.

[74] G. F. Homicz and A. R. George. *Broadband and discrete frequency radiation from subsonic rotors*. Journal of Sound and Vibration 36 (1974), pp. 151–177.

[75] A. Piccolo et al. *Turbulence distortion and leading-edge noise*. Physics of Fluids 36 (2024), p. 125183.

[76] James Goldschmidt et al. *Acoustics and forces from an isolated rotor system*. In: *AIAA SCITECH 2022 Forum*. San Diego, CA & Virtual, American Institute of Aeronautics and Astronautics, 2022.

[77] N. Curle. *The influence of solid boundaries upon aerodynamic sound*. Proceedings of the Royal Society of London. Series A. Mathematical and Physical Sciences 231 (1955), pp. 505–514.

[78] Yannick Rozenberg. *Modélisation analytique du bruit aérodynamique à large bande des machines tournantes : utilisation de calculs moyennés de mécanique des fluides*. PhD thesis. Ecole Centrale de Lyon, 2007.

[79] L. D. De Santana et al. *Airfoil noise prediction from 2D3C PIV data*. In: *21st AIAA/CEAS Aeroacoustics Conference*. Dallas, TX, American Institute of Aeronautics and Astronautics, 2015.

[80] R. K. Amiet. *Noise produced by turbulent flow into a rotor: theory manual for noise calculation*. NASA Report. 1989.

[81] S. Sinayoko et al. *Trailing-edge noise theory for rotating blades in uniform flow* (2013).

[82] R. Zamponi et al. *Rapid distortion theory of turbulent flow around a porous cylinder*. Journal of Fluid Mechanics 915 (2021), A27.

[83] M. J. Lighthill. *Drift*. Journal of Fluid Mechanics 1 (1956), pp. 31–53.

[84] G. K. Batchelor. *An introduction to fluid dynamics*. Cambridge, UK: Cambridge University Press, 1967. ISBN: 978-0-521-66396-0.

[85] P. W. Bearman. *Some measurements of the distortion of turbulence approaching a two-dimensional bluff body*. Journal of Fluid Mechanics 53 (1972), p. 451.

[86] E. Grande et al. *Aeroacoustic Investigation of a Propeller Operating at Low Reynolds Numbers*. AIAA Journal 60 (2022), pp. 860–871.

[87] S. Succi. *The lattice Boltzmann equation: for fluid dynamics and beyond*. Oxford, UK: Oxford University Press, 2001. ISBN: 978-0-19-850398-9.

[88] H. Chen et al. *Recovery of the Navier-Stokes equations using a lattice-gas Boltzmann method*. Physical Review A 45 (1992), R5339–R5342.

[89] P. L. Bhatnagar et al. *A model for collision processes in gases. I. Small amplitude processes in charged and neutral one-component systems*. Physical Review 94 (1954), pp. 511–525.

[90] H. Xu and P. Sagaut. *Optimal low-dispersion low-dissipation LBM schemes for computational aeroacoustics*. Journal of Computational Physics (2011).

[91] Jianping Meng et al. *Analysis of non-physical slip velocity in lattice Boltzmann simulations using the bounce-back scheme*. Journal of Computational Science 28 (2018), pp. 476–482.

[92] David R. Noble et al. *A consistent hydrodynamic boundary condition for the lattice Boltzmann method*. Physics of Fluids 7 (1995), pp. 203–209.

[93] H. Chen et al. *Recovery of Galilean invariance in thermal lattice Boltzmann models for arbitrary prandtl number*. 2014. arXiv: 1403.2357.

[94] Marc B. Reider and James D. Sterling. *Accuracy of discrete-velocity BGK models for the simulation of the incompressible Navier-Stokes equations*. Computers & Fluids 24 (1995), pp. 459–467.

[95] C. Teruna. *Aerodynamic noise reduction with porous materials*. PhD thesis. Technische Universiteit Delft, 2022.

[96] V. Yakhot and S. Orszag. *Renormalization group analysis of turbulence. I. Basic theory*. Journal of Scientific Computing 1 (1986), pp. 3–51.

[97] V. Yakhot et al. *Development of turbulence models for shear flows by a double expansion technique*. Physics of Fluids A: Fluid Dynamics 4 (1992), pp. 1510–1520.

[98] H. Chen et al. *Expanded analogy between Boltzmann kinetic theory of fluids and turbulence*. Journal of Fluid Mechanics 519 (2004), pp. 301–314.

[99] H. Chen et al. *Realization of fluid boundary conditions via discrete boltzmann dynamics*. International Journal of Modern Physics C 09 (1998), pp. 1281–1292.

[100] B. E. Launder and D. B. Spalding. *The numerical computation of turbulent flows*. Computer Methods in Applied Mechanics and Engineering 3 (1974), pp. 269–289.

[101] F. Farassat and G. P. Succi. *A review of propeller discrete frequency noise prediction technology with emphasis on two current methods for time domain calculations*. Journal of Sound and Vibration 71 (1980), pp. 399–419.

[102] G. Brès et al. *Properties of the lattice Boltzmann method for acoustics*. In: *15th AIAA/CEAS Aeroacoustics Conference (30th AIAA Aeroacoustics Conference)*. Miami, FL, American Institute of Aeronautics and Astronautics, 2009.

[103] D. Casalino et al. *M.: Prediction of rod-airfoil interaction noise using the Ffowcs–Williams and Hawkings analogy*. AIAA Journal (2003), pp. 182–191.

[104] P. E. Roach. *The generation of nearly isotropic turbulence by means of grids*. International Journal of Heat and Fluid Flow 8 (1987), pp. 82–92.

[105] I.H. Abbott and Von Doenhoff. *Theory of wing sections*. New York, NY: Dover Publications, 1959.

[106] S. Narayanan et al. *Airfoil noise reductions through leading edge serrations*. Physics of Fluids 27 (2015), p. 025109.

[107] S. Pope. *Turbulent Flows*. Cambridge University Press, 2000. ISBN: 978-0-511-84053-1.

[108] S. A. L. Glegg and W. J. Devenport. *Turbulence and stochastic processes*. In: *Aeroacoustics of Low Mach Number Flows*. Academic Press, 2017, pp. 163–184. ISBN: 978-0-12-809651-2.

[109] M. Uberoi. *Effect of wind-tunnel contraction on free-stream turbulence* (1956).

[110] Geneviéve Comte-Bellot and Stanley Corrsin. *The use of a contraction to improve the isotropy of grid-generated turbulence*. Journal of Fluid Mechanics 25 (1966), pp. 657–682.

[111] P. Lavoie et al. *Effects of initial conditions in decaying turbulence generated by passive grids*. Journal of Fluid Mechanics 585 (2007), pp. 395–420.

[112] R. J. Hearst. *Fractal, classical, and active grid turbulence: from production to decay*. PhD thesis. University of Toronto, 2015.

[113] A. Zarri et al. *Aerodynamic investigation of the turbulent flow past a louvered-fin-and-tube automotive heat exchanger*. Experimental Thermal and Fluid Science (2024), p. 111182.

[114] John L. Lumley and Gary R. Newman. *The return to isotropy of homogeneous turbulence*. Journal of Fluid Mechanics 82 (1977), pp. 161–178.

[115] J. L. Lumley. *Computational modeling of turbulent flows*. Advances in applied mechanincs (1978).

[116] K. Choi and J. L. Lumley. *The return to isotropy of homogeneous turbulence*. Journal of Fluid Mechanics 436 (2001), pp. 59–84.

[117] M Emory and G Iaccarino. *Visualizing turbulence anisotropy in the spatial domain with componentality contours*. Annual Research Briefs 2014 (2014), pp. 123–138.

[118] A. L. Kistler and T. Vrebalovich. *Grid turbulence at large Reynolds numbers*. Journal of Fluid Mechanics 26 (1966), p. 37.

[119] Roberto Merino-Martínez et al. *Aeroacoustic design and characterization of the 3D-printed, open-jet, anechoic wind tunnel of Delft University of Technology*. Applied Acoustics 170 (2020), p. 107504.

[120] R. Zamponi et al. *On the role of turbulence distortion on leading-edge noise reduction by means of porosity*. Journal of Sound and Vibration 485 (2020), p. 115561.

[121] J. C. R. Hunt et al. *A review of velocity and pressure fluctuations in turbulent flows around bluff bodies*. Journal of Wind Engineering and Industrial Aerodynamics 35 (1990), pp. 49–85.

[122] R. Zamponi et al. *Effect of porosity on Curle's dipolar sources on an aerofoil in turbulent flow*. Journal of Sound and Vibration 542 (2023), p. 117353.

[123] A. Piccolo et al. *Turbulence-distortion analysis for leading-edge noise-prediction enhancement*. In: *AIAA Aviation 2023 Forum*. San Diego, CA, American Institute of Aeronautics and Astronautics, 2023.

[124] P. Moriarty et al. *Prediction of turbulent inflow and trailing-edge noise for wind turbines*. In: *11th AIAA/CEAS Aeroacoustics Conference*. Monterey, CA, American Institute of Aeronautics and Astronautics, 2005.

[125] P. A. Durbin and J. C. R. Hunt. *On surface pressure fluctuations beneath turbulent flow round bluff bodies*. Journal of Fluid Mechanics 100 (1980), pp. 161–184.

[126] A. Piccolo et al. *Towards a novel physics-based correction to Amiet's theory for inflow-turbulence noise prediction*. In: *30th AIAA/CEAS Aeroacoustics Conference (2024)*. Rome, Italy, American Institute of Aeronautics and Astronautics, 2024.

[127] M. Drela. *XFOIL: An analysis and design system for low Reynolds number airfoils*. In: *Low Reynolds Number Aerodynamics*. Berlin, Germany, Springer, 1989, pp. 1–12.

[128] S. A. L. Glegg et al. *Propeller noise: inflow distortion in a non axisymmetric flow*. In: *19th AIAA/CEAS Aeroacoustics Conference*. Berlin, Germany, American Institute of Aeronautics and Astronautics, 2013.

[129] S. A. L. Glegg et al. *Broadband rotor noise predictions using a time domain approach*. Journal of Sound and Vibration 335 (2015), pp. 115–124.

[130] Thomas F. Brooks and Casey L. Burley. *Blade wake interaction noise for a main rotor*. Journal of the American Helicopter Society 49 (2004), pp. 11–27.

[131] J. Christophe et al. *Amiet's theory in spanwise-varying flow conditions*. AIAA Journal 47 (2009), pp. 788–790.

[132] Korcan Kücükcoskun. *Prediction of free and scattered acoustic fields of low-speed fans*. PhD thesis. Ecole Centrale de Lyon, 2012.

[133] David K. Wilson. *Three-dimensional correlation and spectral functions for turbulent velocities in homogeneous and surface-blocked boundary layers*. Tech. rep. Defense Technical Information Center, 1997.

[134] T. von Kármán. *Progress in the statistical theory of turbulence* (1948).

[135] R. W. Paterson and R. K. Amiet. *Noise of a model helicopter rotor due to ingestion of isotropic turbulence*. Journal of Sound and Vibration 85 (1982), pp. 551–577.

[136] E. Grande et al. *Laminar Separation Bubble Noise on a Propeller Operating at Low Reynolds Numbers*. AIAA Journal 60 (2022), pp. 5324–5335.

[137] D. Casalino. *Lattice-Boltzmann calculations of rotor aeroacoustics in transitional boundary layer regime*. Aerospace Science and Technology (2022).

[138] S. A. L. Glegg and W. J. Devenport. *Aeroacoustics of low mach number flows*. Academic Press, 2023. ISBN: 978-0-443-19112-1.

ACKNOWLEDGEMENTS

I strongly believe in the importance of social networks, in their literal sense. As such, I consider this thesis, which marks the conclusion of a journey of both professional and personal growth, not as an individual achievement, but as the result of a collective effort to which countless people have contributed.

The PhD would never have started without the trust (and the project money, of course) that Daniele and Francesco put in me. Thank you, guys, for this opportunity and for believing in me through all the ups and downs of these four years. You helped me turn my *cazzate* into... *not cazzate*. No conclusion would have ever been reached without the dedication, effort, and, quite frankly, the blood that Riccardo poured into my work. The project would have died immediately without you, Ric, without your patience and your unwavering faith. I owe this entire PhD to you, so I really think I should be awarded 0.5 PhDs, while you should end up with a total of 1.5.

Every word I have written, every figure I have produced, every line of code, every screw I have tightened or cable I have plugged in, every document I have filled, every difficulty I have faced, and every day I have made it through without a mental breakdown is owed to my colleagues. Each of these small steps grew out of an interaction with one of you, offered in kindness and in the spirit of mutual support. Edo, Fer, Hugo, Manoel, Tercio, you have been a life jacket in a period particularly heavy as the beginning of the PhD was after the pandemic. Ambar, Anastasia, Brian, Claudia, Cristina, Emanuele, Donatella, Dylan, Federico, Federico, Frits, Isaac, Kaj, Muhammad, Nikita, Olivier, Ozgur, Rushi, Sen, Sylvia, Thomas, Yannick, you embody the network I'm speaking of, and each day I grow more admiring of how clever and supportive you all are.

Cristina, you have been the social glue of this network. Your charismatic energy, your perpetual and contagious smile, and your genuine interest in listening helped me get through all the daily challenges of the PhD. My days will be really empty without you. Federico, you are probably the most important brick in this whole network, the connection that brought together an otherwise divided world between Delft and Den Haag, between work and personal life. In both places you made me feel at home, because I knew I had a friend (read "a day at the beach", "orange wine", or "consumerist ideas") I could always count on.

But you don't earn a PhD without defending it, and there's no defense without paranimfs. Actually, without them, this part of my life would have been far more boring and culturally impoverished (and, admittedly, less snobbish). Manoel, Claudia, you showed me what friends truly are, and you have been a constant source of inspiration for me to become a better person. Manoel, if I possess even a grain of critical sense and the drive to dig beneath the surface, I owe it to your keen eye for original perspectives, to your intellectual independence, and to your nonconformist choices. All of this, together with your sincere attachment, helped me enter and thrive in this new chapter of my life. Claudia, in your omnidirectional curiosity, your boundless passions, and your deep commitment

to people, I found understanding and a relentless drive to explore and, most importantly, to share. You gave these four years a depth without which this journey would have been nothing more than a series of grey numbers and endless commutes. If, at the end of this PhD, I feel richer as a person, it is because of all you guys brought into my life, all you inspired me to become, and simply for having you both.

A PhD is also about more than just projects, numbers, figures, and results. This journey also needed a home, and a proxy family. This is exactly what you have been for me throughout these years, Luca and Daria. You have been my safe place, and the warm, affectionate smiles I knew would be waiting for me at home, no matter how the day had gone.

And, well, reaching the PhD is a journey in itself. Without you, Mamma and Papà, there would have been no PhD, no university, no school, no curiosity, and no music (sic!). You have always created the conditions for me to become who I wanted to be, to do what I wanted to do, and to follow my own path. You gave me room to grow while protecting me, letting me pursue my goals. In essence, I owe you everything. The same, starting with the cover of this book, applies to my brother, who has always, always, always been by my side, and with whom I share all the things that matter the most. I know I will never be alone because I can count on you, my favourite person in the world.

But, most importantly, completing the PhD required a great deal of strength, a steady sense of peace to maintain mental balance, and enough joy to truly enjoy the journey. Without you, Ale, I would never have found these on my own. You have the rare strength to create all of this, for yourself and for me, along with the patience to carry and support me every day. And this goes far beyond these four years of the PhD, extending to every obstacle I have faced over what has now become a significant portion of my life. I would be nothing without you. YOU are my strength, my peace, and my joy.

All of you have been indispensable. To those who have been with me from the beginning to the end, to those who shared only part of the journey, to those who stand with me now at the finish line, and to those who are no longer here,
my deepest and most heartfelt thanks.

Curriculum Vitæ

Andrea Piccolo

11-09-1993 Born in Naples, Italy.

Education

2012–2016 Bachelor's Degree in Aerospace Engineering
Universitá degli Studi di Napoli "Federico II"
Naples, Italy

2016–2019 Master's Degree in Aerospace Engineering
Universitá degli Studi di Napoli "Federico II"
Naples, Italy

2019–2020 Post-graduate Program in Energy Engineering and Operations
Politecnico di Torino
Turin, Italy

2021–2026 Ph.D. in Aeroacoustics
Technische Universiteit Delft
Delft, The Netherlands
Thesis: Turbulence Interaction Noise
Promotor: Dr. D. Ragni

LIST OF PUBLICATIONS

JOURNAL PUBLICATIONS

1. **A. Piccolo**, R. Zamponi, F. Avallone, D. Ragni, *Turbulence-distortion modelling for Amiet's theory enhancement*, Journal of Sound and Vibration **624**, 119503 (2025) .
2. **A. Piccolo**, R. Zamponi, F. Avallone, D. Ragni, *Modification of Amiet's model for turbulence-ingestion noise prediction in rotors*, The Journal of Acoustical Society of America **158**, 461-475 (2025).
3. **A. Piccolo**, R. Zamponi, F. Avallone, D. Ragni, *Turbulence Distortion and leading-edge noise*, Physics of Fluids **36**, 125183 (2024).

CONFERENCE PUBLICATIONS

6. M. Alí, **A. Piccolo**, R. Zamponi, D. Ragni, F. Avallone, *On the Impact of Turbulent Inflow on the Noise Generated by a Propeller Operating at Low Reynolds Number*, Forum Acusticum (2025)
5. **A. Piccolo**, R. Zamponi, F. Avallone, D. Ragni, *Effects of inflow conditions on turbulence-ingestion noise prediction*, Forum Acusticum (2025)
4. G. Capobianchi, S. Montagner, **A. Piccolo**, A. Di Marco, F. Avallone, G. Cafiero, D. Ragni, E. de Paola, L. G. Stoica, *Impact of turbulent inflow on the far-field noise generated by a propeller operating at low Reynolds number*, 30th AIAA/CEAS Aeroacoustics Conference (2024)
3. **A. Piccolo**, R. Zamponi, F. Avallone, D. Ragni, *Towards a novel physics-based correction to Amiet's theory for inflow-turbulence noise prediction*, 30th AIAA/CEAS Aeroacoustics Conference (2024)
2. L. Trascinelli, L. Bowen, **A. Piccolo**, R. Zamponi, D. Ragni, F. Avallone, B.Y. Zhou, B. Zang, *Numerical simulation of grid-generated turbulence interaction with a NACA0012 airfoil*, 29th AIAA/CEAS Aeroacoustics Conference (2023)
1. **A. Piccolo**, R. Zamponi, F. Avallone, D. Ragni, *Turbulence-distortion analysis for leading-edge noise-prediction enhancement*, 29th AIAA/CEAS Aeroacoustics Conference (2023)